UC Irvine

UC Irvine Electronic Theses and Dissertations

Title

Hippocampal neuron ensemble activities in wildtype and Alzheimer’s disease mice

Permalink

https://escholarship.org/uc/item/73s8f64n

Author

chen, lujia

Publication Date

2023

Copyright Information

This work is made available under the terms of a Creative Commons Attribution License, availalbe at https://creativecommons.org/licenses/by/4.0/

Peer reviewed|Thesis/dissertation

eScholarship.org Powered by the California Digital Library
University of California

UNIVERSITY OF CALIFORNIA,
IRVINE

Hippocampal neuron ensemble activities in wildtype and Alzheimer's disease mice

DISSERTATION

submitted in partial satisfaction of the requirements
for the degree of

DOCTOR OF PHILOSOPHY

in Biomedical Engineering

by

Lujia Chen

Dissertation Committee:
Professor Xiangmin Xu, Chair
Professor Zoran Nenadic
Professor Douglas A. Nitz

2023

Chapter 1 © 2023 Lujia Chen
Chapter 2 © 2022 Xiaoxiao Lin, Lujia Chen, David Baglietto-Vargas
All other materials © 2023 Lujia Chen

DEDICATION

To

my parents
my colleagues in Xu Lab
my advisors
collaborators
friends

in recognition of their kind support

TABLE OF CONTENTS

Page

LIST OF FIGURES iv

ACKNOWLEDGEMENTS vi

VITA ix

ABSTRACT OF THE DISSERTATION xi

INTRODUCTION 1

Chapter 1: Anatomical organization of temporally correlated neural calcium activity in the hippocampal CA1 region 10

Chapter 2: Spatial coding defects of hippocampal neural ensemble activities in the 3xTg-AD mouse model 89

Chapter 3: Impact of Alzheimer's disease and aging on the anatomical organization of temporally correlated CA1 pyramidal neurons 129

Chapter 4: Conclusions and future directions 159

LIST OF FIGURES

Page

Figure 1.1. GCaMP-based miniscope imaging and mouse preparations 47

Figure 1.2. Graphical illustrations of temporal calcium activity clusters, anatomical clusters and cluster overlap calculation 48

Figure 1.3. Hippocampal CA1 neurons are organized into anatomically clustered groups with temporally correlated calcium activities 489

Figure 1.4. Anatomical clusters are the basis of the functional organization during exploration of different regions of the behavioral arena 52

Figure 1.5. Anatomical cluster-specific calcium event activities vary across different environments 54

Figure 1.6 . Comparisons of anatomical clusters during active exploration and long-term immobility 56

Figure 1.7. Clusters of CA1 excitatory cells observed during mouse exploration in a square arena 58

Figure 1.8. Anatomical distributions of place cells in the clusters observed in the circle arena exploration experiment 61

Figure 1.9. CA1 neuron clusters and their relationships with the spatial activity maps in the square arena exploration 64

Figure 1.10. Cluster profile for mice in the ensemble activity map analysis 65

Figure 1.11. Overlap analysis of cluster-specific ensemble activity maps 67

Figure 1.12. Distributions of calcium transient durations do not show apparent abnormality 68

Figure 1.13. Anatomical cluster sizes in hippocampal CA1 of Camk2a-Cre; Ai163 mice 69

Figure 1.14. ICA-based assembly detection results in comparison with k-mean-based consensus clustering 71

Figure 1.15. Correlation analyses of intra-cluster, border intra-cluster, and border inter-cluster neighboring neuron pairs 73

Figure 1.16. Place cell ensemble rate map analysis for the circle arena data 76

Figure 1.17. Place cell ensemble rate map analysis for the rectangle arena data 78

Figure 1.18. Comparison of extraction results with/without the CNMF-E “with dendrite” feature 79

Figure 1.19. Lap-by-lap stability of detected CA1 neurons in linear track experiments 82

Figure 1.20. Numbers of firing fields of CA1 neurons across mice in different experiments 83

Figure 1.21. The application of Temporal Unmixing of Calcium Traces (TUnCaT) algorithm confirms anatomical clusters 84

Figure 2.1. Age-dependent change in amyloid beta (Aβ) and phospho-tau accumulation in 3xTg-AD mouse hippocampus 116

Figure 2.2. Miniscope imaging of in vivo neural calcium activities of hippocampal CA1 exciatory neurons in 3xTg-AD and Non-Tg mice 118

Figure 2.3 Comparative analyses of the numbers of active hippocampal CA1 neurons across age and AD groups using imaging trials during open field exploration 119

Figure 2.4. Hippocampal CA1 cells in 3xTg-AD mice exhibit altered calcium activities and impaired spatial coding during open field exploration 120

Figure 2.5. Linear track experiment data also supports impaired spatial coding in 3xTg AD hippocampal CA1 122

Figure 2.6. Neural calcium activities of 3xAD-Tg mice exhibit stronger locomotion modulation than Non-Tg mice 124

Figure 3.1. Temporally correlated hippocampal CA1 neurons are organized into anatomically clustered groups regardless of ages and genotypes 150

Figure 3.2. Higher Overlap between ensemble rate maps among young 5xFAD mice 152

Figure 3.3. Age-specific dissimilarity of CA1 neural clusters between rotated linear tracks 153

Figure 3.4. Mosaic level of anatomical clusters display significant correlation with temporal correlation but not rate map correlation 156

ACKNOWLEDGEMENTS

First and foremost, I would like to express my sincerest gratitude to my advisor, Dr. Xiangmin Xu, who has supported me throughout my entire graduate study with his knowledge, patience, and encouragement. Especially remembering the days when we had hot discussions on the research, and the times that I made mistakes, Dr. Xu have provided countless chances for me to introspect and improve. His merits, and well as his guidance, shaped my own values and showed me how to become a mature, independent, and successful scientist.

I would also like to thank Dr. Zoran Nenadic and Dr. Douglas A. Nitz for being my committee member and advisors on the research. As my co-advisor, Dr. Nenadic has taught me how to apply signal processing and system science to neuroscience questions, and kindly helped me to connected with Dr. Xu. Dr. Nitz, a distinguished cognitive neuroscientist in UCSD, has helped me extensively with the major projects of this thesis. Although busy himself, he kindly spent a large amount of time discussing the scientific questions and showed me how a typical cognitive neuroscientist considers the questions. All my three advisors, Dr. Xu, Dr. Nenadic and Dr. Nitz, have provided me with extensive guidance and generous help to my Ph.D. journey, and I will always be grateful for that.

I would also like to thank my lab members and collaborators who helped me with my graduate study. It was a pleasure to collaborate with Dr. Xiaoxiao Lin on various kinds of imaging experiments. Dr. Lin's knowledge of the anatomical structure of the brain and behavioral experiments have provided strong support to the publications we published in these years. I also want to thank Ms. Qiao Ye, a biochemist becoming a multidisciplinary scientist, for her help on various issues, and Ms. Gao Pan for her help on brain clearing and

Tissuecyte related projects. Special thanks to the lab's postdoctoral scholars. Dr. Yanjun Sun, a former member of the lab, for his kind suggestions on research and help in my career. Dr. Steven F. Grieco, a project scientist in the lab, has provided me with great help with manuscript writing and equipment setup. Also, Dr Hai Zhang has helped me with both 2-photon and miniscope imaging experiments, Dr. Kevin Gregory Johnston discussed with me about the computational technics and bioinformatics, and Dr. Suoqin Jin, a former postdoc and collaborator in Dr. Qing Nie's lab, helped with data analysis tools and mathematical expertise. At the same time, Ms. Ginny Wu, Ms. Michele Wu, and Ms. Lin Lin, working as lab managers, have worked hard to keep everything in the lab in order. It was an unforgettable period working with these great colleagues.

Lastly, please allow me to express my greatest appreciation to my family and friends for their encouragement and support during the study.

Chapter 1 of this thesis/dissertation is a reprint of the material as it appears in "Chen, L., Lin, X., Ye, Q., Nenadic, Z., Holmes, T. C., Nitz, D. A., & Xu, X. (2023). Anatomical organization of temporally correlated neural calcium activity in the hippocampal CA1 region. iScience", under the permission from Xiangmin Xu, the corresponding author. Xiaoxiao Lin and Qiao Ye performed viral injection, imaging and behavioral experiments. Lujia Chen performed calcium imaging and all the data analysis, prepared the figures and wrote the manuscript. Zoran Nenadic, Todd Holmes, Douglas A. Nitz and Xiangmin Xu participated in writing the manuscript. Xiangmin Xu designed and oversaw the project. This work was supported by US National Institutes of Health (NIH) grants R01 NS104897 and RF1 AG065675. Todd C. Holmes is supported by R35 GM127102.

Chapter 2 of this thesis/dissertation is a reprint of the material as it appears in “Lin, X., Chen, L., Baglietto-Vargas, D., Kamalipour, P., Ye, Q., LaFerla, F. M., Nitz, D. A., Holmes, T. C., & Xu, X. (2022). Spatial coding defects of hippocampal neural ensemble calcium activities in the triple-transgenic Alzheimer's disease mouse model. Neurobiology of Disease, 162, 105562”, Used the permission from co-first authors Xiaoxiao Lin, David Baglietto-Vargas and Xiangmin Xu, the corresponding author. Xiaoxiao Lin, Parsa Kamalipour and Qiao Ye performed imaging, behavioral and immunostaining experiments. Lujia Chen, Xiaoxiao Lin, David Baglietto-Vargas, Xiangmin Xu, Frank M. LaFerla, Douglas A. Nitz, and Todd C. Holmes analyzed the data, prepared the figures, and wrote the manuscript with help from other authors. Xiangmin Xu designed and oversaw the project. This work was supported by US National Institutes of Health (NIH) grants (R01NS078434, R01NS104897 and RF1AG065675) to Xiangmin Xu and Douglas A Nitz. Todd C. Holmes is supported by R35GM127102.

VITA

Lujia Chen

Education

09/2012-06/2016: B.S., Biomedical Engineering, Beihang University, China

09/2016-06/2023: Ph.D., Biomedical Engineering, UC Irvine

- 09/2016-01/2019: Nenadic Lab (PI: Dr. Zoran Nenadic)
- 01/2019-06/2023: Xu Lab (PI: Xiangmin Xu)

Publications

Chen, L., Lin, X., Ye, Q., Nenadic, Z., Holmes, T.C., Nitz, D.A., Xu, X., Anatomical organization of temporally correlated neural calcium activity in the hippocampal CA1 region, ISCIENCE (2023), doi: 10.1016:j.isci.2023.106703.

Zhang, H., Chen, L., Johnston, K. G., Crapser, J., Green, K. N., Ha, N. M.-L., Tenner, A.J., Holmes, T.C., Nitz, D.A., Xu, X. (2023). Degenerate mapping of environmental location presages deficits in object-location encoding and memory in the 5xFAD mouse model for Alzheimer's disease. Neurobiology of Disease, 176, 105939. doi: 10.1016/j.nbd.2022.105939

Lin, X., Chen, L*., Baglietto-Vargas, D., Kamalipour, P., Ye, Q., LaFerla, F. M., Nitz, D.A., Holmes, T.C., Xu, X. (2022). Spatial coding defects of hippocampal neural ensemble calcium activities in the triple-transgenic Alzheimer's disease mouse model. Neurobiology of Disease, 162, 105562. doi: 10.1016/j.nbd.2021.105562 * co-first author

Lin, X., Chen, L., Jullienne, A., Zhang, H., Salehi, A., Hamer, M., Holmes, T.C., Obenaus, A., Xu, X. (2022). Longitudinal dynamics of microvascular recovery after acquired cortical injury. Acta Neuropathologica Communications, 10(1), 59. doi:10.1186/s40478-022-01361-4

Tan, Z., Garduño, B. M., Aburto, P. F., Chen, L., Ha, N., Cogram, P., Holmes, T.C., Xu, X. (2022). Cognitively impaired aged Octodon degus recapitulate major neuropathological features of sporadic Alzheimer's disease. Acta Neuropathologica Communications, 10(1), 182. doi:10.1186/s40478-022-01481-x

Wong, J. C., Grieco, S. F., Dutt, K., Chen, L., Thelin, J. T., Inglis, G. A. S., Parvin, S., Garraway, S.M., Xu, X., Goldin, A.L., Escayg, A. (2021). Autistic-like behavior, spontaneous seizures, and increased neuronal excitability in a Scn8a mouse model. Neuropsychopharmacology. doi:10.1038/s41386-021-00985-9

Yu, Z., Guindani, M., Grieco, S. F., Chen, L., Holmes, T. C., & Xu, X. (2021). Beyond t test and ANOVA: applications of mixed-effects models for more rigorous statistical analysis in neuroscience research. Neuron. doi: 10.1016/j.neuron.2021.10.030

Grieco, S. F., Qiao, X., Zheng, X., Liu, Y., Chen, L., Zhang, H., Yu, Z., Gavornik, J.P., Lai, C., Gandhi, S.P., Holmes, T.C., Xu, X. (2020). Subanesthetic Ketamine Reactivates Adult Cortical Plasticity to Restore Vision from Amblyopia. Current Biology, 30(18), 3591-3603.e3598. doi: 10.1016/j.cub.2020.07.008

Sun, Y., Jin, S., Lin, X., Chen, L., Qiao, X., Jiang, L., Zhou P., Johnston K.G., Golshani P., Nie Q., Holmes T.C., Nitz. D.A., Xu, X. (2019). CA1-projecting subiculum neurons facilitate object–place learning. Nature Neuroscience, 22(11), 1857-1870. doi:10.1038/s41593-019-0496-y

Conferences

Chen L, Lin X, Jin S, Qing N, Nitz D. A, Xu X. Hippocampus neural ensemble representations of spatial mapping and learning in freely behaving mice. Program No. 333.06. 2019 Neuroscience Meeting Planner. Chicago, IL: Society for Neuroscience, 2019.

Zhang H, Chen L, Johnson K, Crapser J, Green K, Ha N, Tenner A, Holmes T, Nitz D, Xu X. Degenerate Spatial Mapping Presages Deficits in Object-Location Encoding and Memory in the 5xFAD Model for Alzheimer's disease. August 2022. UC Irvine Center for Neural Circuit Mapping 2022 conference, UC Irvine

Professional experience

Visiting student, Harborview Medical Center, University of Washington 02/2023

- Advisor: Dr. Dirk Keene
- Under supervision, perform human brain tissue collection, slicing, and digitalize the brain slices to database

ABSTRACT OF THE DISSERTATION

Hippocampal neuron ensemble activities in wildtype and Alzheimer's disease mice

by

Lujia Chen

Doctor of Philosophy in Biomedical Engineering

University of California, Irvine, 2023

Professor Xiangmin Xu, Chair

The hippocampal CA1 subregion is critical for processing spatial and episodic memories. As the principal cell type, CA1 pyramidal neurons have been found to represent variables that are essential for spatial navigation and elements in episodic memory. At the same time, multiple CA1 pyramidal neurons can display synchronized activations, which can represent complex memory elements that individual neurons cannot process. An important question to date is how the co-activated CA1 pyramidal neurons are spatially organized in anatomical space. Existing research on this question had provided contradictory results, and were all subjected to limitations, for example, the limited anatomical resolution for the electrophysiological-based studies, and the limited behavior for the two-photon based studies. Another question is how the organized co-activations of CA1 pyramidal neurons are affected by Alzheimer's disease (AD). Existing studies have revealed that AD can induce aberrant activation pattern in individual pyramidal neurons, and has negative impact on the circuit connectivity, but no study have investigated AD's potential influence on the anatomical organizations of the co-activating neuron subgroups. Here I utilized a novel imaging technique, the head-mounted miniature microscope (Miniscope), to investigate the ensemble activities of CA1 pyramidal neurons with the limitations above largely addressed. In Chapter 1, I used Miniscope to record neural ensemble activities in mouse hippocampal CA1 and identified sub-populations of excitatory neurons that co-active across the same second-long period

of time while also clustered in anatomical space. This kind of organization vary in membership and activity dynamics with respect to movement in different environments, and appear during immobility in the dark, suggesting internal mechanisms that guide their formation. In Chapter 2, I used Miniscope to investigate the populational CA1 neural activities in both wildtype and 3xTg AD mice, an Alzheimer's disease model mouse type contains three mutations associated with familial Alzheimer's disease. I identified hyperactivations among the CA1 pyramidal neuron populations in AD mice at different ages in open field exploration, as well as impaired spatial representation illustrated by lower spatial information score and higher sparsity. Having established Miniscope's ability to identify anatomical organization of co-activated CA1 pyramidal neurons, and to reveal the difference of their firing profile between control and AD genotypes, I examined the discovered temporal-anatomical pyramidal neuron clusters to both wildtype (WT) and 5xFAD mice under different ages. I found the clusters existed in both genotypes and no difference was noted for intra-cluster pairwise correlation and anatomical cluster size. When examining the cluster-level ensemble representation of the environment, young AD mice show a lower level of specificity between the labelling of different clusters, but no differences were noted between WT and AD for other age groups. Both WT and AD displayed elevated cluster dissimilarity between linear tracks with 90-degree direction difference, but only at 8~10-month age. Finally, the segregation level of the anatomical clusters, measured by the mosaic level metric, displayed significant negative correlation with the averaged pairwise correlation strength in young and mid WT mice, as well as young AD mice, but showed no significant relationship with the correlation of spatial rate maps. Together, the thesis describes a previously under studied organization of CA1 pyramidal neurons and performs preliminary investigation of how this

organization behaves under AD conditions. The results should contribute to our understanding of CA1 neural organizations that support the region's memory processing function.

INTRODUCTION

Hippocampal CA1 serves as the major output area of the hippocampal formation, and plays an important role in spatial navigation (O'Keefe & Dostrovsky, 1971; Skaggs et al., 1996) and episodic memory (Knierim et al., 2006; Wallenstein et al., 1998). Pyramidal neurons constitute the principal cell population in the area, who acquired their name from their remarkable dendrite-axon polarity. The somas of pyramidal neurons are tightly packed and form up the pyramidal cell layer, and their basal dendrites are located in the stratum oriens layer, while apical dendrites are located in stratum lacunosum-moleculare, which constitutes a clear laminar architecture (Amaral & Witter, 1989). CA1 pyramidal neurons receive major extrinsic input from hippocampal CA3 (Amaral & Witter, 1989) and layer 3 entorhinal cortex (Steward & Scoville, 1976). At the same time, they have bi-directional connectivity with the subiculum complex (Sun et al., 2019) and amygdala (Fanselow & Dong, 2010; Witter & Amaral, 1991), and provide output to entorhinal cortex layer 5 (Amaral & Witter, 1989; Anderson et al., 2014), retrosplenial cortex, anterior cingulated cortex, lateral septal nucleus, olfactory cortex, thalamus, and medial prefrontal cortex (Fanselow & Dong, 2010; Wirt & Hyman, 2017). Intrinsically, GABAergic interneurons have vast connection with pyramidal neuron subpopulations and provide inhibitory regulation to their activation patterns (Kullmann, 2011; Pelkey et al., 2017). Recent reports indicate that pairs of pyramidal neurons could have a higher-than-expect level of direct connectivity (Geiller et al., 2022; Yang et al., 2014).

Functionally, individual CA1 pyramidal neurons can represent various cognitive variables like location (O'Keefe & Dostrovsky, 1971), head direction (Leutgeb et al., 2000), and reward (Gauthier & Tank, 2018). At the same time, ensembles of CA1 pyramidal neurons can display co-activation in a short time window (Buzsáki, 2010; Harris et al., 2003). A typical example is the replay phenomenon, in which CA1 pyramidal neurons fire sequentially during sleep or immobile

period (Davidson et al., 2009; Pavlides & Winson, 1989; Skaggs & McNaughton, 1996; Wilson & McNaughton, 1994). Decoding analysis has revealed that replays largely represent the trajectories animals have taken during recent experiments, which are episodic memories that individual place cells cannot represent (Davidson et al., 2009; Knierim, 2009). Meanwhile, co-activated CA1 pyramidal neurons can also represent non-spatial content. For example, in a cue-combination task in which animals must memorize a specific sequence of sounds and odors to get the reward, pyramidal neuron populations are reported to possess subpopulations with strong co-activation at different types of cues that lead to the reward. However, when cues not-relevant to reward are presented, the co-activations do not appear (Terada et al., 2017). At the same time, during the fear conditioning task, ventral CA1 shock-responsive pyramidal neurons can display correlated firing with groups of non-shock-responsive neurons, and their correlation strength is proportional to the fear memory retrieval efficiency (Jimenez et al., 2020).

The collective, coordinated activation of CA1 pyramidal cells (Buzsáki, 2010; Harris et al., 2003) have been hypothesized to be the "cell assemblies" proposed by Hebb in 1940s (Hebb, 1949), which are groups of interconnected neurons that can support complex cognitive process (Buzsáki, 2010; Sejnowski & Churchland, 1992). However, although the assembly model illustrated a potential circuit-level mechanism, till now the actual circuit basis that guides the ensemble activations in CA1 is still not fully understood. An unresolved question in the direction is whether CA1 pyramidal cells displaying co-activations are distributed uniformly, or exhibiting clustered distributions, in anatomical space. Existing studies on the question have generated contradictory results. Via electrophysiology recording, Hampson et al. 1999 reported CA1 cells that represent different reward locations occupy different anatomical locations (Hampson et al., 1999). Redish et al. 2001, however, reported no obvious anatomical patterns for CA1 place cells

(Redish et al., 2001). Later, using 2-photon calcium imaging and VR linear track, Dombeck et al. 2010 reported similar conclusion to Redish et al. research with examining place cells, although when including all the neurons under the field of view, a significant negative trend between neuron pairwise correlation and pairwise distance appeared (Dombeck et al., 2010). Meanwhile, also with 2-photon imaging, Modi et al. 2014 reported anatomically clustered CA1 pyramidal cells displaying correlated firing after a trace-blink task(Modi et al., 2014). One potential reason for these mixed results could be the limitations/differences of the recording technology used in each experiment. Electrophysiology recordings have limited anatomical resolution. 2-photon calcium imaging is able to simultaneously record calcium transients and individual neurons' anatomical profile with high precision, but in Dombeck et al.'s study, the virtual reality setting, as well as the limited field of view, may have limited the number of neurons they can examine, thus the full profile of CA1 pyramidal cell's distribution is not achieved (Wirtshafter & Disterhoft, 2022). Another potential reason could be the neuron populations included in the analysis. Consider the difference of place cell populations and all under-the-field-of-view neurons noted by Dombeck et al. , and the fact that CA1 pyramidal neurons display heterogeneity in gene expression and connectivity across different anatomical locations (Cembrowski & Spruston, 2019; Soltesz & Losonczy, 2018), examining pyramidal neurons without specific exclusion criteria may provide a more complete picture of their anatomical embeddings.

A comprehensive study of the co-active CA1 pyramidal neurons, and their anatomical organizations, can advance multiple frontiers in neuroscience, one of which could be Alzheimer's disease (AD) research. AD has been found to have major impact on hippocampal CA1 area (Padurariu et al., 2012). A-beta amyloid plaques, which is a major biomarker of the disease, have cellular toxicity and can cause CA1 pyramidal neurons to exhibit aberrant hyperactivity (Busche

et al., 2012; De Strooper & Karran, 2016). At the same time, neuronal dendrites will suffer from spine loss and morphology distortion when A-beta plaques are present, which leads to the loss of connections between neurons (Kuchibhotla et al., 2008; Neuman et al., 2015). Lastly, it is found that CA1 interneurons display reduced inhibition toward their pyramidal cell targets under the AD condition (Kurudenkandy et al., 2014; Palop & Mucke, 2016), and CA1 intrinsic gamma oscillations, which are believed to be generated by local interneuron populations (Kullmann, 2011), cannot maintain normal amplitude and rhythmic under AD (Palop & Mucke, 2016). These results indicate that CA1 pyramidal neuron assemblies can be dysregulated under AD as interneurons provide critical regulation to them. Given the important role of CA1 pyramidal neuron ensemble activities in memory representation, study the difference the ensemble activity patterns and their underlying micro-circuits under healthy and AD condition would provide insight of the disease's impact on the memory encoding and retrieval process in the area.

Recent advance in head-mounted miniature have enabled large-scale recording of neuron populations with single neuron resolution under freely behaving behavior (Aharoni & Hoogland, 2019), which cannot be simultaneously achieved by the widely used electrophysiological recording and stationary two-photon imaging. Meanwhile, the development of computational techniques has provided better tools for anatomical organizations and functional types of CA1 pyramidal cells. With the technologies in hand, I performed a set of experiments to investigate the temporal and anatomical organizations of ensemble CA1 pyramidal neuron activities, in both wildtype and Alzheimer's disease mouse models including 3xtg AD and 5xFAD, with the results documented in the following chapters:

In Chapter 1, I investigated the anatomical organization of temporally correlated CA1 pyramidal neurons when animals freely traverse across the environment. Interestingly, I identified

several groups of pyramidal neurons that display correlated calcium activities clustered in anatomical space, forming up several scattered patches whose size is significantly larger than the baseline level. Ensemble activities of these pyramidal neuron clusters covered different regions of the environment; meanwhile, place cells only constituted a part of the intra-cluster neuron populations, indicate the clustered pyramidal neuron subpopulation have functional roles that related to the experience in the specific region, but not restricted to place encoding. More importantly, the neuron membership of multiple clusters significantly varied between altered environments like linear tracks with 90-degree direction difference, and boxes with or without obstacles. Lastly, these temporal-anatomical pyramidal neuron clusters still exist during immobility in dark environment. These results illustrated a previously under studied topologic representation inside CA1 area that may guide the generation of ensemble activity of pyramidal neurons and provided insights to the long-standing debate of the anatomical organizations of CA1 pyramidal neuron assemblies.

In Chapter 2, I investigated how the ensemble activity pattern is differentiated between ordinary animals and an Alzheimer's disease model mouse type called 3xTg AD. This disease model contained mutations to familial AD genes that lead to both Aβ plaques and Neurofibrillary tangles tau, which provides a more complete picture about the pathological influence of the disease (Oddo et al., 2003). We identified the hyperexcitability among the CA1 pyramidal neuron population in 3xTg AD mice, which aligned with the existing findings in other AD mouse models (Busche et al., 2012). In both open field and linear track traversal, CA1 pyramidal neuron population in both young and old 3xTg AD animal displayed lower information score and higher sparsity compared to normal animal, which indicated a sub-optimal spatial representation among

the CA1 pyramidal neurons under AD condition. These results established the deficiency in spatial representation of CA1 pyramidal neurons under AD condition.

Given the findings above, an interesting question would be how the anatomical organizations in chapter 1 differ between healthy condition and AD condition at different stages. Hence, in Chapter 3 I investigated the anatomical organization of temporally correlated CA1 pyramidal neurons in wild type (WT) and 5xFAD animals at 3 different ages. Interestingly, anatomical clusters appeared among the temporally correlated pyramidal neuron populations in both WT and 5xFAD animals, and no significant difference are noted in terms of the anatomical cluster size and intra-temporal cluster pairwise correlation levels. When examining the cluster-level ensemble representation of the environment, young AD mice show a lower level of specificity between the labelling of different clusters, but no differences were noted between WT and AD for other age groups. When comparing between two tracks with different directions, remapping appeared among the CA1 pyramidal cell populations of both WT and 5xFAD at young and middle age, as well as old WT mice, as shown by the rate map correlation. However, for the temporal-anatomical neuron clusters, increased dissimilarity was only noted at middle age. Lastly, we tried to investigate the link between anatomical features and activities by defining mosaic index, a measure of local cluster type variability and could represent the segregation level of anatomical clusters and compared it to the within trial temporal pairwise correlation, and within-trial rate map pairwise correlation. We found the metric exhibit significant negative correlation toward the intra-cluster temporal correlation level for young WT, middle-aged WT, and young AD mice, but showed no significant correlation with intra-cluster rate map correlation.

In Chapter 4, I provide conclusion remarks on how the ensemble activity patterns, as well as their anatomical organizations, are different between normal and Alzheimer's disease animals.

I mentioned some potential future directions for investigating the temporally correlated, anatomically clustered CA1 pyramidal neurons, and discussed the opportunity provided by the spatial transcriptomic of directly aligning the molecular profile and functional properties of neurons defined by imaging. Overall, results in this thesis should contribute to a better understanding of how CA1 fulfills its functional roles, and how neurodegeneration diseases disrupting the memory representations in the area.

Reference

Aharoni, D., & Hoogland, T. M. (2019). Circuit Investigations With Open-Source Miniaturized Microscopes: Past, Present and Future [10.3389/fncel.2019.00141]. *Frontiers in Cellular Neuroscience*, *13*, 141. https://www.frontiersin.org/article/10.3389/fncel.2019.00141

Amaral, D. G., & Witter, M. P. (1989). The three-dimensional organization of the hippocampal formation: A review of anatomical data. *Neuroscience*, *31*(3), 571-591. https://doi.org/https://doi.org/10.1016/0306-4522(89)90424-7

Anderson, E. B., Grossrubatscher, I., & Frank, L. (2014). Dynamic Hippocampal Circuits Support Learning- and Memory-Guided Behaviors. *Cold Spring Harbor Symposia on Quantitative Biology*, *79*, 51-58. http://symposium.cshlp.org/content/79/51.abstract

Busche, M. A., Chen, X., Henning, H. A., Reichwald, J., Staufenbiel, M., Sakmann, B., & Konnerth, A. (2012). Critical role of soluble amyloid-β for early hippocampal hyperactivity in a mouse model of Alzheimer's disease. *Proceedings of the National Academy of Sciences*, *109*(22), 8740. https://doi.org/10.1073/pnas.1206171109

Buzsáki, G. (2010). Neural Syntax: Cell Assemblies, Synapsembles, and Readers. *Neuron*, *68*(3), 362-385. https://doi.org/https://doi.org/10.1016/j.neuron.2010.09.023

Cembrowski, M. S., & Spruston, N. (2019). Heterogeneity within classical cell types is the rule: lessons from hippocampal pyramidal neurons. *Nature Reviews Neuroscience*, *20*(4), 193-204. https://doi.org/10.1038/s41583-019-0125-5

Davidson, T. J., Kloosterman, F., & Wilson, M. A. (2009). Hippocampal Replay of Extended Experience. *Neuron*, *63*(4), 497-507. https://doi.org/https://doi.org/10.1016/j.neuron.2009.07.027

De Strooper, B., & Karran, E. (2016). The Cellular Phase of Alzheimer's Disease. *Cell*, *164*(4), 603-615. https://doi.org/https://doi.org/10.1016/j.cell.2015.12.056

Dombeck, D. A., Harvey, C. D., Tian, L., Looger, L. L., & Tank, D. W. (2010). Functional imaging of hippocampal place cells at cellular resolution during virtual navigation. *Nature Neuroscience*, *13*(11), 1433-1440. https://doi.org/10.1038/nn.2648

Fanselow, M. S., & Dong, H.-W. (2010). Are the Dorsal and Ventral Hippocampus Functionally Distinct Structures? *Neuron*, *65*(1), 7-19. https://doi.org/https://doi.org/10.1016/j.neuron.2009.11.031

Gauthier, J. L., & Tank, D. W. (2018). A Dedicated Population for Reward Coding in the Hippocampus. *Neuron*, *99*(1), 179-193.e177. https://doi.org/https://doi.org/10.1016/j.neuron.2018.06.008

Geiller, T., Sadeh, S., Rolotti, S. V., Blockus, H., Vancura, B., Negrean, A., Murray, A. J., Rózsa, B., Polleux, F., Clopath, C., & Losonczy, A. (2022). Local circuit amplification of spatial selectivity in the hippocampus. *Nature*, *601*(7891), 105-109. https://doi.org/10.1038/s41586-021-04169-9

Hampson, R. E., Simeral, J. D., & Deadwyler, S. A. (1999). Distribution of spatial and nonspatial information in dorsal hippocampus. *Nature*, *402*(6762), 610-614. https://doi.org/10.1038/45154

Harris, K. D., Csicsvari, J., Hirase, H., Dragoi, G., & Buzsáki, G. (2003). Organization of cell assemblies in the hippocampus. *Nature*, *424*(6948), 552-556. https://doi.org/10.1038/nature01834

Hebb, D. O. (1949). *The organization of behavior; a neuropsychological theory*. Wiley.

Jimenez, J. C., Berry, J. E., Lim, S. C., Ong, S. K., Kheirbek, M. A., & Hen, R. (2020). Contextual fear memory retrieval by correlated ensembles of ventral CA1 neurons. *Nature Communications*, *11*(1), 3492. https://doi.org/10.1038/s41467-020-17270-w

Knierim, J. J. (2009). Imagining the Possibilities: Ripples, Routes, and Reactivation. *Neuron*, *63*(4), 421-423. https://doi.org/https://doi.org/10.1016/j.neuron.2009.08.002

Knierim, J. J., Lee, I., & Hargreaves, E. L. (2006). Hippocampal place cells: Parallel input streams, subregional processing, and implications for episodic memory [https://doi.org/10.1002/hipo.20203]. *Hippocampus*, *16*(9), 755-764. https://doi.org/https://doi.org/10.1002/hipo.20203

Kuchibhotla, K. V., Goldman, S. T., Lattarulo, C. R., Wu, H.-Y., Hyman, B. T., & Bacskai, B. J. (2008). Aβ Plaques Lead to Aberrant Regulation of Calcium Homeostasis In Vivo Resulting in Structural and Functional Disruption of Neuronal Networks. *Neuron*, *59*(2), 214-225. https://doi.org/https://doi.org/10.1016/j.neuron.2008.06.008

Kullmann, D. M. (2011). Interneuron networks in the hippocampus. *Current Opinion in Neurobiology*, *21*(5), 709-716. https://doi.org/https://doi.org/10.1016/j.conb.2011.05.006

Kurudenkandy, F. R., Zilberter, M., Biverstål, H., Presto, J., Honcharenko, D., Strömberg, R., Johansson, J., Winblad, B., & Fisahn, A. (2014). Amyloid-β-Induced Action Potential Desynchronization and Degradation of Hippocampal Gamma Oscillations Is Prevented by Interference with Peptide Conformation Change and Aggregation. *The Journal of Neuroscience*, *34*(34), 11416. https://doi.org/10.1523/JNEUROSCI.1195-14.2014

Leutgeb, S., Ragozzino, K. E., & Mizumori, S. J. Y. (2000). Convergence of head direction and place information in the CA1 region of hippocampus. *Neuroscience*, *100*(1), 11-19. https://doi.org/https://doi.org/10.1016/S0306-4522(00)00258-X

Modi, M. N., Dhawale, A. K., & Bhalla, U. S. (2014). CA1 cell activity sequences emerge after reorganization of network correlation structure during associative learning. *eLife*, *3*, e01982. https://doi.org/10.7554/eLife.01982

Neuman, K. M., Molina-Campos, E., Musial, T. F., Price, A. L., Oh, K.-J., Wolke, M. L., Buss, E. W., Scheff, S. W., Mufson, E. J., & Nicholson, D. A. (2015). Evidence for Alzheimer's disease-linked synapse loss and compensation in mouse and human hippocampal CA1 pyramidal neurons. *Brain Structure and Function*, *220*(6), 3143-3165. https://doi.org/10.1007/s00429-014-0848-z

O'Keefe, J., & Dostrovsky, J. (1971). The hippocampus as a spatial map. Preliminary evidence from unit activity in the freely-moving rat. *Brain Research*, *34*(1), 171-175. https://doi.org/https://doi.org/10.1016/0006-8993(71)90358-1

Oddo, S., Caccamo, A., Shepherd, J. D., Murphy, M. P., Golde, T. E., Kayed, R., Metherate, R., Mattson, M. P., Akbari, Y., & LaFerla, F. M. (2003). Triple-Transgenic Model of Alzheimer's Disease with Plaques and Tangles: Intracellular Aβ and Synaptic Dysfunction. *Neuron*, *39*(3), 409-421. https://doi.org/https://doi.org/10.1016/S0896-6273(03)00434-3

Padurariu, M., Ciobica, A., Mavroudis, I., Fotiou, D., & Baloyannis, S. (2012). Hippocampal neuronal loss in the CA1 and CA3 areas of Alzheimer's disease patients. *Psychiatria Danubina*, *24*(2.), 152-158.

Palop, J. J., & Mucke, L. (2016). Network abnormalities and interneuron dysfunction in Alzheimer disease. *Nature Reviews Neuroscience*, *17*(12), 777-792. https://doi.org/10.1038/nrn.2016.141

Pavlides, C., & Winson, J. (1989). Influences of hippocampal place cell firing in the awake state on the activity of these cells during subsequent sleep episodes. *The Journal of Neuroscience*, *9*(8), 2907. https://doi.org/10.1523/JNEUROSCI.09-08-02907.1989

Pelkey, K. A., Chittajallu, R., Craig, M. T., Tricoire, L., Wester, J. C., & McBain, C. J. (2017). Hippocampal GABAergic Inhibitory Interneurons. *Physiological Reviews*, *97*(4), 1619-1747. https://doi.org/10.1152/physrev.00007.2017

Redish, A. D., Battaglia, F. P., Chawla, M. K., Ekstrom, A. D., Gerrard, J. L., Lipa, P., Rosenzweig, E. S., Worley, P. F., Guzowski, J. F., McNaughton, B. L., & Barnes, C. A. (2001). Independence of Firing Correlates of Anatomically Proximate Hippocampal Pyramidal Cells. *The Journal of Neuroscience*, *21*(5), RC134. https://doi.org/10.1523/JNEUROSCI.21-05-j0004.2001

Sejnowski, T. J., & Churchland, P. (1992). *The computational brain*. JSTOR.

Skaggs, W. E., & McNaughton, B. L. (1996). Replay of Neuronal Firing Sequences in Rat Hippocampus During Sleep Following Spatial Experience. *Science*, *271*(5257), 1870-1873. https://doi.org/10.1126/science.271.5257.1870

Skaggs, W. E., McNaughton, B. L., Wilson, M. A., & Barnes, C. A. (1996). Theta phase precession in hippocampal neuronal populations and the compression of temporal sequences [https://doi.org/10.1002/(SICI)1098-1063(1996)6:2<149::AID-HIPO6>3.0.CO;2-K]. *Hippocampus*, *6*(2), 149-172. https://doi.org/https://doi.org/10.1002/(SICI)1098-1063(1996)6:2<149::AID-HIPO6>3.0.CO;2-K

Soltesz, I., & Losonczy, A. (2018). CA1 pyramidal cell diversity enabling parallel information processing in the hippocampus. *Nature Neuroscience*, *21*(4), 484-493. https://doi.org/10.1038/s41593-018-0118-0

Steward, O., & Scoville, S. A. (1976). Cells of origin of entorhinal cortical afferents to the hippocampus and fascia dentata of the rat [https://doi.org/10.1002/cne.901690306]. *Journal of Comparative Neurology*, *169*(3), 347-370. https://doi.org/https://doi.org/10.1002/cne.901690306

Sun, Y., Jin, S., Lin, X., Chen, L., Qiao, X., Jiang, L., Zhou, P., Johnston, K. G., Golshani, P., Nie, Q., Holmes, T. C., Nitz, D. A., & Xu, X. (2019). CA1-projecting subiculum neurons facilitate object–place learning. *Nature Neuroscience*, *22*(11), 1857-1870. https://doi.org/10.1038/s41593-019-0496-y

Terada, S., Sakurai, Y., Nakahara, H., & Fujisawa, S. (2017). Temporal and Rate Coding for Discrete Event Sequences in the Hippocampus. *Neuron*, *94*(6), 1248-1262.e1244. https://doi.org/https://doi.org/10.1016/j.neuron.2017.05.024

Wallenstein, G. V., Hasselmo, M. E., & Eichenbaum, H. (1998). The hippocampus as an associator of discontiguous events. *Trends in Neurosciences*, *21*(8), 317-323. https://doi.org/https://doi.org/10.1016/S0166-2236(97)01220-4

Wilson, M. A., & McNaughton, B. L. (1994). Reactivation of Hippocampal Ensemble Memories During Sleep. *Science*, *265*(5172), 676-679. https://doi.org/10.1126/science.8036517

Wirt, R. A., & Hyman, J. M. (2017). Integrating Spatial Working Memory and Remote Memory: Interactions between the Medial Prefrontal Cortex and Hippocampus. *Brain Sciences*, *7*(4). https://doi.org/10.3390/brainsci7040043

Wirtshafter, H. S., & Disterhoft, J. F. (2022). Place cells are nonrandomly clustered by field location in CA1 hippocampus [https://doi.org/10.1002/hipo.23489]. *Hippocampus*, *n/a*(n/a). https://doi.org/https://doi.org/10.1002/hipo.23489

Witter, M. P., & Amaral, D. G. (1991). Entorhinal cortex of the monkey: V. Projections to the dentate gyrus, hippocampus, and subicular complex [https://doi.org/10.1002/cne.903070308]. *Journal of Comparative Neurology*, *307*(3), 437-459. https://doi.org/https://doi.org/10.1002/cne.903070308

Yang, S., Yang, S., Moreira, T., Hoffman, G., Carlson, G. C., Bender, K. J., Alger, B. E., & Tang, C.-M. (2014). Interlamellar CA1 network in the hippocampus. *Proceedings of the National Academy of Sciences*, *111*(35), 12919. https://doi.org/10.1073/pnas.1405468111

Chapter 1: Anatomical organization of temporally correlated neural calcium activity in the hippocampal CA1 region

Abstract

Hippocampal CA1 neuronal ensembles generate sequential patterns of firing activity that contribute to episodic memory formation and spatial cognition. Here we use *in vivo* calcium imaging to record neural ensemble activities in mouse hippocampal CA1 and identify CA1 excitatory neuron sub-populations whose members are active across the same second-long period of time. We identified groups of hippocampal neurons sharing temporally correlated neural calcium activity during behavioral exploration and found that they also organized as clusters in anatomical space. Such clusters vary in membership and activity dynamics with respect to movement in different environments, but also appear during immobility in the dark suggesting an internal dynamic. The strong covariance between dynamics and anatomical location within the CA1 sub-region reveals a previously unrecognized form of topographic representation in hippocampus that may guide generation of hippocampal sequences across time and therefore organize the content of episodic memory.

Introduction

Hippocampal CA1 neurons are well-known for the spatial tuning of their dynamics within the boundaries of the observable environment (Krupic et al., 2018; O'Keefe & Burgess, 1996; O'Keefe & Dostrovsky, 1971). Because their spatially specific firing fields are approximately uniform in their environmental distribution, ensembles of "place cells" are activated in sequential patterns depending on the trajectories the animal takes through an environment (Pfeiffer & Foster, 2013; Skaggs & McNaughton, 1996). The compression and recurrence of such sequences within each cycle (~125ms) of locomotion-driven theta-frequency oscillation yield a set of highly organized spike-timing relationships among interconnected hippocampal neurons (O'Keefe & Recce, 1993; William E. Skaggs et al., 1996). Such sequencing is thought to be consequential with respect to the generation of episodic memories (O'Keefe & Recce, 1993; William E. Skaggs et al., 1996).

The "place-specific" firing of hippocampal neurons over longer, seconds-duration time periods can also be systematically matched to the specific trajectories taken through any given environment (Markus et al., 1994; Nitz, 2006; Wilson & McNaughton, 1993; Wood et al., 2000). Notably, trajectory shape can promote the generation of path-discernable sequences for different visits to a single location(Brown et al., 1998; Grieves et al., 2016; Markus et al., 1995). Brain dynamics promoting synaptic potentiation according to activity patterns at this second-long timescale have also been identified(Bittner et al., 2017).

Multiple factors contribute to the organization of path specific sequential patterns of CA1 neuron activity. Sequences in hippocampal sub-region CA1 are thought to be generated, at least in part, by connectivity motifs within highly "auto-associative" sub-regions such as CA3 (Guzman et al., 2016; McNaughton & Morris, 1987; Treves & Rolls, 1994) and the distinct axonal

arborization patterns of GABAergic interneurons. Such "internal" connectivity constraints molding CA1 firing patterns are thought to interact with inputs coding for relation to distal visual cues, proximity to boundaries, self-motion cues, heading direction, and trajectory in regions such as the medial entorhinal cortex and nucleus reuniens (Giocomo, 2016; Ito et al., 2018) . Yet, similar sequential patterns of CA1 neuron activity can be observed even under conditions of minimal sensory input in immobile and sleeping animals (Wilson & McNaughton, 1994). These firing patterns are thought to represent internal dynamics of mental replay of previously learned routes and highlight both the constrained and versatile nature of CA1 neurons regarding their specific sequential patterns of activity.

Due to the complexity of factors influencing CA1 neuron firing, including restrictions on the scope of activity measurements, few studies have asked whether the temporal dynamics of CA1 neurons are related to their anatomical distribution[34]. Such a relationship would reveal a hippocampal organization that has previously eluded experimenters. In the present work, we have directly addressed this question by examining the temporal dynamics of large numbers of CA1 neurons longitudinally using in vivo calcium imaging with miniature head-mounted microscopes ("miniscopes") in mice during free exploration of multiple environments. We identify groups of CA1 neurons with temporally correlated calcium activity patterns and find that these groups are organized anatomically within CA1. This reveals a previously unrecognized form of topographic representation in the hippocampus that may guide neural activity contributing to spatial navigation and episodic memory.

In this work, Xiaoxiao Lin and Qiao Ye performed viral injection, imaging and behavioral experiments. I performed calcium imaging and all the data analysis, and together with all other

authors, prepared the figures and wrote the manuscript. Dr. Xiangmin Xu designed and oversaw the project.

Methods

Animals

All experiments were conducted according to the National Institute of Health guidelines for animal care and use and were approved by the Institutional Animal Care and Use Committee and the Institutional Biosafety Committee of the University of California, Irvine. C57BL/6J and Camk2a-Cre mice were acquired from Jackson Laboratory for the described experiments. Ai163 mice were directly transferred from the Allen Institute for Brain Science. Camk2a-Cre; Ai163 mice were obtained by crossing Ai163 and Camk2a-Cre mice. C57BL/6J and Camk2a-Cre; Ai163 mice were all between 4-8 months old. In the circle, square and triangle box experiment for Figures 1.3 and 1.5, 2 male and 4 female mice were included; In the open arena experiment for Figure 1.4, 5 male and 7 female mice were included; In the linear track experiment for Figure 1.5 , 2 male and 4 female mice were included; In the barrier experiment for Figure 1.5 , 5 male mice were included; In the immobility experiment for Figure 1.6 , 3 male mice were included. Animals had access to food and water in their home cages with lights maintained on a 12 h light/dark cycle (lights on at 6:30 am, lights off at 6:30 pm)

Mouse surgery and viral injections (Figure 1.1)

The general procedure for viral injections has been described previously(Yanjun Sun et al., 2019). To perform stereotaxic viral injections into the brain, mice were anesthetized under 1.5% isoflurane for 10 minutes with a 0.8 L/min oxygen flow rate using a bench top unit (HME1-9, Highland Medical Equipment). Mice were then placed into a stereotaxic unit for mice (Leica Angle Two^{TM}) with their heads secured and received continuous 1% isoflurane anesthesia. A small

incision was made on the scalp and the skin was opened to expose the skull and the landmarks of bregma and lambda to determine the coordinates for the injection site. A three-axis micromanipulator guided by a digital atlas was used to determine the position of bregma and lambda. Using the micromanipulator software, the injection site was calculated relative bregma and lambda, using computerized coordinates in the digital atlas. To image in vivo calcium transients from CA1 excitatory neurons, 0.2ul of GCaMP6-expressing virus, AAV1-CaMKII-GCaMP6f-WPRE-SV40 (Penn Vector Core: 3.7 x 10^{13} genome copies per ml) was injected into hippocampal CA1 area (AP: -1.94mm; ML: -1.4mm; DV: -1.35mm). The injection site was drilled with a small hole for the delivery of virus. 0.4ul of the GCaMP6-expressing virus was loaded into a glass pipette (tip diameter, ~20-30 μm) and delivered into target region with a Picospritzer (General Valve, Hollis, NH) at a rate of 20 - 30 nl/min with 10 ms pulse duration. The glass pipette was left in the brain for 5 min after injection to prevent the backflow of the virus. After the complexion of the injection, the incision of mouse was closed with tissue adhesive (3M Vetbond, St. Paul, MN). Mice were injected with 5mg/kg Carprofen to mitigate pain and inflammation. Animals were returned to their home cage for recovery. We waited for 3 weeks after the AAV injection, which allows the infected neurons to express sufficient levels of calcium indicators. Then a follow-up procedure was performed to implant a gradient refractive index (GRIN) lens over the injection site.

GRIN lens implantation and baseplate placement

All animals were implanted with a GRIN lens at the target CA1 region for *in vivo* calcium imaging after the AAV-GCaMP injection. A 1.8-mm diameter circular craniotomy was implanted at the following coordinates of the CA1 region: AP: -2.3mm, ML: -1.75mm, DV: -1.55mm. Using a scalpel to incise the skin, we removed connective tissue and dissected muscles from the edge of

the skull. To enhance the stability of microscope implantation and *in vivo* imaging quality, we used a burr (Meisinger, 1/4 Round Steel) to roughen the surface of the skull and to implant a skull screw far away from the implantation area. A center point for the craniotomy was marked on the exposed skull, and surrounding this point, we etch a 1-mm radius cranial window. We carefully removed bone fragments with fine forceps and gently aspirated the exposed tissue with a 27G flat needle until seeing the white striated structure (corpus callosum) above CA1. We then changed to a 29G flat needle for tissue aspiration and stopped when the hippocampus itself was exposed. We then attached the prepared lens holder to the stereotaxic apparatus and gently lowered the GRIN lens to the target area. A small amount of krazy glue was applied around the lens within the craniotomy to cover the exposed tissue. The GRIN lens was fixed to the skull with dental cement (Lang Dental Manufacturing: 1304CLR). A thick layer of Kwik-Sil was applied to the top of the lens to protect it from physical damage. We used a miniscope to check neural calcium activity through the GRIN lens and to adjust the placement of the baseplate for maximal neuron yields.

Open arenas experiment (ensemble activity map analysis, Figure 1.4)

After one week of handling, 12 mice were habituated in the experimental chamber for four consecutive days. The two arenas included a circular box (36 cm in diameter) and a rectangular box (32cm*26cm), each adorned with different distal visual cues on each wall. On the first day, animals with head-mounted miniscopes were to explore in the rectangular arena for 10 minutes. Then after 6 days, which is generally considered sufficient for animals to forget about previous experience, animals ran in the circular arena for 10 minutes.

Open arenas experiment (circle, square and triangle box, Figures 1.3 and 1.5)

After one week of handling, 6 mice were habituated in the experimental chamber for four consecutive days. Animals with a head-mounted scope freely explored within each of three open-

field arenas for 12 minutes. The three arenas included a circular box (36 cm in diameter), a square box (26 cm in length and width) and a triangular box (area 840cm^2) each adorned with different distal visual cues on wall. In between recording sessions, the corncob bedding was changed, and the arenas were cleaned with 10% ethanol. On the first day of habituation, animals with head-mounted miniscopes were first trained in the circular environments for 12 minutes, followed by another 12 minutes in the square box, and then finally they explored in the triangle box in the last 12 minutes. On day two, animals ran in each arena for 12 minutes as was done for day one, but in a different order. The actual experiment uses the same design as habituation.

Barrier experiment (Figure 1.5)

Camk2a-Cre; Ai 163 mice (n=5) implanted with miniscope GRIN lenses at hippocampal CA1 were used for this experiment. Animals underwent water restriction for 1 week, given around 1ml water per day until they reached ~80% of their original body weight. In the meantime, all animals were handled and habituated with a miniscope mounted on the head for 1 week. The recording lasted for two days with 3 sessions each day. The first day contained three training sessions in an empty square box. The second day contained three sessions, including pre-cue (empty square box), cue (square box with a black barrier positioned at the center) and post-cue (empty square box) sessions. For each session, animals were taken out from their home cage and put into a random position in the box at the beginning of the recording. The experimenter added 5-10μL waterdrops every 30 seconds at a random position into the box. The water-deprived mice would search for the waterdrops across the arena. Miniscope imaging and animal behavior data were simultaneously recorded. Each session lasted for 600 seconds. The square box wall was painted in light grey without visual cues. Animals were able to see the surrounding environment

of the room since the box wall was low. The square box had a waterproof mat on the floor. The dimensions of the square box and the barrier were 25cm*25cm*11cm and 12.5cm*12.5cm*1.2cm.

Linear track (Figure 1.5)

6 Mice were handled 5 minutes per day for 3 consecutive days and then trained to run on the linear track during a week of habituation sessions. Water restriction was conducted to motivate animals and the reduction of body weight was controlled within 20%. A 1-meter-long linear track made of black wood was used. 10% ethanol was used for track cleaning between each recording session. Each mouse was placed on the middle of linear track at the beginning of behavior task. The animal was required to run to the end of the track to get 10ul of water reward. Training continued until a minimum of 40 laps per session was achieved. On day 1 of the experimental recording, animals were required to go through 1 session (day 1-horizontal). On the second day, animals went through the same session as day 1 (day 2-horizontal), and then ran another 30 laps after a 90-degree rotation of the linear track relative to the recording environment (day 2-vertical). The animal was held in the experimenter's hand for a one-minute break between the two sessions.

Immobility imaging (Figure 1.6)

3 mice were habituated in their home cage inside dark box for 4 consecutive days. The dark box was dimly illuminated with a blue LED. Animals' position was tracked by an Arlo wire-free camera and was used to determine the immobility periods. On the experimental day, mouse behavior and CA1 neuronal activities were first recorded with the room lights on. The animal was then placed back to the dark box (dim blue LEDs only), and imaging was made during periods of immobility for 10 minutes.

Histology (Figure 1.1)

Mice were transcardially perfused, and the harvested brains were post-fixed in 4% paraformaldehyde overnight, followed by 30% sucrose in phosphate buffered saline for the next day. The brain was then sectioned coronally using a microtome (Leica SM2010R, 30μmslices). Brain slices near the GRIN lens implantation area of hippocampal CA1 were collected and stained with DAPI and mounted on microscope slides. Brain sections were then imaged using a fluorescence BX61 Olympus microscope to visualize fluorescently labeled (GCaMP6+) CA1 cells.

Calcium imaging data preprocessing

Calcium imaging data was downsampled to 15 frames/sec. To adjust for rigid, between-frame movements of the brain relative to the camera, motion correction was applied to the images with an established calcium imaging motion correction pipeline, NormCorre (Eftychios A. Pnevmatikakis & Andrea Giovannucci, 2017) (https://github.com/flatironinstitute/NoRMCorre). The corrected recordings under different conditions were aligned with each other by aligning the neurons that appeared across conditions and were combined prior to neuron extraction.

Extraction of calcium transients in individual neurons using the CNMF-E method

The calcium signals of neurons were extracted from the combined recording using the Extended Constrained Nonnegative Matrix Factorization (CNMF-E) method proposed by Zhou et al (Pengcheng Zhou et al., 2018) (https://github.com/zhoupc/CNMF_E). This method models the recording as follows:

$$y(\mathrm{x}, t) = \sum_{i=1}^{\mathrm{K}} a_i(\mathrm{x}) * c_i(t) + b(\mathrm{x}, t)$$

Where $y(x,t)$ represents the raw video data, $a_i(x)$ represent the neuron's spatial footprint, $c_i(t)$ represents the temporal calcium activity and $b(x,t)$ represents the background activity. The software applies sophisticated background approximation to remove the background component, and by iteratively applying constrained nonnegative matrix factorization to the remaining data, extracts the temporal varying calcium dynamic and the spatial footprint of neurons in the recordings.

We note the footprints of CNMF-E extracted neurons usually have a bright center and gradually fade toward the periphery, while artifacts have uniform brightness or distributed bright spots. To exclude artifacts, we calculated Kullback–Leibler divergence between the footprints and a 2D normal distribution, whose peak locates at the centroid of the footprint and variance equal the variance of the footprint. The Kullback–Leibler divergence gives a value range from 0 to 1 that quantifies the similarity between two distributions, so here it represents the closeness between the actual neuron footprint and the theoretically perfect footprint. For a perfect match, the divergence value is 0. Neurons with divergence values smaller than 0.3 were kept for subsequent analyses. We also applied manual intervention to further remove false detections with aberrant shapes and temporal responses.

Mouse movement tracking

The movement trajectory of the mouse was extracted from overhead videos using a Logitech web camera which has a sample rate of 30 Hz. The floor of any given arena is selected as the region of interest (ROI) to restrict the area for detection of movement. A red LED built into the miniscope is detected inside the ROI of each frame, and its centroid position is captured using customized MATLAB software. The locomotor trajectory is constructed from the positions of red LED across all frames and smoothed with a moving average.

Autocorrelation of temporal dynamics

To quantify the time span of correlated calcium activities in temporal clusters, the calcium signals of all neurons in one cluster are added up together to get the ensemble trace, and the autocorrelation of the ensemble trace is calculated with MATLAB "xcorr" function. Half-length of the higher-than-0 autocorrelation data is considered as the time span of correlated calcium activities.

Spike train and spatial activity map calculation

For activity rate calculations, the calcium spike trains are estimated by applying the CNMF-E embedded deconvolution algorithm, OASIS (Johannes Friedrich et al., 2017), to the extracted temporal calcium dynamics. A threshold of 3 times of the standard deviation of the neurons peak amplitudes is applied for each neuron and spikes lower than the threshold are discarded.

Spatial activity maps are calculated as follows: the locomotor trajectory is downsampled by 2 to be aligned with the calcium responses. In all experiments, the ROI is divided into 1 cm X 1 cm bins. For each bin, the total time the mouse occupied that location is determined as is the total number of events occurring while occupying that bin (C). The spatial event rate for each bin (bin rate) is thus C/bin time. After construction, the activity map is smoothed with a 10 cm x 10 cm 2D Gaussian kernel (delta = 2cm). This is applied to all experiments including linear track and open field arena trials. For linear track, the trajectory and calcium data within 10% of both ends are excluded as they are inside the water reward area. The number of fields is determined by counting the components inside the binarized activity maps in which only the center of the fields with bin rates higher than the 0.5 times of maximal bin rate across the map are preserved.

Ensemble activity map of each cluster is calculated by averaging the activity maps activity maps of all intra-cluster neurons.

Spatial activity map correlations

Activity maps of the same neuron in two different trials are reshaped to 1d vectors, and the Pearson correlation between the reshaped vectors represents the correlation between the corresponding activity maps.

K-mean based consensus clustering (KCC) and optimal cluster numbers (Figure 1.2)

We utilized a clustering method called "k-mean based consensus clustering (KCC)(Wu et al., 2015) with slight modifications to achieve replicable clustering results while automatically determining the optimal cluster number. In detail, we first predefined a range of 2-10 as potential cluster numbers. Then for each potential number, we perform 100 rounds of k-mean clustering. In each round, neuron responses are down-sampled by half, and then linearly interpolated to match the original length. K-means clustering is applied to the interpolated responses with K-means ++ seeding. Pairwise correlations between responses are used as distance for cluster calculation.

The results from 100 clustering rounds are used to build a consensus matrix that contains the pairwise similarity between neuron pairs (i.e. the number of rounds that two neurons fall into the same cluster). To determine the optimal number of clusters, we calculate the cophenetic correlation coefficient of the consensus matrixes corresponding to each of the cluster number candidates. Given a consensus matrix X, and its corresponding dendrogram of Z, the cophenetic correlation coefficient of X is calculated as follows

$$c = \frac{\sum_{i<j}(X_{ij} - \bar{X})(Z_{ij} - \bar{Z})}{\sqrt{\sum_{i<j}(X_{ij} - \bar{X}) \sum_{i<j}(Z_{ij} - \bar{Z})}}$$

Where X_{ij} is the distance between point i and j in matrix, and Z_{ij} is the dendrogram distance between point i and j. The coefficient will be higher if the hierarchical clustering result of the consensus matrix is more robust (Brunet et al., 2004). Hence, inside the predefined range, the consensus matrix with the highest cophenetic correlation corresponds to the optimal cluster number and represents the optimal clustering result.

With the optimal cluster number and its corresponding consensus matrix, hierarchical clustering is performed to the consensus matrix, and the final clustering result is defined at the hierarchical level that gives the optimal number of clusters.

ICA-based clustering

We utilize the ICA-based clustering method described in previous study (Lopes-dos-Santos et al., 2013) (https://github.com/tortlab/Cell-Assembly-Detection). The method returns the weight matrix representing each neuron's contribution toward a specific assembly, and based on that, the assembly time-series can be built from the neuronal activities. For comparison with KCC-based clustering, we used the cluster number determined by KCC-based clustering to the ICA-based algorithm. We utilize all the neurons with weight value larger than 0. For each assembly, the weights of all neurons are sorted, and a neuron will be assigned into the assembly's neural cluster if its weight position is prior to that in other assemblies. If there is a position tie between multiple assemblies, we resolve this by comparing the correlation between the neuron's transient with the assembly and assigning the neuron to the assembly with which it has the highest correlation.

Intra- and inter- cluster pairwise correlation and spatial distance

The pairwise Pearson correlation of calcium signals is calculated for all neuron pairs of each mouse according to their categorization as belonging to the same cluster (intra-cluster) or

different clusters (inter-cluster). Correlations are also determined following 100 randomized shuffles of cluster identity while retaining the same number of neurons in each cluster.

For the pairwise correlation – pairwise distance data. The correlation-distance distribution fits with a first order power function. Wilcoxon matched pair signed rank test is used to test the difference of fit curves of intra- and inter-cluster correlation-distance distribution.

Anatomically contiguous patches of CA1 anatomical space

We used Density-Based Spatial Clustering of Applications with Noise (DBSCAN)(Ester et al., 1996) to isolate the anatomically compact neuron clusters. For each neuron, DBSCAN takes its centroid and counts how many of its neighborhood neurons are within the predefined maximum neighborhood distance L. If the number of qualified neighborhood neurons are higher than the predefined number threshold N, then this neuron and its neighbors form up an anatomically compact neuron cluster. The algorithm continues to perform the same operation until no more clusters are founded and no more neurons are assigned to the existing clusters. We define L as the 95^{th} percentile of the minimum neighborhood distances for all neurons. For N, we choose an arbitrary number 3, which means the smallest anatomical cluster should have at least 3 neurons.

Having defined anatomically compact neuron groups, we define their outer boundaries by connecting the centroids of the most peripheral neurons and use the boundaries to define anatomically contiguous patches. Each cluster may have one or multiple patches. The patch size of each cluster is then calculated as the average size of all its regions. A threshold of 10% maximum patch size is applied to the calculations to minimize the influence of very small patches. To determine the chance level, we shuffle the cluster identities of neurons 100 times, and calculate the patch size for each shuffled clustering result, which formulate a distribution of patch sizes of shuffled clusters. The Wilcoxon matched pair signed rank test is used to test the difference between

the curves of original anatomical cluster patch size and that of averaged shuffled cluster patch size across different cluster number candidates.

Cluster overlap

Cluster overlap is quantified as the percentage of neuron pairs remaining in the same cluster across two independent clustering results. The algorithm is described as follows (Figure 1.1C): Suppose a group of neurons has two clustering results (in different trials for example), P1 and P2, neurons in a specific cluster c of P1 may go into N clusters in P2.

We define:

a_i = number of neurons in cluster c that go into cluster i $(i = 1 \ldots N)$ in P2

S = total number of neurons in cluster c

Then the cluster overlap between c and the corresponding N clusters in P2 is

$overlap = \frac{\sum_{i=1 \ldots N} \binom{a_i}{2}}{\binom{S}{2}}$.

$\left(\frac{a_i}{2}\right)$ means the combinations of all possible two-neuron pairs in a population of a_i neurons. If 0< a_i <=2, $\left(\frac{a_i}{2}\right)$ is replaced with 1, there is only 1 possible combination of these neurons. When a_i = 0, $\left(\frac{a_i}{2}\right)$ is replaced with 0.

If P1 has M clusters, the overall cluster overlap between P1 and P2 will be the average overlap across M clusters:

$$overall\ overlap = \frac{\sum_{i=1 \ldots M}(overlap_i)}{M}$$

The baseline for overall cluster overlap is calculated as the average of 95th percentile for 1000 shuffled overall cluster overlap for all mice.

It is noted that the difference in cluster number may affect the overlap (or non-overlap) of cluster partitions as well. To control this variability, when comparing cluster overlap between different conditions (Figure 1.5), we redo the clustering using a uniform cluster number for each experiment. For circle-square-triangle box, linear track and barrier experiments, the uniform cluster numbers chosen are 5, 4, 4, respectively. In Figure 1.1.7, when comparing the clusters between different periods, we first determine the cluster number using the whole 12 min data, then apply this number to all 6min periods.

Information score and place cell

Information score of recorded neurons is calculated as information per spike (William E. Skaggs et al., 1996). Only the running session with speed larger than 0.5cm/s are included in calculation, and the spatial bins with bin time smaller than 0.1 sec are excluded to avoid non-existed trespass caused by trajectory smoothing. For an activity map with n bins, the information per second is defined as:

$$Information\ Score(bits/spike) = \sum_{i=1}^{n} P_i \frac{\lambda_i}{\lambda} log_2 \frac{\lambda_i}{\lambda}$$

P_i is the probability the mouse stays in the i th bin, which is represented as the ratio between the times in the bin and total times of the trial. λ_i is the firing rate of the i th bin, while λ is the average firing rate across the trial. Place cells are defined by comparing the information score of each neuron with its shuffled baseline. All the time points along the calcium responses will be randomly shuffled 100 times, to randomize their correspondence with behavior and generate a distribution

of potential score values the neuron may achieve. A neuron is determined as a place cell if its original score value is higher than the 95th percentile of the shuffled distribution.

Spatial coherence is used to further trim the selection of place cells by the firing field smoothness. Spatial coherence is calculated as the correlation between the bin rate of each pixel and the averaged bin rate of its 8 neighboring bins (Sijie Zhang et al., 2014). Place cells with spatial coherence higher than 0.4 are selected for further analysis.

TUnCaT processing

The Temporal Unmixing of Calcium Traces (TUnCaT) software were obtained from the official github link (Bao et al., 2022) (https://github.com/YijunBao/TUnCaT). The software requires the original recording video and a mask representing the originally detected neurons. Following the TUnCaT protocol, we used the CNMF-E's neuron footprint as the neuron mask input. We used OASIS to obtain the CNMF-E like calcium trace from TUnCaT generated raw calcium traces for comparisons. We noted that TUnCaT returns empty or aberrant calcium traces for some neurons even they have acceptable CNMF-E calcium traces. We excluded these neurons from the downstream analysis. For the above-threshold peak analysis, we applied gaussian smoothing to the signals (Gaussian window length: 6 sec), as well as a threshold of 0.2 times of the maximum calcium trace amplitude to explicitly target the large activities.

Quantification and statistical analysis

Data are presented as the mean ± SEM. Two-tailed Wilcoxon rank sum test was used for testing statistical significance between distributions of individual mouse. Two sample Kolmogorov–Smirnov tests were used to compare the difference between cumulative distributions. The Wilcoxon matched pairs signed rank test was used to test the cluster size difference across different cluster numbers, as well as to test the pairwise correlation difference

across different pairwise distance. The level of statistical significance was defined as are defined as $p \leq 0.05$ *, $p < 0.01$ **, $p < 0.001$ ***. Statistical test details can be found in the corresponding legends of the figure panels.

Results

Anatomical clustering of temporally correlated neurons

To determine whether the temporally correlated activity of CA1 neurons is related to their anatomical distribution in the hippocampus, we employed miniscope imaging of Ca^{++} transients (Figure 1.1) while mice freely explored one of several environments of different shapes and bearing different sets of boundary wall visual cues (Figure 1.3 A, B). Using the K-means-based consensus clustering algorithm (KCC) that categorizes neurons based on temporal correlation (Wu et al., 2015), we determine that CA1 does indeed exhibit neuron subpopulations activated in sequences spanning several seconds (n = 6 mice). Notably, the sub-populations identified by this method contain many members whose activations are not strictly synchronous or even overlapping in time but nevertheless, fall within the same multi-second windows of time. We observe a strong correlation of neuron-neuron activity vectors within each group and a relatively weak correlation of activity across groups (Figure 1.3 C-D). Temporally correlated activity among members of each group occurs over periods of greater than 3 seconds, approximately following the timeframe identified in recent work that measured synaptic potentiation among neurons active within a few seconds of each other (Bittner et al., 2017). The periods of correlated activation can cover large behavioral movement trajectories in the arena up to >110cm (Figure 1.3 D2).

We then graphed neuron-neuron temporal correlations among all pairs recorded during arena exploration. By organizing the X and Y axes of the correlation matrix according to group identity, neurons of the same group (intra-cluster, Figure 1.3 E) exhibit higher correlations with

each other than with neurons from different groups (inter-cluster, Figure 1.3 E). To determine statistical significance, we constructed cumulative probability functions for all the pairwise correlations between neurons as shown in Figure 1F. The cumulative probability functions for neuron pairs from the same group (purple curve), from different groups (green curve), and after random shuffling of group identities (blue curve) are depicted. Neuron pairs from the same group exhibit significantly higher correlations than when group identities are randomized, and when neurons in pair are not from the same group (Figure 1.3 F). These results further illustrate that the CA1 pyramidal neurons can be organized into distinct groups based on the temporal correlations in their activity.

Having established CA1 neuron group identity based on temporal activity profiles, we then asked whether these groupings exhibit any specific anatomical distributions. To address this, we visualized the anatomical profile of neurons from each temporal cluster across the imaged sub-region of CA1. Strikingly, this reveals that temporally correlated neurons are clustered anatomically into irregularly shaped patches (Figure 1.3 G, left, right for two different example cases). Within such groupings, any given pair of neurons may reside next to each other or be hundreds of microns apart; nevertheless, the members of each group cover one or more contiguous patches of CA1 anatomical space. To test the stability of anatomical clustering across the exploration session, we divided the recording session into several epochs and visualized the distribution of neurons from each temporal grouping in an anatomical map. While CA1 neuron activation across a given space may vary significantly as a function of time, trajectory, or behavior (Fenton et al., 2010; Markus et al., 1995), we found the anatomical clustering defined by temporal correlation exhibit a higher-than-expected level of stability throughout the duration of the

recording session, that among all possible pairs of neurons, on average around 35%-40% of pairs stay in the same cluster across different periods of recording session (Figure 1.3 H, Figure 1.7 J).

We measured the spatial span of anatomical clustering of temporally correlated neurons using density-based spatial clustering of applications with noise (DBSCAN). This algorithm de-noises and defines contiguous populations of individual elements and their boundaries (Ester et al., 1996)(see Figure 1G, lower panels, which show defined contiguous regions; see Figure 1.2 for a description of the method). Across mice, detected contiguous patches have an average area of ~2000 μm^2 over the topographical surface of CA1. In addition, we also observe that anatomical clusters formed by temporally correlated neurons are not always present as one contiguous region. Smaller islands can sometimes be found isolated from the major region, a characteristic we refer to as fractured domain topography.

We then asked whether our clustering algorithm, and the choice of cluster numbers, affect the detected patches. To address this, we first compared the original patch size across mice (i.e., patch size determined by temporally detected clusters), with their corresponding shuffled baseline (i.e., patch size determined by the same data with cluster identities randomized). We found the patch size of original clusters significantly surpass the shuffled baseline (Figure 1.7 N. See Figure 1.7 O for another arena). We then compared the patch size across different cluster numbers, as shown in Figure 1.3 I, where the patch size of original anatomical clusters significantly exceeds the patch sizes of clusters with randomized identities. (See further examples from a different arena in Figure 1.7 G). We also utilized an independent component analysis (ICA)-based algorithm (Lopes-dos-Santos et al., 2013) to examine if our observation is brought by our k-mean based clustering algorithm itself, and find that ICA-based algorithm also picked up both the temporal and anatomical clusters we described previously (Figure 1.14), which indicate the results described

here is not an induced by the clustering algorithm itself. The above analysis shows neither the clustering algorithm, nor the number of clusters chosen, have significant effect in the notability of patches, and that the detected contiguous CA1 patches should be physiologically meaningful.

A potential concern regarding the detected anatomical clusters is that the viral transfection approach we applied may cause unhealthy physiological conditions due to the cellular toxicity of potential viral over-expression. To address this issue, we first examined the histology and morphology of neurons with immunostaining (Figure 1.1). Overall, we do not note CA1 pyramidal neurons exhibiting aberrant shapes which indicate unhealthy conditions. We also checked the length of transients for the virus injection mice used in the experiment (Figure 1.12) and found the most concentrated transient length/duration is around 2-3 sec, which follow the impression of previous studies[64]. Finally, we also applied the same cluster detection technique to a group of 5 Camk2a-Cre; Ai163 mice performing free exploration inside an open square arena. The Ai163 is a Cre-dependent calcium-indicator strain (Daigle et al., 2018) which is less vulnerable to toxicity issues when used in conjunction with the Camk2a-Cre strain. As shown in Figure 1.13 E-I, Camk2a-Cre; Ai163 mice have CA1 excitatory cell clusters that display visually distinguishable anatomical regions that are larger than shuffled baseline across all the potential cluster number candidates. It is noted that the identified anatomical clusters are more fractured in the transgenic mouse cases, which is likely due to less dense transgenic GCaMP expression in CA1 excitatory cells compared with AAV transduction (Figure 1.13). Based on the contents above, we conclude the anatomical clustering of CA1 excitatory cells is unlikely to be induced by virus toxicity.

A second question concerns the potential signal overlap of imaged neural activity between neighboring neurons. To address this, we compared the correlation of neighboring intra- and inter-cluster neurons at the border of each cluster, for mice from different experiments. If the formation

of anatomical clusters is dominated by neighboring neuron interference, the pairwise correlation distribution of neighboring inter-cluster neurons should not be distinguishable from that of neighboring intra-cluster neurons. However, we find that even at the border, neighboring inter-cluster neuron pairs have a significantly lower correlation than border intra-cluster or any intra-cluster neighboring neuron pairs (Figure 1.15). This provides additional evidence that signal overlap cannot explain the formation of the anatomical contiguous patches illustrated here.

Finally, a third problem lies in the possibility that dendritic signals may contaminate the recorded data and give rise to the correlated neighboring components. We first note that this explanation of the data is not consistent with the differences between intra-cluster and extra-cluster pairs at the border between clusters. Nevertheless, we also addressed this concern by utilizing an additional CNMF-E ‘s dendrite detection feature, which can include detected components to be a variety of shapes rather than only ellipse shapes that are considered as typical for soma. We compared the neuron extraction result with the dendrite detection feature being turned on or off and found little difference between the two kinds of extraction (Figure 1.18). The imaged data contains mostly ellipse-shaped components which are predominantly cell soma. We also checked the number of firing fields our detected neurons displayed in the experiments (Figure 1.20). Overall, a high percentage of neurons have two or less fields (~75%), indicating our results are not dominated by components with highly dispersed firing profile.

We also utilized a recently published algorithm, TUnCaT, to unmix and remove the background and dendritic influence from the detected neuron traces (Bao et al., 2022) and examined the effect on cluster detection in six example mice with virus induced GCaMP expression. Comparing the CMNF-E extracted trace and the TUnCaT extracted trace, we note that although most above-threshold peak activities are aligned, some only exist in CNMF-E or TUnCaT

traces (Figure 1.21 B). We therefore quantified the difference between the total above-threshold peak numbers for the original CNMF-E extracted calcium trace and the TUnCaT extracted calcium traces. Overall, across the six mice, most neurons (~90%) have a calcium transient peak number difference <=22 for a duration of 10 minutes of recording, while ~50% of the neurons have a peak number difference <=5 (Figure 1.21 C). Further, we performed cluster detection using the TUnCaT generated calcium traces and examined the patch size of the observed anatomical clusters. We compared the average patch size with its corresponding shuffled baseline across different cluster numbers. Like CNMF-E detected clusters, the patch size of anatomical clusters generated with TUnCaT processed calcium traces significantly exceeds the patch sizes of randomized baseline. (Figure 1.21 E).

Two-photon microscopy distinguishes neuronal and non-neuronal structures. Existing 2-photon studies have provided various views on the anatomical organizations of CA1 neurons discussed above. Modi et al. found similar anatomical contiguous patches that resemble our results after a trace-eyeblink learning task (Modi et al., 2014). Dombeck et al. showed a negative relationship between CA1 pyramidal cell pairwise distance and pairwise correlation when including all neurons in the field of view (Dombeck et al., 2010). While 2-photon calcium imaging is difficult to apply in freely moving mice, we attempted to follow Dombeck et al.'s analysis approach by directly examining the relationship between temporal correlation and distance of recorded principal neuron pairs that have pairwise distances beyond 35μm for this analysis (Dombeck et al., 2010). We found that overall, CA1 principal neuron pairs across mice display a negative relationship between pairwise distance and temporal correlation (Figure 1.3 J cyan line, spearman correlation=-0.1976). This result is consistent with Dombeck et al.'s result that includes all neurons in view. It should be noted though, that Dombeck et al.'s analytical approach is

qualitatively different from our clustering analysis, and may underestimate anatomical clustering because here, any two neurons assigned to the same cluster can be neighboring or distant from each other.

We further examined the distribution of pairwise correlations for intra- and inter- cluster neuron pairs over different distances (Figure 1.3 J, green and purple line). Both intra- and inter-cluster neuron pairs show similar correlation-distance relationships compared to the overall trend. Using the fit curves of intra-cluster and inter-cluster correlation-distance distributions, we find that across a wide range of distance levels, intra-cluster cell pairs exhibit higher pairwise correlation compared to that of inter-cluster cell pairs ($p=3.8966*10^{-18}$, Wilcoxon matched pair signed rank test). This is consistent with the observation that members of a temporally correlated neural cluster can go into multiple anatomically contiguous spaces that are either in proximity or hundreds of microns apart. Meanwhile, consider the results in Figure 1.15, two directly neighboring neurons can be of the same or different clusters, and their temporal correlations will tend to be high and low, respectively. We note here and elsewhere that the form of topographic representation seen in our data differs in character from that tested for in some prior studies (Muller et al., 1987; Redish et al., 2001). In those studies, the tested model most often assumes that all neighboring neurons should have location-specific firing fields near each other, and that neurons at further distances from each other should have proportionally distributed distances between their location-specific firing field centers. This model is derived according to the correlation in location-specific firing activity of hippocampal neurons as opposed to the temporal correlation approach utilized here. The latter and current approach can yield correlations that partially depend on location-specific activity but also allows the specific trajectories through space to define different temporal sequences of activity.

Furthermore, a recent study reported synchronized firing of neighboring CA1 pyramidal neurons after artificial activation of a "seed" CA1 pyramidal neuron using 2-photon microscopy. These synchronized neurons have a high spatial concentration around 50-100 μm range relative to the seed neurons (Geiller et al., 2022). We, therefore, calculated the number of intra-cluster neurons of different distances toward intra-cluster place cells. We used a conservative method to define "place cells" according to quantification of firing activity maps with the metrics coherence and spatial information/event. Spatial information/event measures feature of the distribution in firing rates across environmental locations; values for this measure are high when a small proportion of spatial bins are associated with high activity across a much larger background of inactivity. Coherence complements this measure in reflecting the tendency for high activity spatial bins to be neighboring, as one would expect for a place field. We found that on average, to each place cell the number of neighboring intra-cluster neurons display a similar cell number-distance trend as noted by Geiller et al (Figure 1.3 J right top panel, see Figure 1.8 for anatomical distribution of place cells). This further supports the anatomical organization we describe here.

Anatomical clustering and its relation to location-specific firing

As considered briefly in the preceding section, an important question here concerns how location-specific activity of CA1 cells relates to the identified anatomical distribution of temporally correlated CA1 sub-groups. This is important given that previous results have not identified a one-to-one spatial correspondence between the pairwise anatomical distances and pairwise spatial firing correlations between neurons (Dombeck et al., 2010; Redish et al., 2001).

We first examined the anatomical distribution of place cells. As shown in Figure 1.8 B, place cells are defined according to the distribution in their spatially binned firing rates, and the similarities in rates of neighboring spatial bins, and are observed among all detected anatomical

clusters. Importantly, place cells of the same cluster can either be neighboring each other or have large distances between them. The pairwise distance between intra-cluster place cells, as well as all intra-cluster neurons, is lower than that with all place cell pairs (i.e., independent of their clustering), but there was no significant difference noted between intra-cluster place cells and all intra-cluster cells (Figure 1.8 C). Thus, neurons with strong location-specific activity are just a sub-population of the defined clusters whose activation patterns occur across the same second-long period of time. The pairwise temporal correlation of intra-cluster place cells, and all intra-cluster neurons, are higher than that of all place cell pairs (Figure 1.8 D). Thus, the grouping of neurons by temporal correlation captures neurons that are active over the same second-long period of time, irrespective of whether their activity can be strongly place-specific.

We next examined the relationship of temporally correlated activity to the distribution of location-specific activity for neurons of the same and different clusters. We measured spatially defined activity maps of CA1 neurons by calculating their firing rates within 1cm*1cm spatial bins. We also calculated the averaged spatial activity maps across individual neurons of the same cluster to construct the "ensemble activity map" for that cluster. Interestingly, we find that many temporally correlated CA1 neurons tend to share environmental location-specific tuning, and their ensemble activity clearly maximizes across a specific sub-region of environmental space (Figure 1.4). To quantify the extent of the coverage difference between different neuron clusters, we calculated the pairwise overlap level between ensemble activity maps from all clusters of each individual mice. We define the "major field" as the center portion of ensemble activity maps that have higher than 50% of the maximum activity level across the activity map (Figure 1.11A), and pairwise overlap level is calculated as the ratio between overlapped area and total area of the two major fields. When we pooled the overlap levels from all mice together, we note low level of

overlapping between major fields of a large fraction of ensemble activity map pairs, with 93.21% of pairs having lower than 25% of their major fields overlapping with each other (Figure 1.11C). Similar results were also noted when we only included the place cells in each cluster (Figure 1.16, 1.17).

In the meantime, while many individual intra-cluster neurons have maximal activity within the sub-region covered by cluster ensemble activity map, some neurons within the same temporally defined cluster can have spatially distinct activity distributions, that the firing peaks for individual neurons of a cluster can be distributed across the full space of the environment (Figure 1.4 B, E, H black dots). We think this is consistent with a model in which much of the temporal correlation in activity occurs as a combined consequence of the locations of spatially specific activity for neurons, and the distances as well as trajectories taken by animals across second-long period of time. In this way, many neurons of a cluster will have place fields partially constrained to a sub-region of the arena given that animals may remain in the same area over many second-long periods. Meanwhile, considering Figure 1.8, place cells only constitute part of the intra-cluster neuron populations. Hence, neurons showing activity outside the high ensemble activity region may also be fulfilling their functions differently from place encoding, while they also co-activate with other intra-cluster neurons to support the ensemble cognitive process inside the high ensemble activity region.

To further investigate the interaction between spatial and temporal components of activity correlation within clusters, we also examined the relationships between pairwise temporal correlation and pairwise activity map correlations. Temporal activity correlations are overall positively correlated with spatial map correlations between neuron pairs sharing the same anatomical cluster (Figure 1.4 C, F, I. also Figure 1.9). Meanwhile, at different temporal

correlation levels, the spatial map correlation variates, which follows our observation that intra-cluster neurons can display their primary firing fields at different locations across arena. These results further support our observation that intra-cluster CA1 principal neuron pairs displaying relatively higher temporal correlation also display more similar spatial tunings. Moreover, these results highlight that the anatomical clustering of CA1 neurons discovered herein reflect temporally correlated activation of neuron sub-groups over second-long period, as opposed to an anatomical clustering organized strictly and exclusively by the location-specific firing of neurons.

Anatomical clustering of co-active neuron populations is dynamic

As anatomical clusters exhibit sensitivity to the specific environmental locations visited across time, we asked if different environments would yield different patterns of clustering. To test this, we compared anatomical clustering for temporally-derived neuron sub-groups when animals explored circle-, triangle-, or square-shaped environments (Figure 1.5 A, each environment also bore unique visual cues along their walls). Anatomical clustering based on groupings of temporally correlated neurons was observed for all three environments (Figure 1.5 B). The average spatial activity map correlations between the first and second half of the same sessions, and between sessions recorded in the same environment on different days, did not differ significantly (Figure 1.5 C). However, anatomical clustering appears to vary across days and across environments. We measured the level of cluster overlap both for different environments and for the same environment on different days. The level of cluster overlap is significantly higher than the chance level for all conditions tested (Figure 1.5 D). This shows that CA1 neurons in each anatomical cluster exhibit a degree of stability in their being active across the same second-long period of environmental exploration, which is true for different environments and for the same environment on different days. Though the mean overlap between neurons forming each group

tends to be higher for the same environment as compared to different environments, it is not significant (Figure 1.5 D). We note that cluster overlap across different environments does not imply that the distribution of location-specific firing across neurons is the same for different environments.

We then considered the possibility that an environment yielding more stable and similar trajectories through space might yield more robust stability in anatomical clustering. To test this, we compared anatomical cluster membership and spatial activity patterns when animals traveled along a horizontally- or vertically-oriented linear track (Figure 1.5 E, both track orientations gave a view to the same set of global visual cues in the recording room). As the track defines a space that can be moved or reoriented within a larger, directly visible allocentric space (defined by the recording room walls), activity maps for different configurations of the track relative to the room could be compared for similarity; this was not possible for the open-field arena exploration experiments where an obvious means to align environments is not given. By rotating the track, the global environment perceived by animals for the same locations on the track will be differentiated. The clusters based on groupings of temporally correlated neurons recorded from animals on linear tracks are robust (Figure 1.5 F). We first calculate the spatial activity map correlations between the first and second halves of individual recording sessions, and between two different sessions using the same horizontal orientation. The correlation levels between the halves and same direction trials are in the same level with the lap-by-lap rate map correlation within each trial (Figure 1.19), but are significantly higher than those for the horizontally- versus vertically-oriented track (Figure 1.5 G), indicating a strong influence of location and orientation on spatial firing patterns as expected. The level of cluster overlaps for the first and second halves of each track orientation and across days using the same orientation is beyond that expected by chance

(Figure 1.5 G; comparisons within columns). Next, we asked if there is greater anatomical cluster overlap for the same versus different track orientations. Anatomical clusters have a significantly greater overlap for the same orientation in accordance with the greater degree of pairwise activity map correlations (horizontal or vertical orientation, Figure 1.5 H; comparisons across columns). We attribute the higher clustering overlap for the two horizontal orientation track runs as likely reflecting the constraint on the animal to only two trajectories through the observable environment; this constraint does not characterize the free exploration of the circle, triangle, or square-shaped arenas on different days or across different time periods of the same session.

To further examine how clustering stability may reflect the difference in exploration behavior induced by environment change, we utilized a task in which a barrier is introduced in the center of the square arena, which can alter the exploration trajectory of the animals compared with that of empty arena (Figure 1.5 I, J). Although no significant difference is noted in terms of activity map correlation (Figure 1.5 K), we again noted a significant reduction in cluster overlap between the empty box trials and the barrier trials, while between two open box trials, even on different days, the anatomical cluster overlap shows no significant differences (Figure 1.5 L). Altogether, the above results indicate that anatomical clusters display much stability yet are versatile and dynamic in their organization during active behavioral exploration of different environments.

Anatomical clusters and behavioral state

Having characterized the dynamics and stability of CA1 anatomical clusters of co-active neurons, we next asked if they persist across distinct behavioral states. We compared the behavioral states of active exploration versus immobility within the same environment (Figure 1.6 A, B, F, G). To facilitate immobility, we imaged CA1 neurons while animals were in their home cage inside a dark box under dim lighting. Visual inspection of the layout of temporally correlated

neuron groups during immobile periods revealed that anatomical clusters are as robust as those during behavioral exploration (Figure 1.6 C, D, E, H, I, J). These results indicate that anatomical clusters are present even during immobility.

To determine the significance of anatomical clustering across the behavioral states of active exploration versus immobility, we compared the cumulative probability distribution of intra-cluster and inter-cluster temporal correlations for neuron pairs under active exploration and immobility states. During the exploration period, intra-cluster neuron pair correlations are significantly higher than both shuffled baseline and inter-cluster correlations (Figure 1.6 K). Similarly, during immobility, intra-cluster neuron pair correlations are significantly higher than both shuffled baseline and inter-cluster correlations (Figure 1.6 L). These results suggest that while the temporal correlations in activity seen for anatomical clusters of CA1 neurons are related to the actual exploration pattern for an environment (Figure 1.4), temporal clustering is also subject to the influence of internal dynamics and connectivity. In this way, clustering of activity and anatomical proximity among neuron sub-groups may form CA1 hippocampal activity sequences for encoding and memory of locomotor and non-locomotor episodes.

Discussion

Neighboring neurons with similar response properties form topographic modular structures in sensory areas of the neocortex (Hubel & Wiesel, 1962; Mountcastle, 2003). To date, most approaches to detecting such one-to-one correspondences between the sites of location-specific firing for individual neurons and their locations with the space of CA1 have not found evidence for a strict, metric form of topographic representation of environmental location (Redish et al., 2001; Villette et al., 2015). Instead, hippocampal neurons underlying spatial navigation and memory formation are thought to have a non-topographical, distributed organization. Yet, work

addressing this question has focused on the response properties of very closely neighboring neurons recorded on the same electrode in comparison to neurons recorded on different electrodes at larger distances from each other. Furthermore, these experiments have generated contradictory results (Hampson et al., 1999; Muller et al., 1987; Redish et al., 2001). Neurons with the same place field tuning can be located anywhere in CA1(Redish et al., 2001), yet under more complicated tasks like associating positions with rewards, it has been reported that neurons with the same tuning tend to neighbor one another (Eichenbaum et al., 1989). Similar anatomically organized CA1 principal neuron subpopulations are also identified after association learning (Modi et al., 2014). These results suggest that the anatomical organization of the hippocampus is not yet fully understood and that there may be yet undiscovered principles of connectivity that guide the expression of activity sequences.

Our results show that a very different form of topographical organization not examined in prior work is found when CA1 pyramidal neurons are clustered according to which neurons are activated over second-long time periods. Here, clustering, in the form of cluster members being activated within the same second-long time periods, is accompanied by clustering of members within contiguous areas or 'patches' of the CA1 region being imaged. Notably, this form does not imply that neurons of the same cluster will necessarily exhibit location-specific firing over overlapping locations in the environment. Further, this form does not imply that members of a cluster are adjacent, but, rather, that they lie over a potentially broader spatial range within a contiguous region of CA1; cluster members may be neighboring cells or lie hundreds of microns apart. The CA1 topographical organization of anatomical clusters follows the seconds-scale temporal correlation among large groups of neurons spread over relatively broad regions of anatomical space. Our approach stands in contrast to the approach used in earlier work in which

smaller hippocampal neuron groups of closely-neighboring versus non-neighboring neurons were identified according to whether they had been recorded on the same or a different recording tetrode (Redish et al., 2001). Correlations in the spatial activity maps for same-tetrode versus different-tetrode neuron groups were used to assess the presence or absence of topographic organization. In the present study, we find that neurons with non-overlapping location-specific firing fields can be also assigned to the same cluster, in addition, neurons sharing the same cluster identity can be so anatomically distant from each other that recording them on the same tetrode would be extremely unlikely. For these reasons, we suggest that replication of our findings using electrophysiology in rats or in mice would demand the utilization of a tightly spaced (across anterior-posterior and medial-lateral dimensions) and dense array of recording electrodes. Compared to conventional electrophysiological approaches, optical imaging of cell activity allows for continuous sampling across larger subspaces of the CA1 region to better address the issue of topography and to search for any of multiple forms of it. In the present work, the quantification of temporal correlations between CA1 neurons imaged over a broad view field for several seconds serendipitously yielded discovery of near-neighbor anatomical clustering in the hippocampal CA1 region.

Anatomical clusters in hippocampal sub-region CA1 have several notable anatomical and functional characteristics. First, they are defined in the present work by temporal correlations between CA1 neurons on the order of seconds. Many, but not all, of the recorded neurons exhibit place-specific activity by conservative criteria. By focusing on temporal correlations in firing patterns, our approach examines the dynamics of hippocampal ensembles without employing filters according to a simplified model wherein CA1 excitatory neurons exhibit only single place fields with highly reliable visit to visit activation and robustness to trajectory taken through a location. Thus, at least for active foraging behaviors, the temporal correlations in activity reflect

in part the sequencing of spatially tuned ensemble activity patterns that accompany specific trajectories through an environment. Our approach may also be better able to detect coactivation patterns under circumstances where the recording technique (imaging versus electrophysiological) and/or the species (e.g., rat versus mouse) may be associated with differences in the degree and reliability of spatial tuning. With respect to spatially versus temporally correlated activity, it is also relevant that we observed anatomical clustering for both active exploration and immobile behavioral states. The latter, of course, precludes a spatial approach to defining correlated activity. This suggests that more internally driven dynamics are organized, at least in part, according to the layout of neurons across the space of CA1. A second functional characteristic is that anatomical clusters do not always constitute a single continuous region; a single anatomical cluster may include a non-contiguous island of neurons that is relatively remote from the main cluster. Finally, when we measured anatomical cluster overlap as animals explored different environments, we found that they are dynamic in their organization. In other words, the anatomical distribution of clusters has a "mix-and-match" quality wherein the observed topography is specific to the environment. Temporally correlated clusters of neurons and the sub-regions they occupy in CA1 can be organized in a combinatorial fashion that matches the diversity of experience across environments.

The question as to what circuitry leads to temporal activity correlations for anatomically clustered neurons is complex. Multiple non-random distributions of connectivity co-exist in CA1 including inputs from entorhinal cortex, subiculum, and CA3, all of which vary systematically along the transverse and septo-temporal axes of hippocampus (Witter et al., 2017). Yet, anatomical clustering observed in the present work is dynamic and does not neatly follow obvious medial/lateral or anterior/posterior patterns. Another possible source of anatomical organization

are patterns of hippocampal GABAergic interneuronal axonal arbors. CA1 interneurons are heterogeneous in their dendritic and axonal arbors, and are tightly integrated into the temporal and spatial tuning dynamics of CA1 pyramidal cells (English et al., 2017; Wilent & Nitz, 2007). Through broad-scale changes in firing rates, sub-populations of interneurons appear to influence CA1 pyramidal neuron spatial tuning over the space of experimental arenas such as those used in the present work (Nitz & McNaughton, 2004). Thus, we speculate that the dynamic and fractured topography of CA1 neuron activation patterns observed in the present study are the product of time-based and environment-based dynamic reorganization of activity patterns among CA1 interneurons and the organization of excitatory inputs according to the transverse and longitudinal axes.

Geiller et al.'s recent study provided a model hypothesizing CA1 pyramidal cells are embedded inside a subnetwork including neighboring pyramidal cells and interneurons. In our results, the anatomical distribution of neighboring intra-cluster neurons to place cells, and the distance-temporal correlation relationship of temporally clustered pyramidal neurons is comparable to what Geiller et al. study presented. Our observation is based on different analytical approaches, which make us believe that we are measuring physiological properties of CA1 pyramidal neuron populations rather than coincidence caused by non-neuron structures or specific experimental settings. Meanwhile, the idea of recurrently connected neighboring pyramidal cells could be another potential source of the CA1 pyramidal cell organization we are seeing here and is worth further study.

Overall, our findings imply that episodic memories for random trajectories through an environment may be contained within sub-spaces of CA1 and that activation of CA1 sub-regions could trigger recall of the environmental locations already visited within a single exploration

session. This is consistent with recent work demonstrating that co-activation of neurons over timescales of several seconds can drive the changes in synaptic efficacy that are thought to define memories (Bittner et al., 2017). Alternatively, activation of clusters could be involved in the control of behavioral output itself through CA1 outputs to prefrontal cortex (Dolleman-van der Weel et al., 2019) or retrosplenial cortex (Alexander & Nitz, 2015). Also, anatomical clusters may guide neural activity that contributes to spatial navigation and episodic memory.

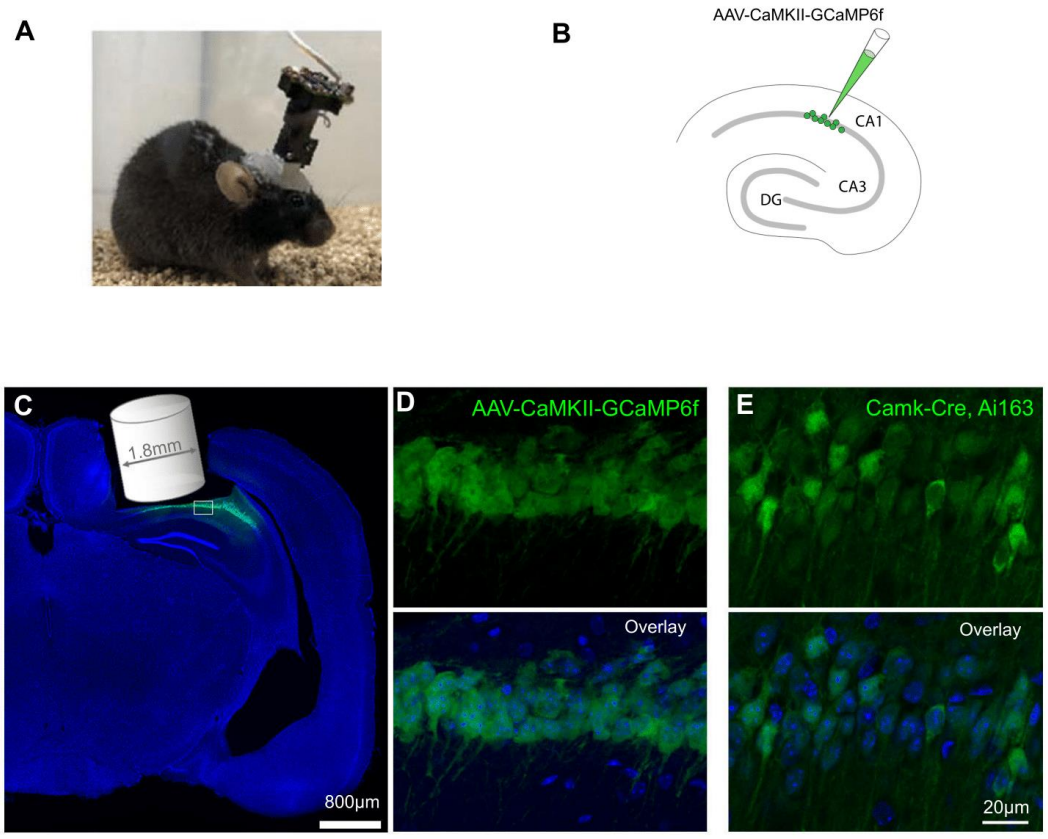

Figure 1.1. GCaMP-based miniscope imaging and mouse preparations (A) Photograph of a mouse fitted with a head-mounted miniscope. (B) Illustration of AAV-CaMKIIGCaMP6f injection into CA1 area for selective expression in excitatory cells. (C) Illustration of a GRIN lens implant site in the coronal brain slice. Our surgical preparation removed overlying cortical tissue without damaging hippocampal tissue. (D) Histological section images of hippocampal CA1 in a C57 mouse with AAV-CaMKII-GCaMP6f expression. Blue color represents DAPI labeled nuclei. (E) Histological section images of hippocampal CA1 in a Camk2a-Crel Ai163 mouse. Note that while both AAV and transgenic preparations appear healthy, the Camk2a-Crel Ai163 preparation shows more sparse GCaMP expression compared with the AAV preparation.

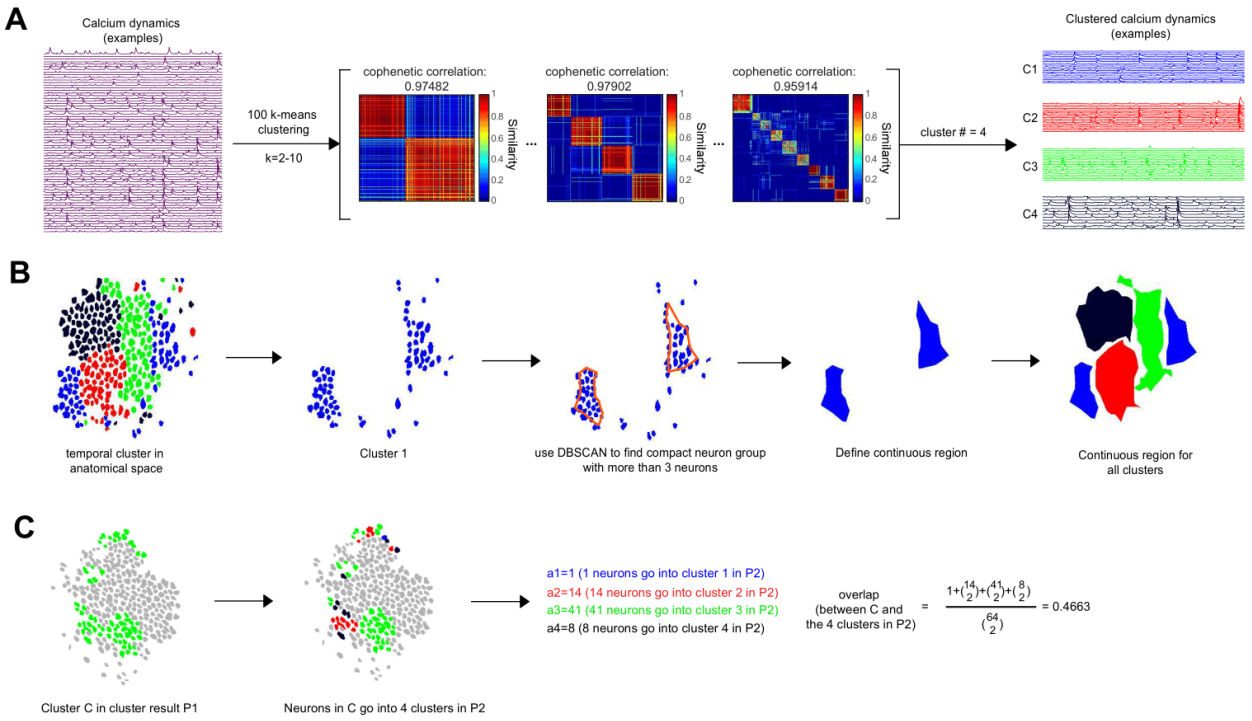

Figure 1.2. Graphical illustrations of temporal calcium activity clusters, anatomical clusters and cluster overlap calculation (A) Illustration of our clustering technique for creating temporal clusters. Starting with raw calcium signals of neurons (left), and candidate clusters numbering over a range of 2-10, 100 rounds of k-mean clustering are performed on the signals (for each neuron a random half is picked during each clustering round). The clustering result is then used to formulate the consensus matrix which represents the similarity between neurons and corresponded to a candidate cluster number (middle). For each consensus matrix, cophenetic correlation is calculated, and the matrix with the highest value. represents the best clustering result, while the corresponding cluster number is the optimal cluster number. (B) Graphical representation of anatomical clusters. Anatomical footprints of individual neurons are labeled with different colors based on their temporal cluster identity (far left panel). DBSCAN is used to identify the anatomically gathered temporal clusters (second on the left). For each anatomical cluster, its outer boundary is defined (middle), and the boundary is filled to achieve the area span of the cluster (second on the right). The area span of each anatomical cluster is mapped and then superimposed (far right panel). (C) Illustration of cluster overlap calculation. Green neurons in the far-left footprint compose one cluster in clustering result P1 for the 1st analytical iteration, these neurons go into different clusters in clustering result P2 for the 2nd analytical iteration (second from the left). For these neurons, cluster overlap is defined as the ratio of the pair of neurons whose assignment remains in the same clusters in P2, and the total pairs of neurons assigned in P1. For other clusters in P1, similar overlap values can be calculated between them and their corresponding clusters in P2, and their average represents the overall overlap between P1 and P2 (far right).

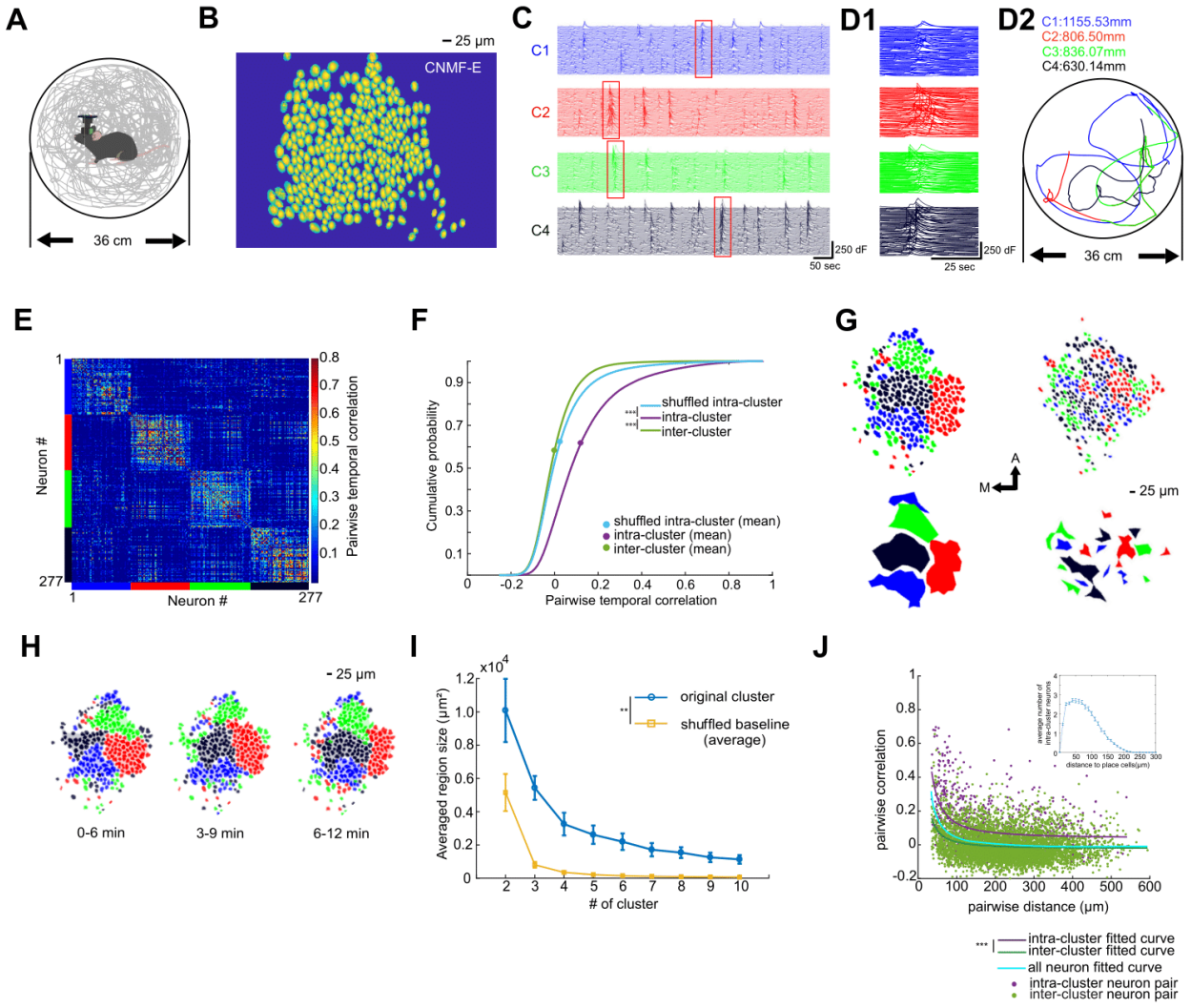

Figure 1.3 Hippocampal CA1 neurons are organized into anatomically clustered groups with temporally correlated calcium activities (A) Illustration of a mouse with a head-mounted miniscope targeting the hippocampal CA1 region, and the behavioral arena (36cm diameter circle box) in which the mouse can freely explore with simultaneous calcium event neural imaging. Gray line indicates the trajectory of one example mice exploring for 12 minutes (B) Illustration of neuron footprints extracted by CNMF-E during processing of miniscope imaging data. (C) Temporal calcium traces of all neurons grouped into clusters recorded from a single mouse (C1-C4) (D1) Magnification of the red boxed areas in C. The aligned calcium events are clearly seen in the magnified trace segment. (D2) Trajectories corresponding to the four magnified calcium event segments presented in d (trajectory length: C1: 1155.53mm, C2: 806.50mm, C3: 836.07mm, C4: 630.14mm) (E) Pairwise temporal correlation matrix. Both axes represent neuron indexes which are grouped by clusters. (F) Comparisons of cumulative probabilities between intra- and inter- cluster pairwise temporal correlations of neuron calcium event dynamics, as well as shuffled intra-cluster pairwise correlation. Intra-cluster correlation is significantly higher than both shuffled and inter-cluster correlation (intra-cluster, 0.1206 ± 0.0006; inter-cluster, 0.0031 ± 0.0006; shuffled intra-cluster, 0.0202 ± 0.0006; intra-cluster versus inter-cluster, $p= 1.0257*10^{-40}$, intra-cluster versus shuffled intra-cluster-cluster, $p= 4.1659*10^{-24}$, two sample Kolmogorov–Smirnov

test, Data are presented as the mean ± SEM). (G) Anatomical clusters of neural calcium event footprints from temporally correlated neurons. Two example mice are shown here. The scale bar represents 25 μm. For the anatomical axis symbols, A refers to anterior and M refers to medial. (H) Anatomical cluster changes during 3 semi-overlapping epochs of a single recording session for the example mouse in G (the left one) (I) Average patch size of anatomical clusters across different cluster numbers. Error bars represent the SEM of patch sizes across six mice perform the same task at the specific cluster number. Blue circle: Patch size of the original anatomical clusters. Yellow square: average size of the shuffled cluster patches serves as shuffled baseline (Original cluster patch size curve v.s. shuffled baseline curve: $p=0.0039$, Wilcoxon matched pairs signed rank test, N=9 cluster numbers) (J) Relationship between pairwise temporal correlations and pairwise anatomical distance of neuron pairs. Intra- and inter-cluster data is represented as purple and green, respectively. The distribution of intra- and inter-cluster data are fitted to a first-order power function. Overall, for all the mice, across neuron pairs with different pairwise distances, a significant negative relationship is identified between pairwise temporal correlation and pairwise distance (Cyan line, spearman correlation=-0.1976, $p=3.9975*10^{-67}$). Also, across neuron pairs with different pairwise distances, the pairwise temporal correlation of intra-cluster neuron pairs is significantly higher than that of inter-cluster neuron pairs ($p=3.8966*10^{-18}$, Wilcoxon matched pair signed rank test, N=100 distance levels). The subplot on the right top illustrates distribution of neighboring cells toward intra-cluster place cells. Asterisks are defined as $p \leq 0.05$ *, $p< 0.01$ **, $p< 0.001$ ***.

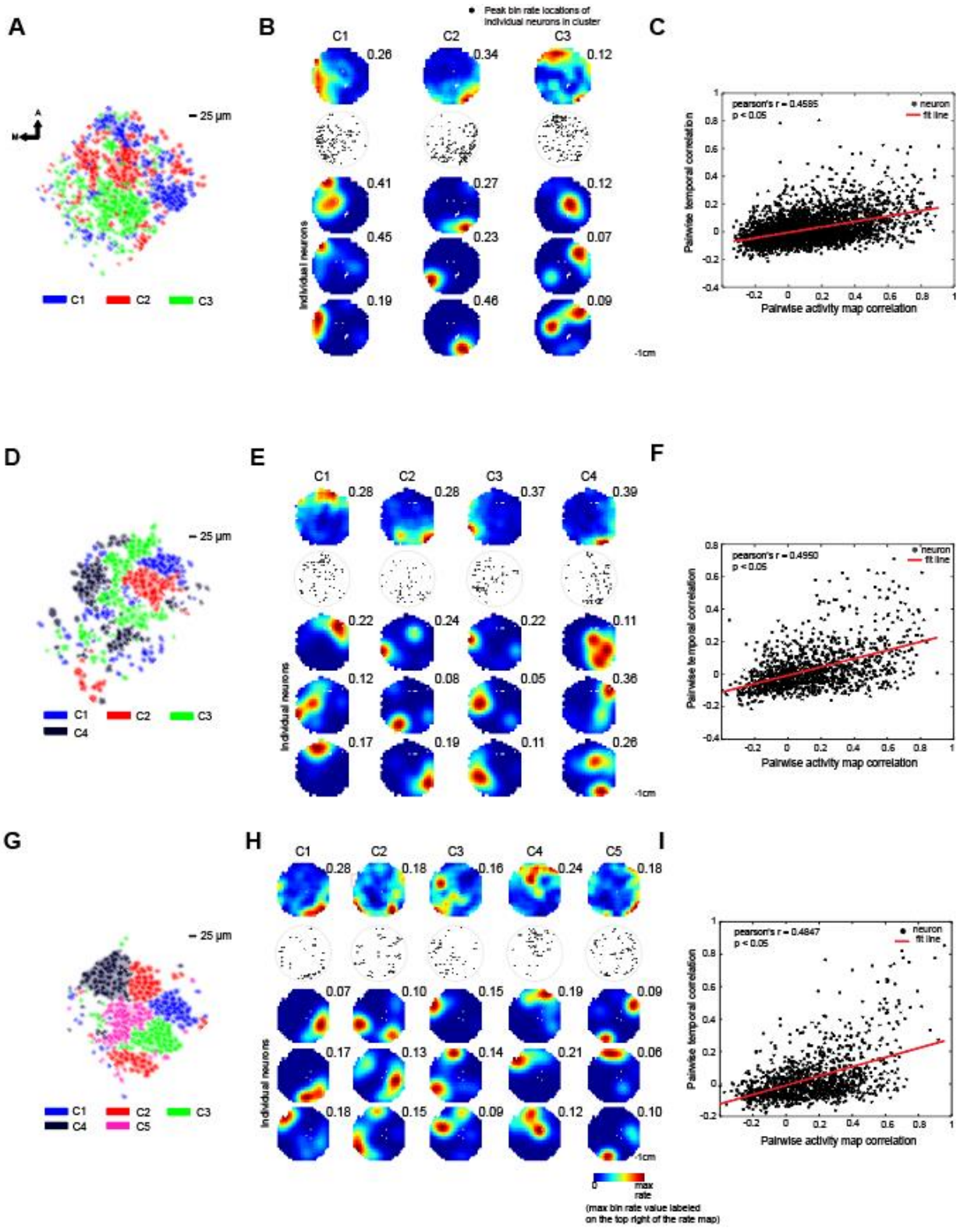
A
25 μm
C1
C2
C3
B
Peak bin rate locations of individual neurons in cluster
C1
C2
C3
0.26
0.34
0.12
0.41
0.27
0.12
0.45
0.23
0.07
0.19
0.46
0.09
Individual neurons
1cm
C
pearson's r = 0.4585
p < 0.05
neuron
fit line
Pairwise temporal correlation
Pairwise activity map correlation
D
25 μm
C1
C2
C3
C4
E
C1
C2
C3
C4
0.28
0.28
0.37
0.39
0.22
0.24
0.22
0.11
0.12
0.08
0.05
0.36
0.17
0.19
0.11
0.26
Individual neurons
1cm
F
pearson's r = 0.4950
p < 0.05
neuron
fit line
Pairwise temporal correlation
Pairwise activity map correlation
G
25 μm
C1
C2
C3
C4
C5
H
C1
C2
C3
C4
C5
0.28
0.18
0.16
0.24
0.18
0.07
0.10
0.15
0.19
0.09
0.17
0.13
0.14
0.21
0.06
0.18
0.15
0.09
0.12
0.10
Individual neurons
1cm
0
max rate
(max bin rate value labeled on the top right of the rate map)
I
pearson's r = 0.4847
p < 0.05
neuron
fit line
Pairwise temporal correlation
Pairwise activity map correlation

Figure 1.4. Anatomical clusters are the basis of the functional organization during exploration of different regions of the behavioral arena (A, D, G) Anatomical clusters for three representative mice imaged while freely exploring an identical behavioral arena. (B, E, H) Upper portion of the panels represents ensemble activity maps of the anatomical clusters in A, E, I. Black dots represent the maximal activity location of individual intra-cluster neurons. Lower portion of the panels represents activity maps of 3 representative neurons from each anatomical cluster. The number on the right top of each activity map represents the maximum bin rate in the map. For all activity maps each bin represent 1cm*1cm of the arena space (C, F, I) Relationship between pairwise temporal correlation and pairwise activity map correlation for neuron pairs within the anatomical clusters for the three representative mice depicted in A, E, I. Each of the neuron pairs is represented by a single black dot. For all 3 example mice, the pairwise temporal correlations have significant linear relationship with pairwise activity map correlation (mouse1: Pearson's r = 0.4585, p=6.1241*10-68; mouse 2: Pearson's r = 0.4950, p=2.6525*10-33; mouse 3: Pearson's r = 0.4847, p=1.8400*10-31).

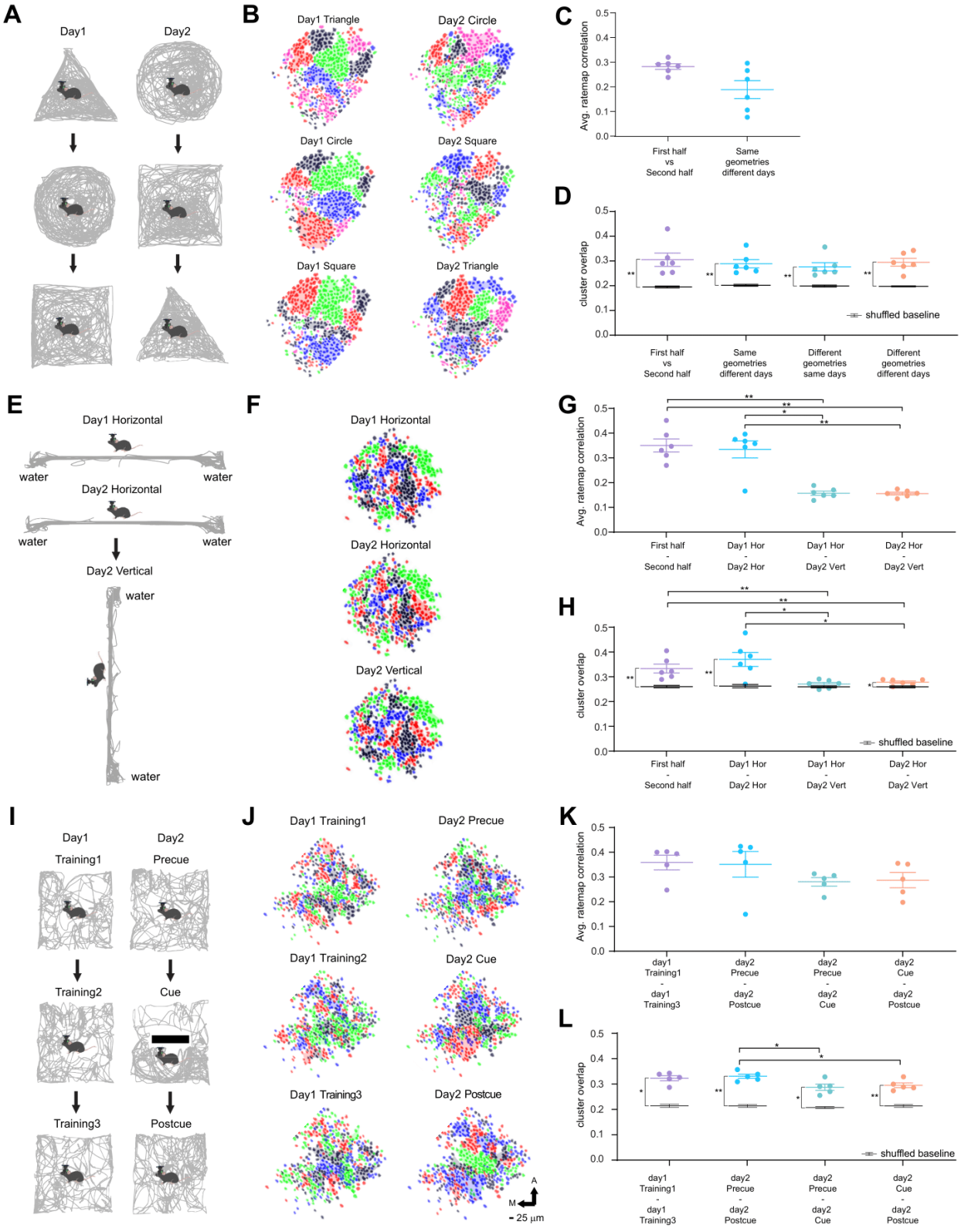
A
Day1
Day2
B
Day1 Triangle
Day2 Circle
Day1 Circle
Day2 Square
Day1 Square
Day2 Triangle
C
Avg. ratemap correlation
First half vs Second half
Same geometries different days
D
cluster overlap
shuffled baseline
First half vs Second half
Same geometries different days
Different geometries same days
Different geometries different days
E
Day1 Horizontal
water
water
Day2 Horizontal
water
water
Day2 Vertical
water
water
F
Day1 Horizontal
Day2 Horizontal
Day2 Vertical
G
Avg. ratemap correlation
First half - Second half
Day1 Hor - Day2 Hor
Day1 Hor - Day2 Vert
Day2 Hor - Day2 Vert
H
cluster overlap
shuffled baseline
First half - Second half
Day1 Hor - Day2 Hor
Day1 Hor - Day2 Vert
Day2 Hor - Day2 Vert
I
Day1
Day2
Training1
Precue
Training2
Cue
Training3
Postcue
J
Day1 Training1
Day2 Precue
Day1 Training2
Day2 Cue
Day1 Training3
Day2 Postcue
A
M
25 µm
K
Avg. ratemap correlation
day1 Training1 - day1 Training3
day2 Precue - day2 Postcue
day2 Precue - day2 Cue
day2 Cue - day2 Postcue
L
cluster overlap
shuffled baseline
day1 Training1 - day1 Training3
day2 Precue - day2 Postcue
day2 Precue - day2 Cue
day2 Cue - day2 Postcue

Figure 1.5. Anatomical cluster-specific calcium event activities vary across different environments (A) Experiment schematic. Six mice explored inside three different types of arenas (triangle, circle and square), each arena for 12 min. The order of exploration in the first and second day is illustrated in the schematic. (B) Anatomical clusters in hippocampal CA1 in one representative mouse for each of these trials. (C) Average activity map correlation between the two halves of each trial and trials with the same geometry on different days. No significant difference is found between the two conditions (first half - second half: 0.2825 ± 0.0113, same geometry different days: 0.1889 ± 0.0363, p=0.0931, two-tailed Wilcoxon rank sum test, Data are presented as the mean ± SEM, N=6 mice). (D) Cluster overlap between the first and second halves of each trial, between the same geometry trials on different days, between different geometry trials on the same day, and between different trials on different days. No significant difference is found between these conditions (first half - second half: 0.2950 ± 0.0155, same geometry different days: 0.3051 ± 0.0268, different geometry same days: 0.2889 ± 0.0168, different geometry different days: 0.2764 ± 0.0168. first half - second half vs same geometry different days: p>0.9999; first half - second half vs different geometry same days: p>0.9999; first half - second half vs different geometry different days: p=0.3939; same geometry different days vs different geometry same days: p=0.8182; same geometry different days vs different geometry different days: p=0.4848; different geometry same days vs different geometry different days: p=0.4848; two-tailed Wilcoxon ranksum test, Data are presented as the mean ± SEM, N=6 mice), while all the cluster overlap distributions are significantly higher than their corresponding shuffled baseline (first half - second half baseline: 0.2117 ± 0.0014, same geometry different days baseline: 0.2125 ± 0.0031, different geometry same days baseline: 0.2166 ± 0.0032, different geometry different days baseline: 0.2124 ± 0.0031, first half - second half vs its baseline: p=0.0022, same geometry different days vs its baseline: p=0.0022, different geometry same days vs its baseline: p=0.0022, different geometry different days vs its baseline: p=0.0022, two-tailed Wilcoxon ranksum test, Data are presented as the mean ± SEM, N=6 mice). (E) Experiment schematic. Six mice conducted exploration on a horizontal linear track on the first day. On the second day they first repeated the exploration on the track with previous day's settings. After that the track was rotated 90 degrees clockwise, and the mice conducted another exploration on the rotated track. (F) Anatomical cluster organization for one representative mouse for each of these three conditions. (G) Average activity map correlation between the first and second halves of the same trials, and between the two horizontal track trials. (First and second halves: 0.3503 ± 0.0261, day 1 horizontal to day 2 horizontal: 0.3343 ± 0.0344, day 1 horizontal to day 2 vertical: 0.1573 ± 0.0085, day 2 horizontal to day 2 vertical: 0.1558 ± 0.0057. first and second half vs day 1 horizontal to day 2 horizontal: p=0.8182, first and second half vs day 1 horizontal to day 2 vertical: p=0.0022, first and second half vs day 2 horizontal to day 2 vertical: p=0.0022, day 1 horizontal to day 2 horizontal vs day 1 horizontal to day 2 vertical: p=0.0087, day 1 horizontal to day 2 horizontal vs day 2 horizontal to day 2 vertical: p=0.0043, day 1 horizontal to day 2 vertical vs day 2 horizontal to day 2 vertical: p=0.9372. two-tailed Wilcoxon rank sum test, Data are presented as the mean ± SEM, N=6 mice). (H) Cluster overlap between the first and second halves of the same trials, between day 1 horizontal to day 2 horizontal, between day 1 horizontal to day 2 vertical, and between day 2 horizontal to day 2 vertical, (First and second halves: 0.3333 ± 0.0177, day 1 horizontal to day 2 horizontal: 0.3702 ± 0.0283, day 1 horizontal to day 2 vertical: 0.2706 ± 0.0283, day 2 horizontal to day 2 vertical: 0.2782 ± 0.0048. first and second half vs day 1 horizontal to day 2 horizontal: p=0.3939, first and second half vs day 1 horizontal to day 2 vertical: p=0.0043, first and second half vs day 2 horizontal to day 2 vertical: p=0.0022, day 1 horizontal to day 2 horizontal vs day 1 horizontal to day 2 vertical: p=0.0260, day

1 horizontal to day 2 horizontal vs day 2 horizontal to day 2 vertical: p=0.0260, day 1 horizontal to day 2 vertical vs day 2 horizontal to day 2 vertical: p=0.4848. two-tailed Wilcoxon rank sum test, Data are presented as the mean ± SEM, N=6 mice). Except day 1 horizontal – day 2 vertical combination, all other cluster overlap distributions are significantly higher than their corresponding shuffled baseline (First and second halves baseline: 0.2616 ± 0.0047, day 1 horizontal to day 2 horizontal baseline: 0.2634 ± 0.0066, day 1 horizontal to day 2 vertical baseline: 0.2606 ± 0.0036, day 2 horizontal to day 2 vertical baseline: 0.2606 ± 0.0036. First and second halves vs its baseline: p=0.0026, day 1 horizontal to day 2 horizontal baseline vs its baseline: p=0.0043, day 1 horizontal to day 2 vertical vs its baseline: p=0.4848, day 2 horizontal to day 2 vertical vs its baseline: p=0.0260, two-tailed Wilcoxon rank sum test, Data are presented as the mean ± SEM, N=6 mice) (I) Experiment schematic. Five mice conducted 10-minute exploration in the same square box for three times on the first day. On the second day a barrier was placed in the middle of the box in the second trial. (J) Anatomical clusters for one representative mouse for the trials described in I. (K) Average activity map correlation for the trial combinations (training1 and training3: 0.3586 ± 0.0294, pre-cue and post-cue: 0.3512 ± 0.0517, pre-cue and cue: 0.2805 ± 0.0173, post-cue and cue: 0.2872 ± 0.0309. training1 and training3 vs pre-cue and post-cue: p=0.4206, training1 and training3 vs pre-cue and cue: p=0.0952, training1 and training3 vs post-cue and cue: p=0.1508, pre-cue and post-cue vs pre-cue and cue: p=0.1508, pre-cue and post-cue vs post-cue and cue: p=0.1508, pre-cue and cue vs post-cue and cue: p>0.9999, two-tailed Wilcoxon rank sum test, Data are presented as the mean ± SEM, N=6 mice). (l) Cluster similarities between the training1 and training3 trial in the first day, and between the pre-cue and post-cue, pre-cue and cue, post-cue, and cue trials in the second day (training1 and training3: 0.3229 ± 0.0099, pre-cue and post-cue: 0.3304 ± 0.0083, pre-cue and cue: 0.2872 ± 0.0123, post-cue and cue: 0.2950 ± 0.0094. training1 and training3 vs pre-cue and post-cue: p=0.8413, training1 and training3 vs pre-cue and cue: p=0.1508, training1 and training3 vs post-cue and cue: p=0.1508, pre-cue and post-cue vs pre-cue and cue: p=0.0317, pre-cue and post-cue vs post-cue and cue: p=0.0317, pre-cue and cue vs post-cue and cue: p=0.6905, two-tailed Wilcoxon rank sum test, Data are presented as the mean ± SEM, N=6 mice). All the cluster overlap distributions are significantly higher than their corresponding shuffled baseline (training1 and training3 baseline: 0.2655 ± 0.0075, pre-cue and post-cue: 0.2607 ± 0.0033, pre-cue and cue: 0.3229 ± 0.0099, post-cue and cue: 0.3304 ± 0.0083. training1 and training3 vs its baseline: p=0.0159, pre-cue and post-cue vs its baseline: p=0.0079, pre-cue and cue vs its baseline: p=0.0159, post-cue and cue vs its baseline: p=0.0079, two-tailed Wilcoxon rank sum test, Data are presented as the mean ± SEM, N=6 mice). Asterisks are defined as $p \leq 0.05$ *, $p < 0.01$ **, $p < 0.001$,***.

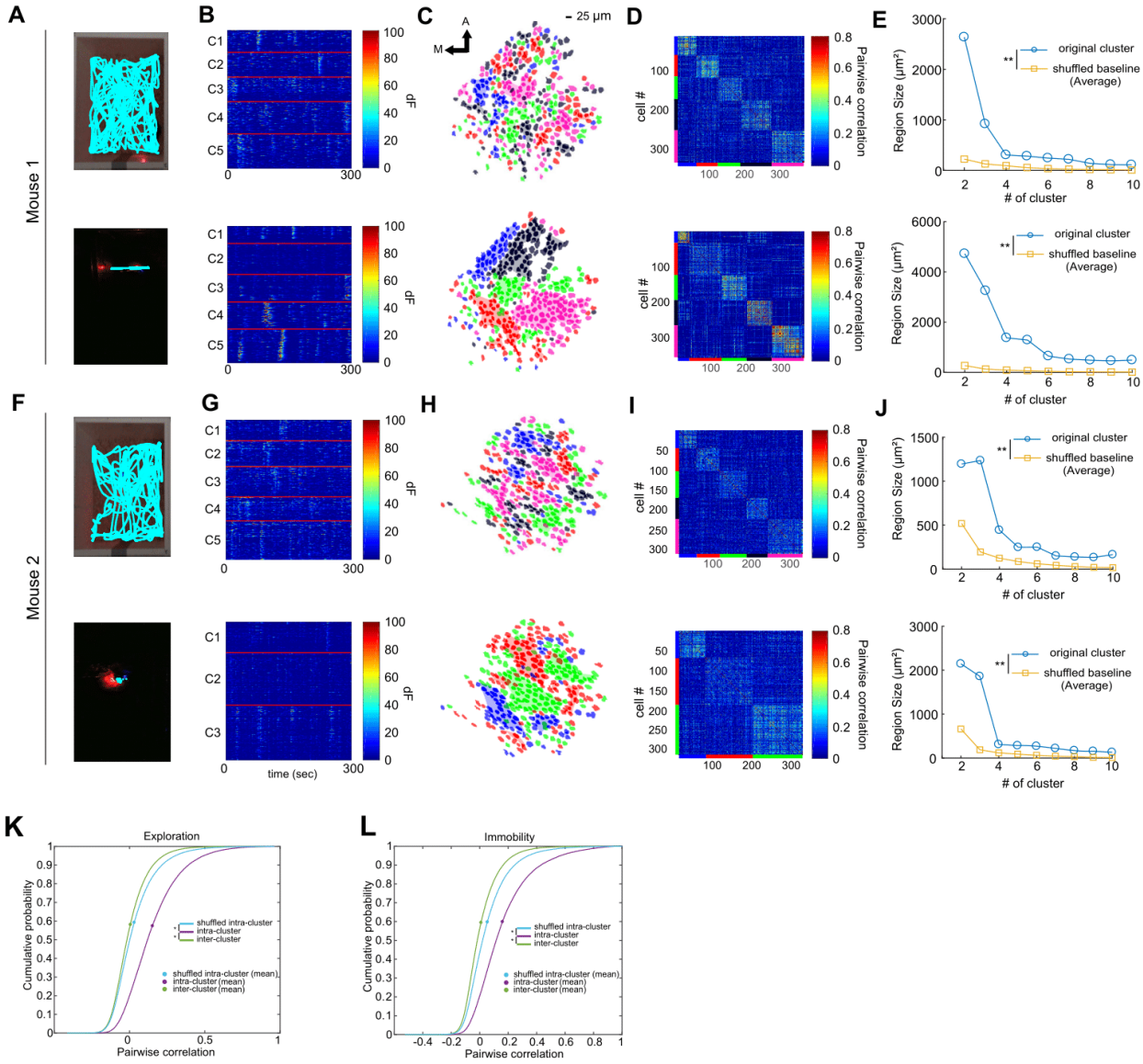

Figure 1.6 . Comparisons of anatomical clusters during active exploration and long-term immobility (A, F; upper portion of each panel) Two example mice actively explored in an open arena (blue traces, square box) (A, F; lower portion of panel) The example mice were immobile in their home cage (square box) which was dimly lit. (B, G; upper portion of panel) Raw calcium activity traces of individual neurons of the mice during active exploration of the arena. (B, G; lower portion of panel) Raw calcium activity trace of individual neurons of the same mice grouped by anatomical clustering during long periods of immobility. (C, H; upper portion of panel) Anatomical clusters during active exploration of the arena by the example mice. (C, H; lower portion of panel) Anatomical clusters during long periods of immobility. (D, I; upper portion of panel) Pairwise correlation matrix of neurons during exploration of the example mice. (D, I; lower portion of panel) Pairwise correlation matrix of neurons during immobility of the example mice. (E, J; upper portion of panel) Anatomical cluster patch size for different number of clusters during exploration. (E, J; lower portion of panel) Anatomical cluster patch size for different number of clusters during immobility. Blue circle: Patch size of the original anatomical clusters. Yellow

square: average size of the distribution of shuffled cluster patches. Overall, original clusters' patch size across different choice of cluster numbers are significantly higher than that of shuffled baseline for both exploration and immobility across different cluster numbers (E upper panel: p=0.0039; E lower panel: p=0.0039; J upper panel: p=0.0039; J lower panel: p=0.0039. Wilcoxon matched pair signed rank test, N=9 cluster numbers) (K, L) Cumulative probability distributions of intra- and inter-cluster pairwise temporal correlations of individual neuron pairs during active exploration (K) or immobile periods (L) for all mice tested. Shuffled intra-cluster pairwise cross correlation is included as well in both K and L. (K) During exploration intra-cluster correlation is significantly higher than both shuffled and inter-cluster correlation (intra-cluster: 0.1422± 0.0010; inter-cluster: 0.0032± 0.0002; shuffled intra-cluster: 0.0314 ± 2.4697*10-5. intra-cluster versus inter-cluster: p=1.9134*10-29, intra-cluster versus shuffled: p=8.4786*10-24, two-sample Kolmogorov–Smirnov test, Data are presented as the mean ± SEM). (L) During immobility the intra-cluster correlation is significantly higher than both shuffled and inter-cluster correlation (intra-cluster: 0.1448 ± 0.0001; inter-cluster: 0.0081 ± 0.0003; shuffled: 0.0491± 2.2288*10-5. intra-cluster versus inter-cluster: p=5.2291*10-22, intra-cluster versus shuffled: p=1.5743*10-12, two-sample Kolmogorov–Smirnov test, Data are presented as the mean ± SEM, N=6 mice). Asterisks are defined as $p \leq 0.05$ *, $p < 0.01$ **, $p < 0.001$,***.

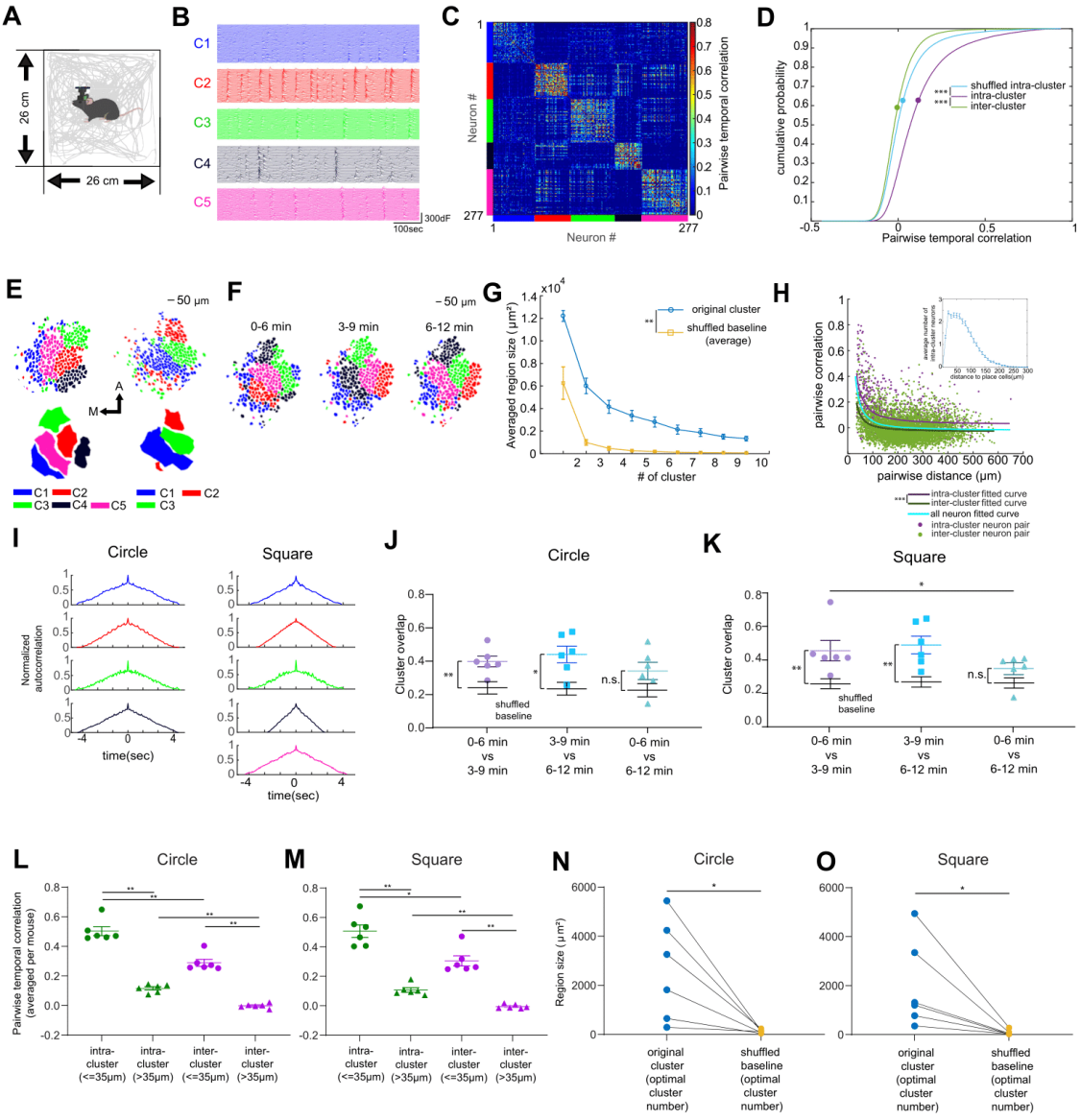

Figure 1.7. Clusters of CA1 excitatory cells observed during mouse exploration in a square arena (A) Square arena experiment design. Six mice explored in a 26cm*26cm square arena for 12 minutes each day. The gray line represents the locomotion trajectory of an example mouse during the experiment. (B) Illustration of temporal raw calcium traces of all neurons, grouped by clusters, of the example mouse. (C) Pairwise correlation matrix of neuron calcium traces of the example mouse. Both axes represent neuron indexes which are grouped by clusters. (D) Comparison between intra- and inter- cluster pairwise cross-correlations of temporal calcium dynamics of neurons, as well as shuffled intra-cluster pairwise cross correlations, for all 6 mice. The intra-cluster correlation is significantly higher than both shuffled baseline and inter-cluster correlation (intra-cluster: 0.1163 ± 0.0006; inter-cluster: -0.0044 ± 0.0001; shuffled intra-cluster: 0.0280 ± 0.0000. intra-cluster vs. inter-cluster: $p=1.1998*10^{-149}$, two sample Kolmogorov–Smirnov test, intra-cluster vs. shuffled intra-cluster-cluster: $p=4.0483*10^{-89}$, two sample Kolmogorov–Smirnov test, Data are presented as the mean ± SEM, N=6 mice). (E) The anatomical

footprint of temporal clusters, and contiguous patches of CA1 anatomical space detected by DBSCAN. Each cluster is represented by a single color. Two example mice are shown here. (F) Anatomical formation of temporal clusters for three 6-minute periods window of the experiment. (G) The anatomical cluster patch sizes across different numbers of clusters, for all 6 mice. Blue circle: Region size of the original anatomical clusters. Yellow square: average size of the shuffled cluster regions. (Original cluster size curve vs. shuffled baseline curve: p=0.0039, Wilcoxon matched-pairs signed rank test, N=9 cluster numbers) (H) Relationship between pairwise temporal correlations and pairwise anatomical distances of neuron pairs, in square arena exploration. Intra- and inter-cluster data are represented as purple and green, respectively. The distribution of intra- and inter-cluster data are fitted to a first-order power function. Overall, across neuron pairs from all mice, a significant negative relationship is identified between the pairwise temporal correlation and pairwise distance (Cyan line, spearman correlation=-0.2141, $p=3.5514*10^{-81}$). Across neuron pairs with different pairwise distances, the pairwise temporal correlation of intra-cluster neuron pairs is significantly higher than that of inter-cluster neuron pairs ($p=3.8966*10^{-18}$, Wilcoxon matched pair signed rank test, N=100 distance levels). The subplot on the right top illustrates the distribution of neighboring cells toward intra-cluster place cells. (I) Autocorrelation of the ensemble calcium activity of each cluster of the example mouse. The maximum autocorrelation values are normalized to 1 (left: circle arena trial in Figure 1; right: square arena trial in panel A). (J) Cluster overlap between the three 6-min periods during the experiment, for the circle arena trial (Figure 1). Cluster overlap between the three period do not show a significant difference (0-6 min -- 3-9 min: 0.3984 ± 0.0320; 3-9 min -- 6-12 min: 0.4407 ± 0.0496; 0-6 min -- 6-12 min: 0.3419 ± 0.0520. 0-6 min -- 3-9 min vs 3-9 min -- 6-12 min: p=0.4848; 0-6 min -- 3-9 min vs 0-6 min -- 6-12 min: p=0.2403; 3-9 min -- 6-12 min vs 0-6 min -- 6-12 min: p=0.3095. Two-tailed Wilcoxon rank sum test, Data are presented as the mean ± SEM, N=6 mice). The baseline was achieved by shuffling the cluster identities of neurons in different periods. Between 0-6 min and 3-9min or 3-9min and 6-12min windows, the cluster overlap is significantly higher than baseline, while between 0-6min and 6-12min the cluster overlap does not significantly different from baseline (0-6 min -- 3-9min to baseline: p=0.0087, 3-9 min -- 6-12min to baseline: p=0.0152, 3-9 min -- 6-12min to baseline: p=0.1320. Two-tailed Wilcoxon rank sum test, N=6 mice). (K) Cluster overlap between the three 6 min windows during the experiment, for the square
arena trial (panel a). 0-6min and 3-9min period is significantly higher than between 0-6min and 6-12min windows (0-6 min -- 3-9 min: 0.4611 ± 0.0580; 3-9 min -- 6-12 min: 0.4847 ± 0.0550; 0-6 min -- 6-12 min: 0.3465 ± 0.0352. 0-6 min -- 3-9 min vs 3-9 min -- 6-12 min: p=0.8182; 0-6 min -- 3-9 min vs 0-6 min -- 6-12 min: p=0.0411; 3-9 min -- 6-12 min vs 0-6 min -- 6-12 min: p=0.0931. Two-tailed Wilcoxon rank sum test, Data are presented as the mean ± SEM, N=6 mice). Between 0-6 min and 3-9min or 3-9min and 6-12min windows, the cluster overlap is significantly higher than baseline, while between 0-6min and 6-12min the cluster overlap does not significantly different from baseline (0-6 min -- 3-9min to baseline: p=0.0087, 3-9 min -- 6-12min to baseline: p=0.0087, 3-9 min -- 6-12min to baseline: p=0.0931. Two-tailed Wilcoxon rank sum test, N=6 mice). (L) Average pairwise correlations of intra-cluster neuron pairs and inter-cluster neuron pairs that are anatomically close (center distance<=35um) or far away (>35um), in the circle arena experiment described in Figure 1. Neurons that are anatomically close show significantly higher pairwise correlation than far away neurons, and intra-cluster neuron pairs show significantly higher correlation than inter-cluster neuron pairs (intra-cluster(<=35μm): 0.5025±0.0301; intracluster(>35μm): 0.1158±0.0236; inter-cluster(<=35μm): 0.2886±0.0236; inter-cluster(>35μm): -0.0022±0.0064; intra-cluster(<=35μm) vs intra cluster(>35μm): p=0.0022; inter-

cluster(<=35μm) vs. inter-cluster(>35μm): p=0.0022; intra-cluster(<=35μm) vs. inter-cluster(<=35μm): p=0.0022; intra-cluster(>35μm) vs inter-cluster(>35μm): p=0.0022. Two-tailed Wilcoxon rank sum test, Data are presented as the mean ± SEM, N=6 mice). (M) Average pairwise correlation of intra-cluster neuron pairs and inter-cluster neuron pairs that are anatomically close (center distance<=35um) or far away (>35um), in the square arena experiment described in the current figure. Neurons that are anatomically close have significantly higher pairwise correlation than far away neurons, and intra-cluster neuron pairs have a significantly higher correlation than inter-cluster neuron pairs (intra-cluster(<=35μm): 0.5069±0.0424; intra-cluster(>35μm): 0.1072±0.0154; intercluster(<=35μm): 0.3052±0.0348; inter-cluster(>35μm): -0.0050±0.0059; intra-cluster(<=35μm) vs intra cluster(>35μm): p=0.0022; inter-cluster(<=35μm) vs inter-cluster(>35μm): p=0.0022; intra-cluster(<=35μm) vs inter-cluster(<=35μm): p=0.0156; intra-cluster(>35μm) vs inter-cluster(>35μm): p=0.0022. Two-tailed Wilcoxon rank sum test, Data are presented as the mean ± SEM, N=6 mice). (N, O) Comparison of original cluster patch size and shuffled baseline, for each of the 6 mice with their optimal cluster numbers. All mice have their original cluster patch size surpassing their own baseline (Panel N (circle): original cluster patch size: 2619 ± 835.5 μm^2, shuffled baseline patch size: 130.4 ± 28.2 μm^2, p=0.0319; Panel O (square): original cluster patch size: 1988 ± 725.6 μm^2, shuffled baseline patch size: 84.52 ± 40.79 μm^2, p=0.0319. Wilcoxon matched pair signed rank test, Data are presented as the mean ± SEM, N=6 mice). Asterisks are defined as $p \leq 0.05$ *, p< 0.01,**, p< 0.001,***.

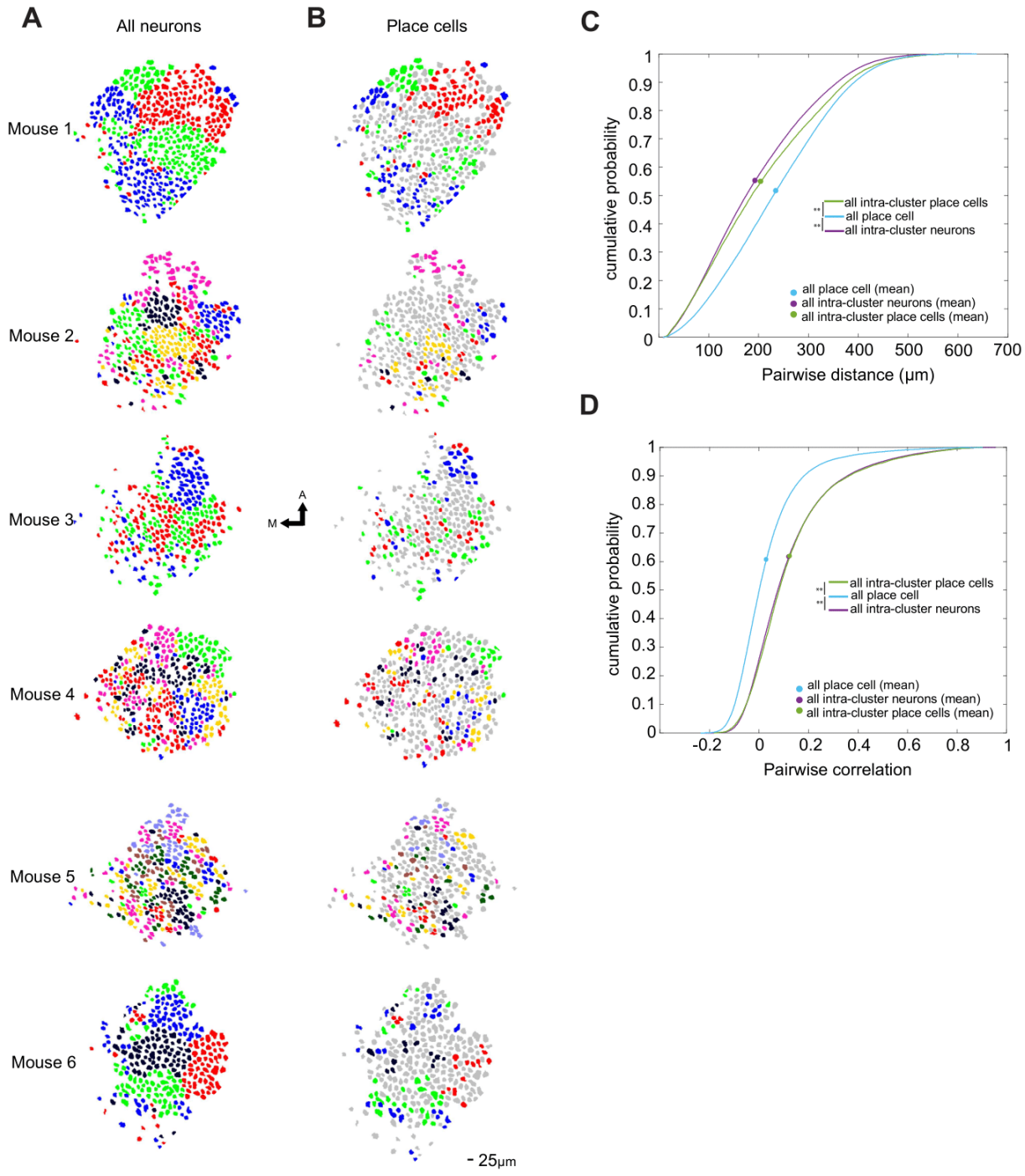

Figure 1.8. Anatomical distributions of place cells in the clusters observed in the circle arena exploration experiment (A) Anatomical footprints of all neurons with their cluster identities illustrated by different colors (B) Detected place cells and their location in anatomical footprints, labeled with colors indicating their cluster identities (C) Pairwise distance of all intra-cluster neurons, intra-cluster place cells, and all place cells. The pairwise distance distributions of intra-cluster place cells, as well as all intra-cluster neurons, are significantly lower than that of all place cells, but not significantly different from all intra-cluster neurons (Intra-cluster place cells:

195.1612 ± 0.8564μm, intra-cluster all neurons: 193.0436 ± 0.3770μm, all place cells: 230.0036 ± 0.3997μm. Intra-cluster place cells vs intra-cluster all neurons: p=0.6976; intra-cluster place cells vs all place cells: $p=8.6730*10^{-6}$, intra-cluster all neurons vs all place cells: $p=6.4860*10^{-8}$, two sample Kolmogorov–Smirnov test, Data are presented as the mean ± SEM) (D) Pairwise temporal correlation of all intra-cluster neurons, intra-cluster place cells and all place cells. Intra-cluster place cells, as well as all intra-cluster neuron pairs, display slightly stronger pairwise correlations toward all place cell pairs including intra- and inter-cluster pairs (Intra-cluster place cells: 0.1285 ± 0.0013, intra-cluster all neurons: 0.1203 ± 0.0006, all place cells: 0.0285 ± 0.0005. Intra-cluster place cells vs intra-cluster all neurons: p=0.6048; intra-cluster place cells vs all place cells: $p=5.8780*10^{-13}$, intra-cluster all neurons vs all place cells: $p=9.7433*10^{-22}$, two sample Kolmogorov–Smirnov test, Data are presented as the mean ± SEM). Asterisks are defined as $p \leq 0.05$ *, p< 0.01,**, p< 0.001,***.

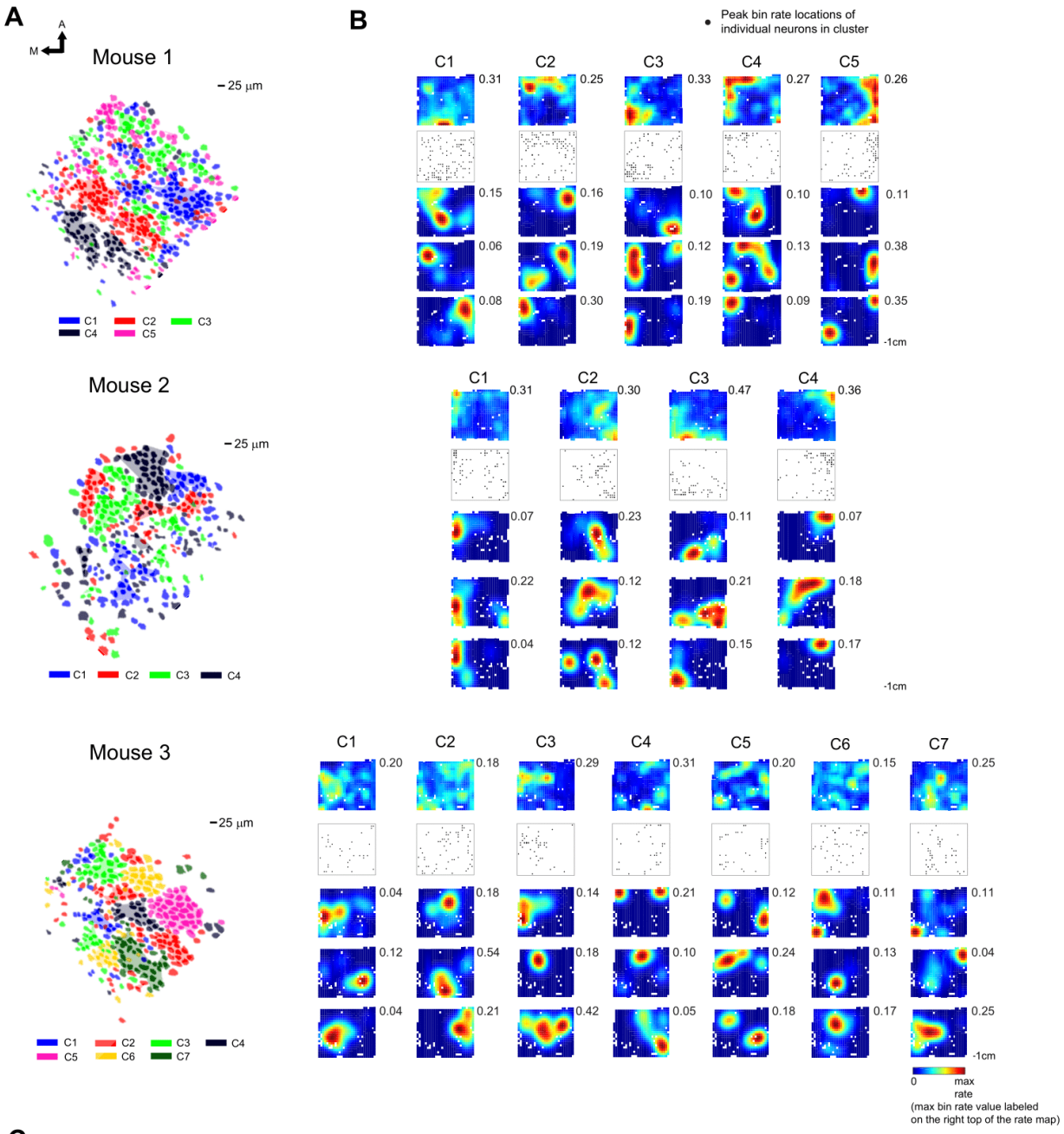
A
A
M
Mouse 1
25 μm
C1
C2
C3
C4
C5
Mouse 2
25 μm
C1
C2
C3
C4
Mouse 3
25 μm
C1
C2
C3
C4
C5
C6
C7
B
Peak bin rate locations of individual neurons in cluster
C1
C2
C3
C4
C5
0.31
0.25
0.33
0.27
0.26
0.15
0.16
0.10
0.10
0.11
0.06
0.19
0.12
0.13
0.38
0.08
0.30
0.19
0.09
0.35
-1cm
C1
C2
C3
C4
0.31
0.30
0.47
0.36
0.07
0.23
0.11
0.07
0.22
0.12
0.21
0.18
0.04
0.12
0.15
0.17
-1cm
C1
C2
C3
C4
C5
C6
C7
0.20
0.18
0.29
0.31
0.20
0.15
0.25
0.04
0.18
0.14
0.21
0.12
0.11
0.11
0.12
0.54
0.18
0.10
0.24
0.13
0.04
0.04
0.21
0.42
0.05
0.18
0.17
0.25
-1cm
0
max rate
(max bin rate value labeled on the right top of the rate map)
C
Mouse 1
pearson's r=0.3187
p<0.05
Pairwise temporal correlation
Pairwise activity map correlation
Mouse 2
pearson's r=0.3624
p<0.05
Pairwise activity map correlation
Mouse 3
pearson's r=0.2335
p<0.05
neuron
fit line
Pairwise activity map correlation

Figure 1.9. CA1 neuron clusters and their relationships with the spatial activity maps in the square arena exploration (A) Anatomical footprints and continuous neuron regions in hippocampal CA1 of three typical mice. (B) Ensemble activity maps of individual clusters, as well as activity maps of 3 example neurons inside the cluster, for the example mouse shown in B. The number on the right top of each activity map represent the maximum bin rate in the map (C) Relationship between pairwise temporal correlations and pairwise activity map correlation, for the three example mice shown in B. Each neuron pair is represented by a single black dot. For all 3 example mice, the pairwise temporal correlations show a significant linear relationship with the pairwise activity map correlation (mice1: Pearson rho = 0.3187, $p=8.6543*10^{-32}$; mice2: Pearson rho = 0.3624, $p=8.4029*10^{-18}$; mice3: Pearson rho = 0.2335, $p=1.5445*10^{-8}$).

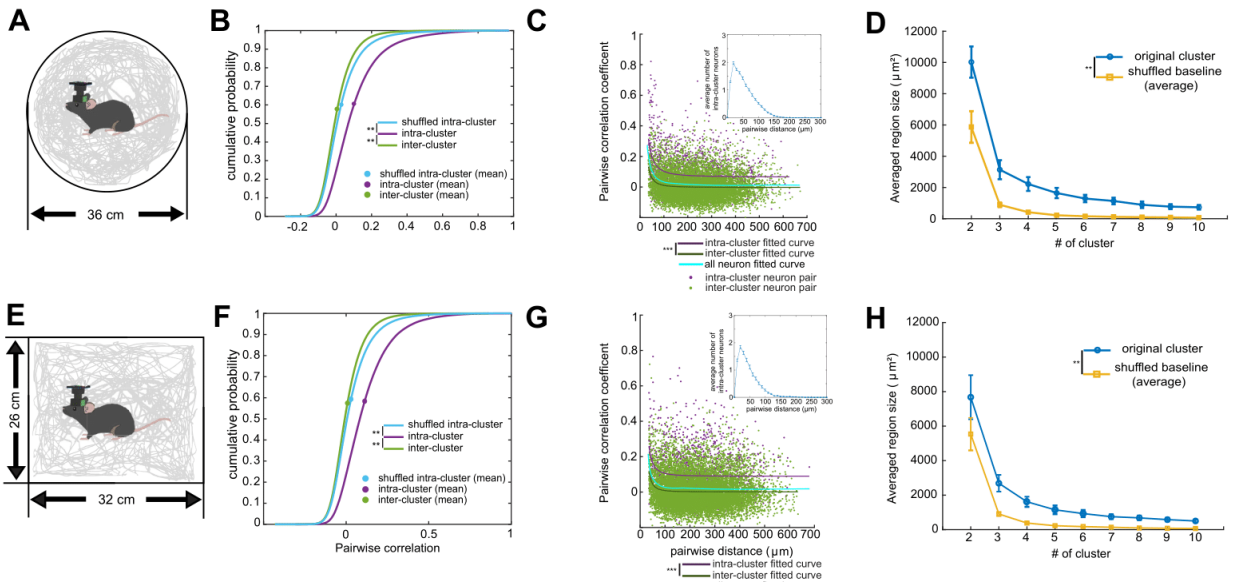

Figure 1.10. Cluster profile for mice in the ensemble activity map analysis (A) 12 mice explored in a 36cm diameter circle arena for 12 minutes each day. The gray line represents the locomotion trajectory of an example mouse during an experiment. (B) Comparison between intra- and inter- cluster pairwise cross-correlation of temporal calcium dynamics of neurons, as well as shuffled intra-cluster pairwise cross-correlation, for all 12 mice. Intra-cluster correlation is significantly higher than both randomized baseline and inter-cluster correlation (intra-cluster: 0.1020 ± 0.0003; inter-cluster: 0.0065 ± 0.0001; shuffled intra-cluster: 0.0283 ± 0.0000. intra-cluster vs. inter-cluster: p= $2.5131*10^{-125}$, intra-cluster vs. shuffled intra-cluster-cluster: p= $1.1876*10^{-85}$, two sample Kolmogorov–Smirnov test, Data are presented as the mean ± SEM). (C) Relationship between pairwise temporal correlations and pairwise anatomical distance of neuron pairs, in the square arena exploration. Intra- and inter-cluster data are represented as purple and green, respectively. The distributions of intra- and inter-cluster data are fitted to a first-order power function. Overall, across neuron pairs from all mice, a significant negative relationship is identified between pairwise temporal correlation and pairwise distance (Cyan line, spearman correlation=-0.0973, p=$3.4393*10^{-34}$). Across neuron pairs with different pairwise distances, the pairwise temporal correlation of intra-cluster neuron pairs is significantly higher than that of inter-cluster neuron pairs (p=$3.8966*10^{-18}$, Wilcoxon matched pair signed rank test, N=100 distance levels). The subplot on the right top illustrates the distribution of neighboring cells toward intra-cluster place cells. (D) The cluster patch sizes change across the different number of clusters, for all 12 mice in the circle arena trial. Blue circle: Patch size of the original anatomical clusters. Yellow square: average size of the shuffled cluster patches. (Original cluster size curve vs. shuffled baseline curve: p=0.0039, Wilcoxon matched pairs signed rank test, N= 9 cluster numbers) (E) Experiment design. 12 mice in 12-minute exploration in a 32cm*26cm rectangle arena for one day. The gray line represents the trajectory of an example mouse during an experiment. (F) Comparison between intra- and inter- cluster pairwise cross-correlation of temporal calcium dynamics of neurons, as well as shuffled intra-cluster pairwise cross-correlation, for all 12 mice. Intra-cluster correlation is significantly higher than both shuffled baseline and inter-cluster correlation (intra-cluster: 0.1123 ± 0.0004; inter-cluster: 0.0079± 0.0001; shuffled intra-cluster: 0.0297 ± $9.2812*10^{-6}$. intra-cluster vs. inter-cluster: p=$9.0350*10^{-18}$, intra-cluster vs. shuffled

intra-cluster-cluster: p= $1.1924*10^{-12}$, two sample Kolmogorov–Smirnov test, Data are presented as the mean ± SEM). (G) Relationship between pairwise temporal correlations and pairwise anatomical distance of neuron pairs, in the square arena exploration. Intra- and inter-cluster data is represented as purple and green, respectively. The distribution of intra- and inter-cluster data are fitted to a first-order power function. Overall, across neuron pairs from all mice, a significant negative relationship is identified between pairwise temporal correlation and pairwise distance (Cyan line, spearman correlation=-0.0613, $p=1.8120*10^{-14}$). Across neuron pairs with different pairwise distances, the pairwise temporal correlation of intra-cluster neuron pairs is significantly higher than that of inter-cluster neuron pairs ($p=3.8966*10^{-18}$, Wilcoxon matched pair signed rank test, N=100 distance levels) The subplot at the top right illustrates the distribution of neighboring cells toward intra-cluster place cells. (H) The cluster patch sizes change across the different number of clusters, for all 12 mice in the square arena trial. Blue circle: Region size of the original anatomical clusters. Yellow square: average size of the shuffled cluster regions. (Original cluster size curve vs. shuffled baseline curve: p=0.0039, Wilcoxon matched-pairs signed rank test, N=9 cluster numbers) . Asterisks are defined as $p \leq 0.05$ *, p< 0.01**, p< 0.001,***.

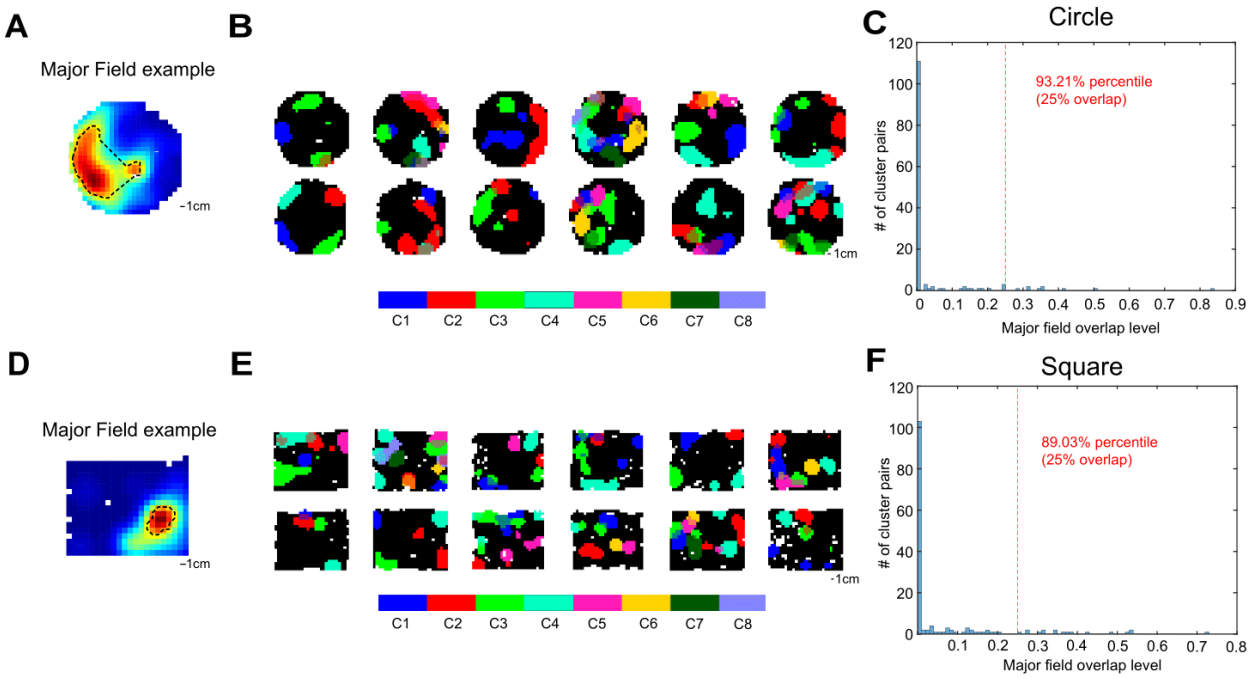

Figure 1.11. Overlap analysis of cluster-specific ensemble activity maps (A) Illustration of a major field encircled by the dashed line, in an ensemble activity map of one neuronal cluster, for the circle arena exploration. (B) Illustration of all major fields calculated from all specific-cluster ensemble activity maps for each individual mouse during the circle arena exploration. Major fields of different clusters are labeled with corresponding colors on the scale. (C) Distribution of major field overlap levels of cluster ensemble activity map pairs. Across mice, 93.21% of the cluster pairs have their major field overlap level smaller than 25%. (D) Illustration of a major field encircled by the dashed line, in an ensemble activity map of one neuronal cluster, for the rectangle arena exploration. (E) Illustration of all major fields calculated from all specific-cluster ensemble activity maps for each individual mouse during the rectangle arena exploration. Major fields of different clusters are labeled with corresponding colors (F) Distribution of major field overlap levels of cluster ensemble activity map pairs. Across different mice, 89.03% of the cluster pairs have their major field overlap level smaller than 25%.

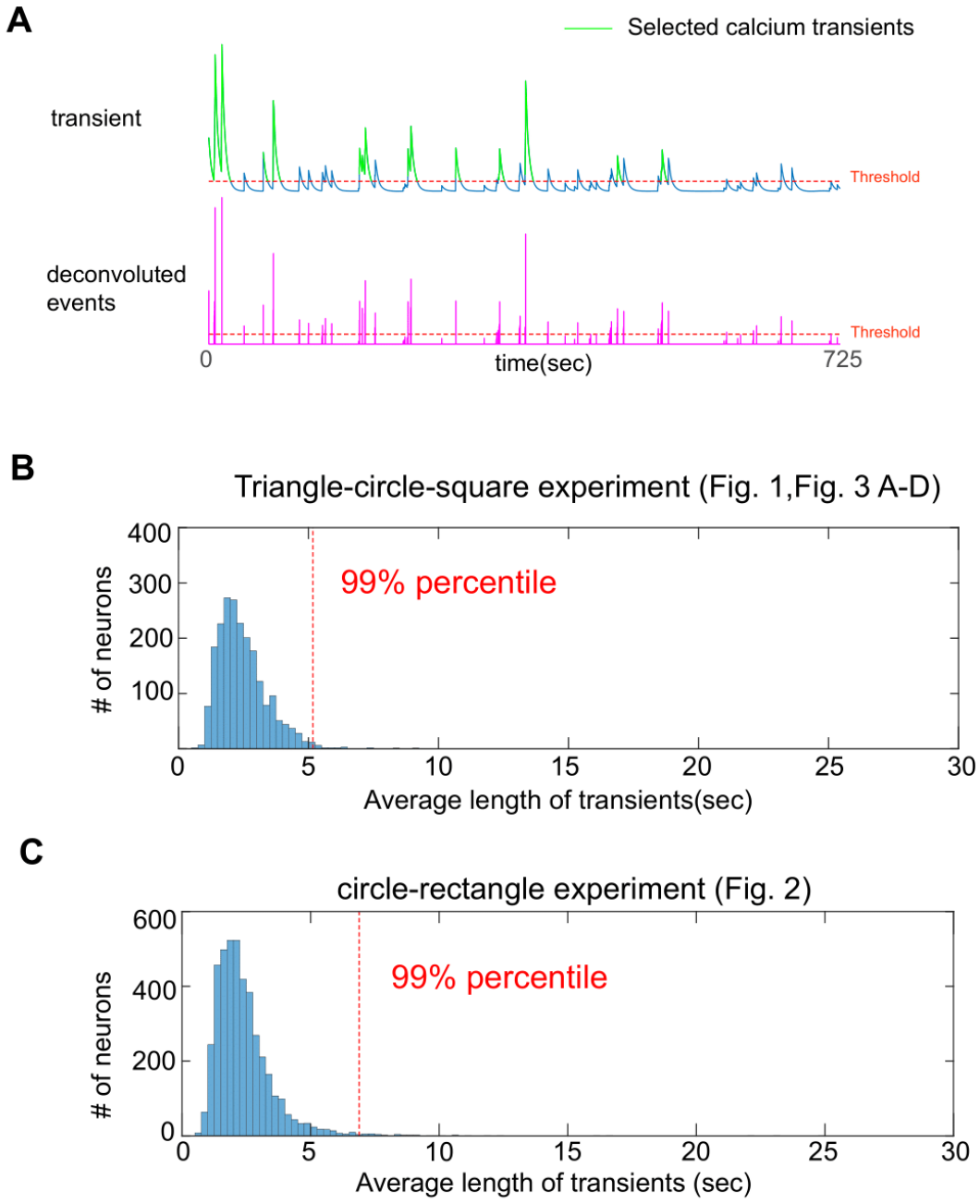

Figure 1.12. Distributions of calcium transient durations do not show apparent abnormality (A). Illustration of selected calcium transients (green). Using the aligned deconvoluted calcium event, a calcium transient duration/length is determined by including the calcium response duration to both the left and right of the event. An average transient length is calculated for each individual neuron using all transients detected in a single trial. (B). The transient length distribution of AAV-GCaMP experiment 1; the 99th percentile of transient lengths is 5.1707 sec. (C). The transient length distribution of AAV-GCaMP experiment 2; the 99th percentile of transient lengths is 6.8808 sec.

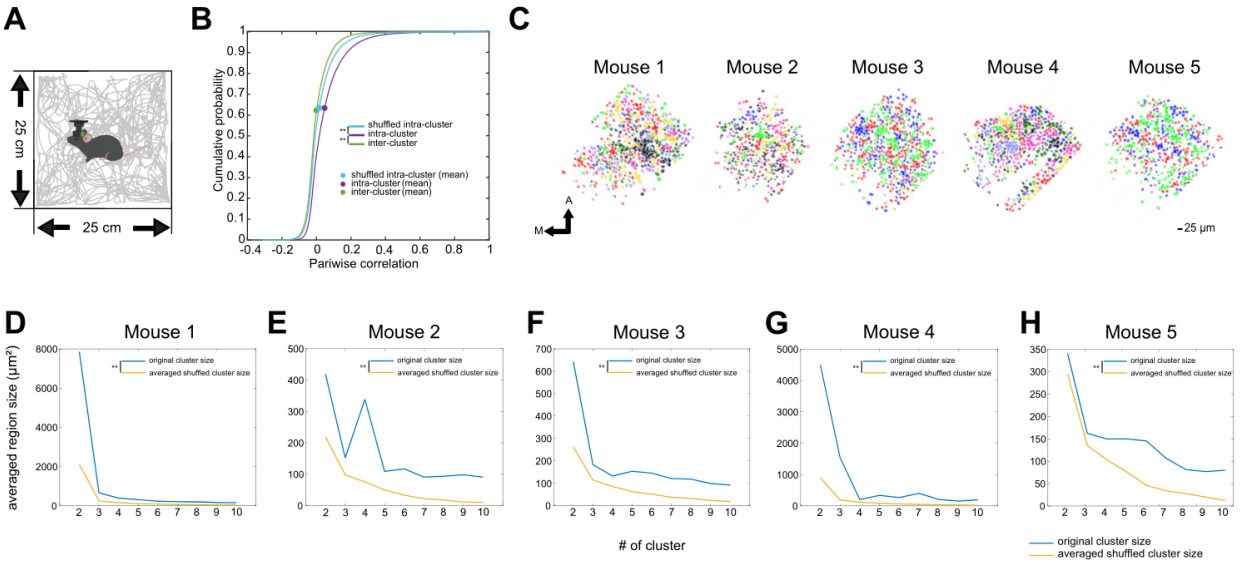

Figure 1.13. Anatomical cluster sizes in hippocampal CA1 of Camk2a-Cre; Ai163 mice (A) Experiment design. Six mice were explored in a 26cm*26cm square arena for 10 minutes. The gray line represents the locomotion trajectory of an example mouse during the experiment. (B) Comparisons of cumulative probabilities between intra- and inter- cluster pairwise temporal cross-correlation of neuronal calcium event dynamics, as well as a shuffled intra-cluster pairwise cross-correlation. The intra-cluster correlation is significantly higher than both shuffled and the inter-cluster correlation (intra-cluster, 0.0687 ± 0.0013; inter-cluster, 0.0002 ± 0.0001; shuffled intra-cluster, 0.0255 ± 0.00001; intra-cluster versus inter-cluster, p= $1.0671*10^{-60}$, intra-cluster versus shuffled intra-cluster-cluster, p= $2.2669*10^{-37}$, two sample Kolmogorov–Smirnov test, Data are presented as the mean ± SEM, N=6 mice). (C) Illustration of the anatomical clusters in hippocampal CA1 of all the five Camk2-Cre; Ai163 mouse in used, during the square arena exploration. (D-H) Comparison of anatomical patch size of original clusters, and the average patch size of 100 shuffled clusters, for each of the 5 mice used in the experiment. The patch size is calculated across each cluster number inside the selection range. Overall, for each cluster number tested, the original clusters display larger anatomical sizes than the averaged region size of shuffled clusters, for all the 5 mice used. (Mouse 1: p=0.0039, Mouse 2: p=0.0039, Mouse 3: p=0.0039, Mouse 4: p=0.0039, Mouse 5: p=0.0039, Two-sample Wilcoxon Signed Rank test, N= 9 cluster numbers). Asterisks are defined as $p \leq 0.05$ *, p< 0.01,**, p< 0.001,***.

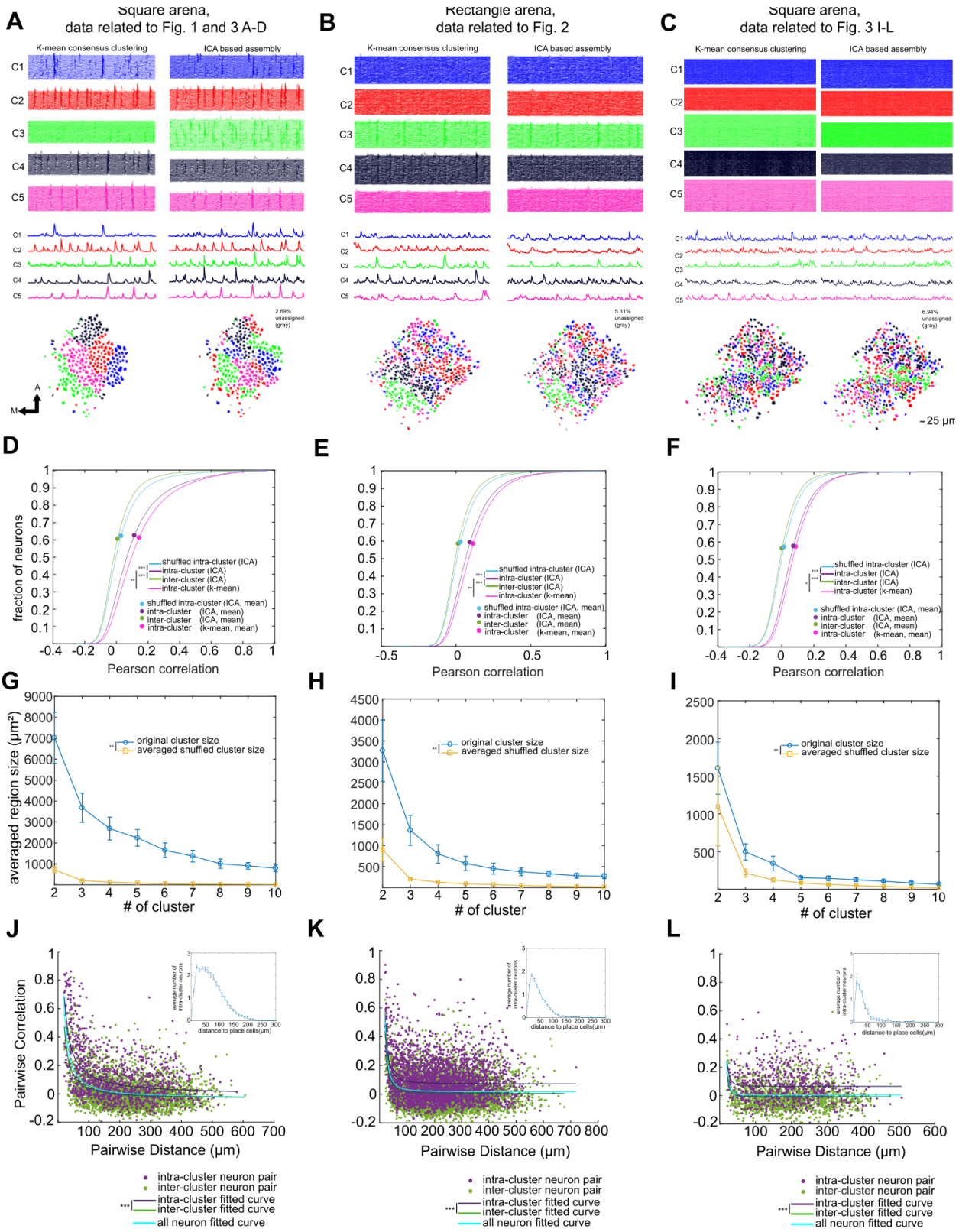
A
Square arena,
data related to Fig. 1 and 3 A-D
B
Rectangle arena,
data related to Fig. 2
C
Square arena,
data related to Fig. 3 I-L
K-mean consensus clustering
ICA based assembly
C1
C2
C3
C4
C5
2.89% unassigned (gray)
5.31% unassigned (gray)
6.94% unassigned (gray)
A
M
25 μm
D
E
F
fraction of neurons
Pearson correlation
shuffled intra-cluster (ICA)
intra-cluster (ICA)
inter-cluster (ICA)
intra-cluster (k-mean)
shuffled intra-cluster (ICA, mean)
intra-cluster (ICA, mean)
inter-cluster (ICA, mean)
intra-cluster (k-mean, mean)
G
H
I
averaged region size (μm²)
# of cluster
original cluster size
averaged shuffled cluster size
J
K
L
Pairwise Correlation
Pairwise Distance (μm)
average number of intra-cluster neurons
distance to place cells(μm)
intra-cluster neuron pair
inter-cluster neuron pair
intra-cluster fitted curve
inter-cluster fitted curve
all neuron fitted curve

Figure 1.14. ICA-based assembly detection results in comparison with k-mean-based consensus clustering (A-C) Direct comparison of the assemblies extracted by the k-mean-based consensus clustering (left), and ICA-based assembly detection using the approach described in Lopes-dos-Santos et al (2013) (right). For ICA-based assemblies, the number of assemblies is set to the same as k-mean-based assemblies. Neurons that have negative weights toward all ICA-based assemblies are excluded and labeled in gray in the anatomical footprints. It is noted that both k-mean-based and ICA-based approaches can capture the same co-activation events occurring during the trial. However, an individual k-mean assembly does not necessarily have the same set of co-activation events as an ICA-based assembly. (D-F). Comparison between intra- and inter-assembly pairwise cross-correlation of temporal calcium dynamics of neurons, as well as the shuffled intra-assembly pairwise cross-correlation for ICA-based assemblies in each experiment. For ICA-based assemblies, the intra-cluster correlation is significantly higher than both shuffled and inter-cluster correlation. K-mean based assemblies show higher intra-cluster correlation than ICA-based assemblies (**D:**: k-mean consensus intra-cluster: 0.1542 ± 0.0181; ICA intra-cluster: 0.1201 ± 0.0106; ICA shuffled intra-cluster: 0.0322 ± 0.0034; ICA inter-cluster: 0.0108 ± 0.0043. k-mean intra-cluster vs. ICA intra-cluster: p=0.0044, ICA intra-cluster vs. ICA inter-cluster: $p=3.9748*10^{-43}$, ICA intra-cluster vs. ICA shuffled intra-cluster-cluster: $p=8.1834*10^{-26}$, two sample Kolmogorov–Smirnov test, Data are presented as the mean ± SEM) (**E**: k-mean consensus intra-cluster: 0.1235 ± 0.0093; ICA intra-cluster: 0.0968 ± 0.0061; ICA shuffled intra-cluster: 0.0301 ± 0.0021; ICA inter-cluster: 0.0147 ± 0.0019. k-mean intra-cluster vs. ICA intra-cluster: p=0.0002, ICA intra-cluster vs. ICA inter-cluster: $p=4.8257*10^{-88}$, ICA intra-cluster vs. ICA shuffled intra-cluster-cluster: $p=4.4463*10^{-63}$, two sample Kolmogorov–Smirnov test, Data are presented as the mean ± SEM) (**F**: k-mean consensus intra-cluster: 0.0898 ± 0.0092; ICA intra-cluster: 0.0731 ± 0.0084; ICA shuffled intra-cluster: 0.0075 ± 0.0015; ICA inter-cluster: -0.0058 ± 0.0035. k-mean intra-cluster vs. ICA intra-cluster: p=0.0212, ICA intra-cluster vs. ICA inter-cluster: $p=1.3326*10^{-67}$, ICA intra-cluster vs. ICA shuffled intra-cluster-cluster: $p=1.5276*10^{-57}$, two sample Kolmogorov–Smirnov test, Data are presented as the mean ± SEM). (G-I) the cluster patch sizes change across different numbers of clusters for ICA-based assemblies. Blue circle: Patch size of the original anatomical clusters. Yellow square: averaged size of the 100 shuffled cluster patchs. Comparing the curves of the original anatomical cluster size and shuffled baseline across different cluster numbers, the original cluster size is higher than the shuffled at all cluster number candidates (**G**: p=0.0039, **H**: p=0.0039, **I**: p=0.0039, Wilcoxon matched -pair signed rank test, N=9 cluster numbers). (J-L) Relationship between pairwise temporal correlations and pairwise anatomical distance of neuron pairs for ICA-based assemblies. Intra- and inter-cluster data are represented in purple and green, respectively. The distributions of intra- and inter-cluster data are fitted to a first-order power function. Overall, across neuron pairs from all mice, a significant negative relationship is identified between pairwise temporal correlations and pairwise distances (Cyan line: **J**: spearman correlation=-0.2411, $p=1.3701*10^{-104}$; **K**: spearman correlation=-0.0824, $p=3.3219*10^{-25}$; **L**: spearman correlation=-0.0402, p=0.0049). Also, intra-cluster neuron pairs also exhibit overall lower pairwise distance than inter-cluster neuron pairs (**J**: Intra-cluster neuron average pairwise distance: 196.3884 ± 0.4854μm; Inter-cluster neuron average pairwise distance: 224.9410 ± 0.1379 μm; $p= 3.8966*10^{-18}$, Wilcoxon matched-pair signed rank test, Data are presented as the mean ± SEM; **K**: Intra-cluster neuron average pairwise distance: 222.7403 ± 0.3073μm; Inter-cluster neuron average pairwise distance: 232.6561 ± 0.1116 μm, $p=3.8966*10^{-18}$, Wilcoxon matched-pair signed rank test, Data are presented as the mean ± SEM; **L**: Intra-cluster neuron average pairwise distance: 193.2881 ± 0.5013μm; Inter-cluster neuron average pairwise

distance: 196.8642 ± 0.1783 µm, $p=3.8966*10^{-18}$; Wilcoxon matched-pair signed rank test, Data are presented as the mean ± SEM). The subplot at the top right illustrates the distribution of neighboring cells toward intra-cluster place cells. Asterisks are defined as $p \leq 0.05$ *, $p< 0.01$,**, $p< 0.001$,***.

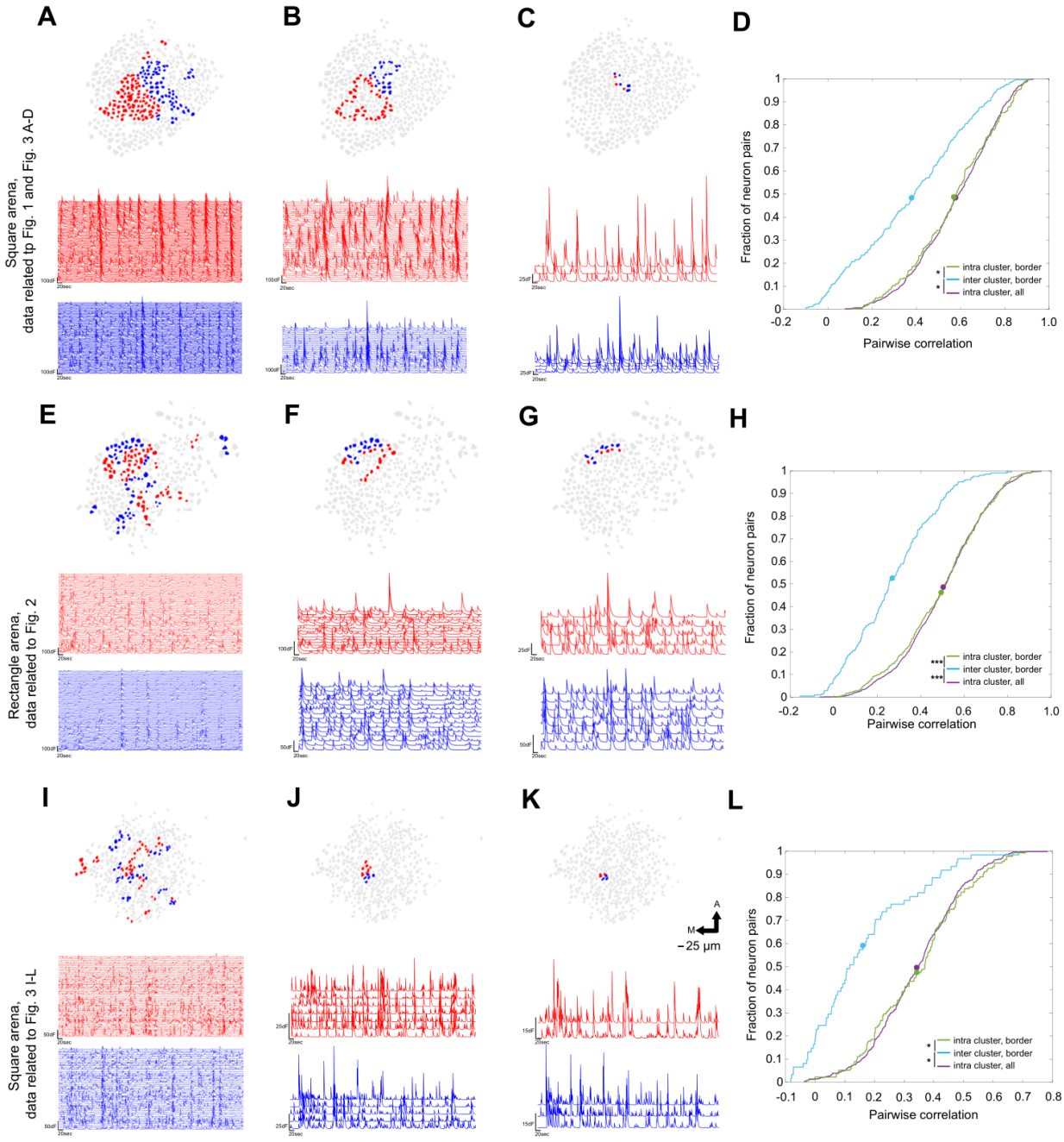

Figure 1.15. Correlation analyses of Intra-cluster, border intra-cluster, and border inter-cluster neighboring neuron pairs (A-C). Examples of intra-cluster neurons, intra-cluster border neurons, and inter-cluster border neurons of an example mouse with AAV expressing GCaMP in hippocampal CA1 in the first square arena trial in Fig. 1 and 3 A-D. Only neighboring neurons are shown and used for the correlation analysis. (D) Pairwise Pearson correlation between neighboring neuron pairs for all mice used in the trial. Overall intra-cluster neuron pairs and border intra-cluster neuron pairs do not show significant differences, but both of them exhibit higher pairwise correlation toward border inter-cluster neuron pairs (intra-cluster neighboring neuron pairs: 0.5788 ± 0.0347, border intra-cluster neighboring neuron pairs: 0.5678 ± 0.0381, border inter-cluster

neighboring neuron pairs: 0.3819 ± 0.0466; intra-cluster vs. border intra-cluster: p=0.3180, intra-cluster vs. border inter-cluster: p=0.0122, border intra-cluster vs. border inter-cluster: p=0.0123, two sample Kolmogorov–Smirnov test, Data are presented as the mean ± SEM). (E-G) Examples of intra-cluster neurons, intra-cluster border neurons, and inter-cluster border neurons of an example mouse with AAV expressing GCaMP in hippocampal CA1 in the rectangle arena trial in Fig. 2. Only neighboring neurons are shown and used for the correlation analysis. (H). Pairwise Pearson correlation between neighboring neuron pairs, for all mice in the trial. Overall intra-cluster neuron pairs and border intra-cluster neuron pairs do not show significant differences, but both of them exhibit higher pairwise correlation toward border inter-cluster neuron pairs (intra-cluster neighboring neuron pairs: 0.5045 ± 0.0127, border intra-cluster neighboring neuron pairs: 0.4844 ± 0.0177, border inter-cluster neighboring neuron pairs: 0.2600 ± 0.0278; intra-cluster vs. border intra-cluster: p=0.4333, intra-cluster vs. border inter-cluster: p= $2.0531*10^{-5}$, border intra-cluster vs. border inter-cluster: p=0.0002, two sample Kolmogorov–Smirnov test, Data are presented as the mean ± SEM) (I-K). Examples of intra-cluster neurons, intra-cluster border neurons, and inter-cluster border neurons of example Camk2a-Cre; Ai163 mice in the first square arena trial of Fig. 3. I-L. Only neighboring neurons are shown and used for the correlation analysis. (L). Pairwise Pearson correlation between neighboring neuron pairs, for all Camk2a-Cre; Ai163 mice in the trial. Overall intra-cluster neuron pairs and border intra-cluster neuron pairs do not show significant differences, but both of them exhibit higher pairwise correlation toward border inter-cluster neuron pairs (intra-cluster neighboring neuron pairs: 0.3378 ± 0.0131, border intra-cluster neighboring neuron pairs: 0.3558 ± 0.0319, border inter-cluster neighboring neuron pairs: 0.1842 ± 0.0482; intra-cluster vs. border intra-cluster: p=0.9996, intra-cluster vs. border inter-cluster: p= 0.0361, border intra-cluster vs. border inter-cluster: p=0.0364. two sample Kolmogorov–Smirnov test, Data are presented as the mean ± SEM). Asterisks are defined as $p \leq 0.05$ *, p< 0.01,**, p< 0.001,***.

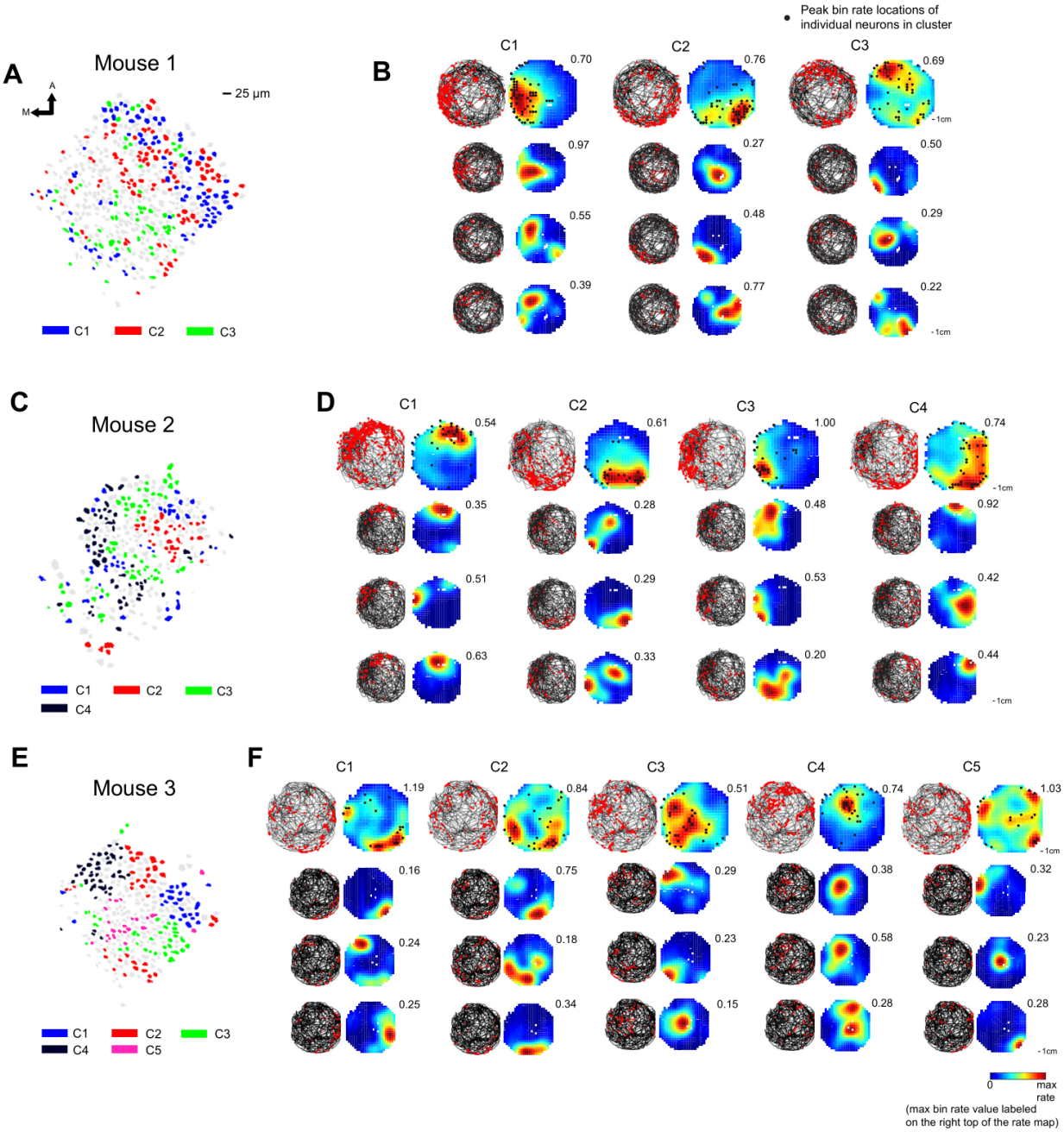
A
Mouse 1
A
M
25 μm
C1
C2
C3
B
Peak bin rate locations of individual neurons in cluster
C1
C2
C3
0.70
0.76
0.69
1cm
0.97
0.27
0.50
0.55
0.48
0.29
0.39
0.77
0.22
1cm
C
Mouse 2
C1
C2
C3
C4
D
C1
C2
C3
C4
0.54
0.61
1.00
0.74
1cm
0.35
0.28
0.48
0.92
0.51
0.29
0.53
0.42
0.63
0.33
0.20
0.44
1cm
E
Mouse 3
C1
C2
C3
C4
C5
F
C1
C2
C3
C4
C5
1.19
0.84
0.51
0.74
1.03
1cm
0.16
0.75
0.29
0.38
0.32
0.24
0.18
0.23
0.58
0.23
0.25
0.34
0.15
0.28
0.28
1cm
0
max rate
(max bin rate value labeled on the right top of the rate map)
G
Mouse 1
r=0.5010
p<0.05
Pairwise temporal correlation
Pairwise activity map correlation
H
Mouse 2
r=0.3618
p<0.05
Pairwise activity map correlation
I
Mouse 3
neuron
fit line
r=0.3306
p<0.05
Pairwise activity map correlation

Figure 1.16. Place cell ensemble rate map analysis for the circle arena data (A, C, E) Anatomical clusters in hippocampal CA1 of three representative mice imaged for calcium events while exploring the circle arena in Fig. 2. Only place cells are shown. (B, D, F) The upper portion (first row) of the panels represents ensemble activity maps of the anatomical clusters in A, C, and E. The lower portion of the panels represents activity maps of 3 representative place cells from each anatomical cluster. The number on the right top of each activity map represent the maximum bin rate in the map (G, H, I) Relationship between pairwise temporal correlation and pairwise activity map correlation for neuron pairs within the anatomical clusters for the three representative mice is shown in A, C, and E. Each of the neuron pairs is represented by a single black dot. For all three example mice, the pairwise temporal correlations have a significant positive linear relationship with the pairwise activity map correlations (mouse 1: Pearson's r = 0.5010, $p=3.5639*10^{-188}$; mouse 2: Pearson's r = 0.3618, $p=3.0705*10^{-57}$; mouse 3: Pearson's r = 0.3306, $p=1.3156*10^{-26}$)

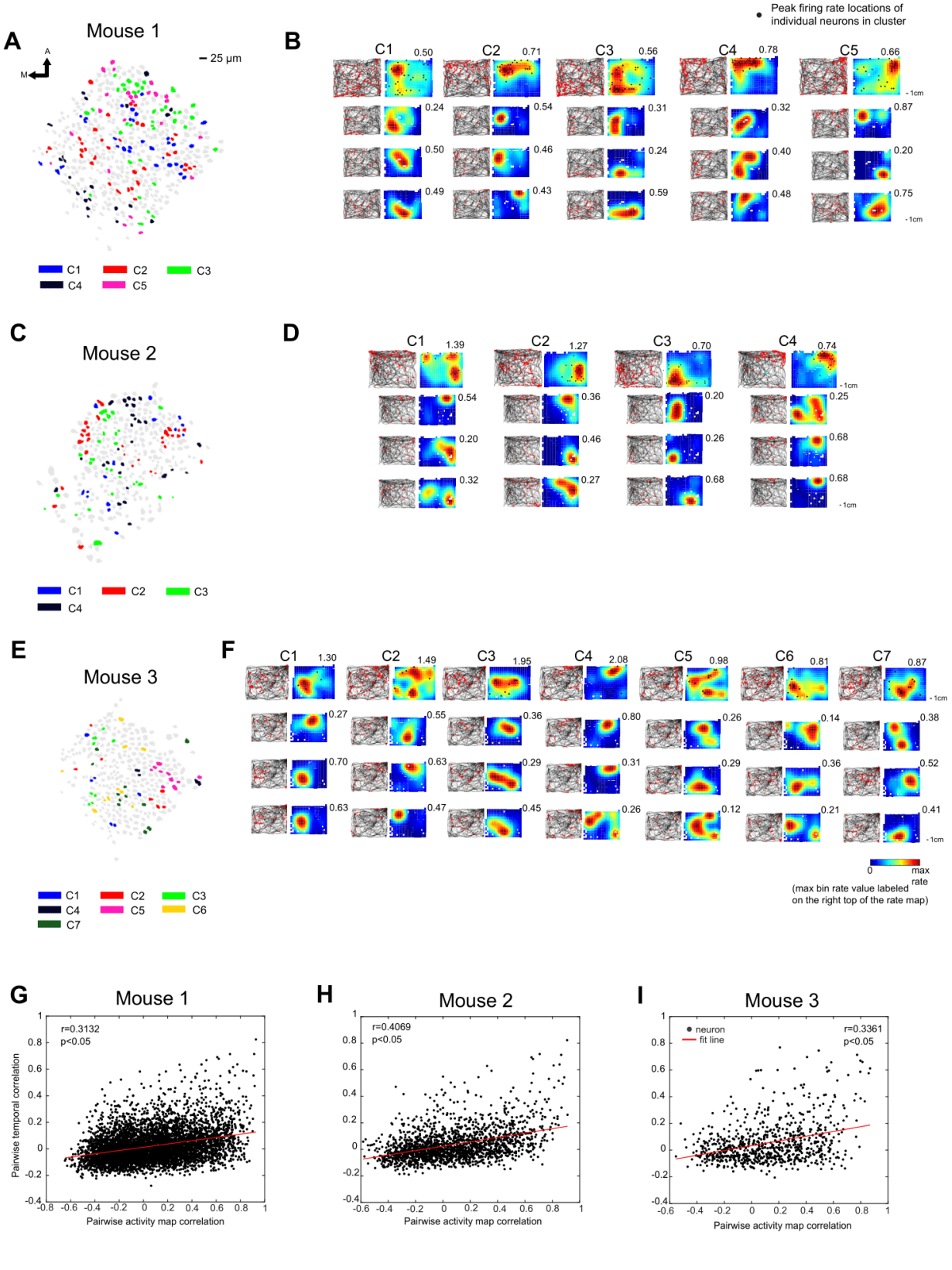
A
Mouse 1
A
M
25 μm
C1
C2
C3
C4
C5
B
Peak firing rate locations of individual neurons in cluster
C1 0.50
C2 0.71
C3 0.56
C4 0.78
C5 0.66
0.24
0.54
0.31
0.32
0.87
0.50
0.46
0.24
0.40
0.20
0.49
0.43
0.59
0.48
0.75
1cm
C
Mouse 2
C1
C2
C3
C4
D
C1 1.39
C2 1.27
C3 0.70
C4 0.74
0.54
0.36
0.20
0.25
0.20
0.46
0.26
0.68
0.32
0.27
0.68
0.68
1cm
E
Mouse 3
C1
C2
C3
C4
C5
C6
C7
F
C1 1.30
C2 1.49
C3 1.95
C4 2.08
C5 0.98
C6 0.81
C7 0.87
0.27
0.55
0.36
0.80
0.26
0.14
0.38
0.70
0.63
0.29
0.31
0.29
0.36
0.52
0.63
0.47
0.45
0.26
0.12
0.21
0.41
1cm
0
max rate
(max bin rate value labeled on the right top of the rate map)
G
Mouse 1
r=0.3132
p<0.05
Pairwise temporal correlation
Pairwise activity map correlation
H
Mouse 2
r=0.4069
p<0.05
Pairwise activity map correlation
I
Mouse 3
neuron
fit line
r=0.3361
p<0.05
Pairwise activity map correlation

Figure 1.17. Place cell ensemble rate map analysis for the rectangle arena data (A, C, E) Anatomical clusters in hippocampal CA1 of three mice imaged for calcium events while exploring the rectangle arena as shown in Supplemental Fig. 5. Only place cells are shown. (B, D, F) The upper portion of the panels represents ensemble activity maps of the anatomical clusters in A, C, and E. The lower portion of the panels represents activity maps of 3 representative place cells from each anatomical cluster. The number on the right top of each activity map represent the maximum bin rate in the map (G, H, I) Relationship between pairwise temporal correlation and pairwise activity map correlation for neuron pairs within the anatomical clusters for the three representative mice depicted in A, C, E. Each of the neuron pairs is represented by a single black dot. For all three example mice, the pairwise temporal correlations have a significant positive linear relationship with the pairwise activity map correlations (mouse 1: Pearson's $r = 0.3132$, $p=4.6473*10^{-124}$; mouse 2: Pearson's $r = 0.4069$, $p=1.4662*10^{-71}$; mouse 3: Pearson's $r = 0.3361$, $p=4.6658*10^{-22}$).

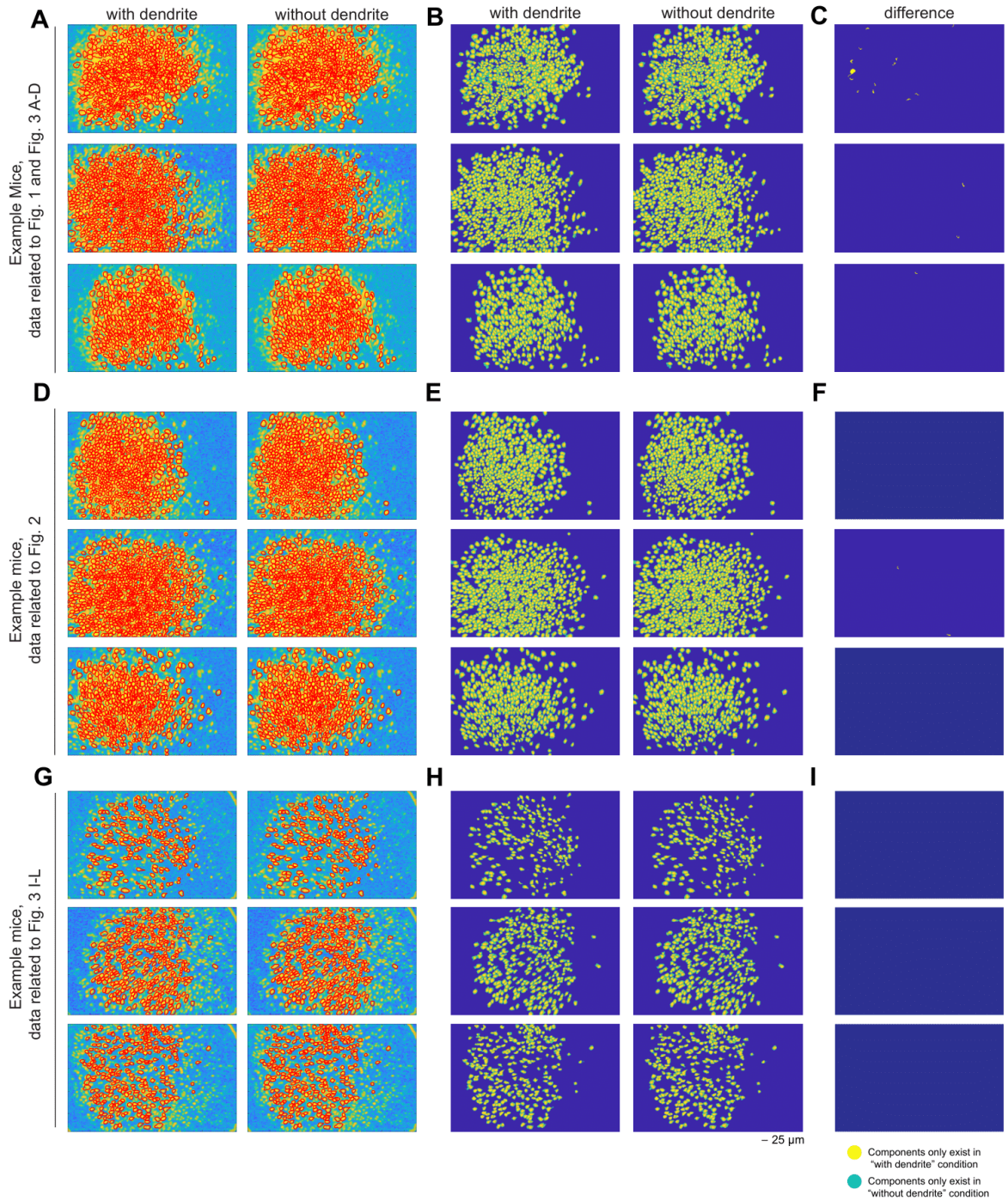

Figure 1.18. Comparison of extraction results with/without the CNMF-E "with dendrite" feature (A, D, G) CNMF-E revealed neuron footprints in hippocampal CA1 of example mice. For the "with_dendrite" group, CNMF-E's "with_dendrite" feature was turned on during extraction, which does not restrict the shape of detected components. For the "without_dendrite" group, CNMF-E's "with_dendrite" feature was turned off, in which the algorithm only preserves components with the shape of neuron soma. (B, E, H) CNMF-E extracted neuron footprints in hippocampal CA1 of the example mice shown in A, D, G. (C, F, I) Differences between extracted neuron footprints of "with dendrite" and "without dendrite" options.

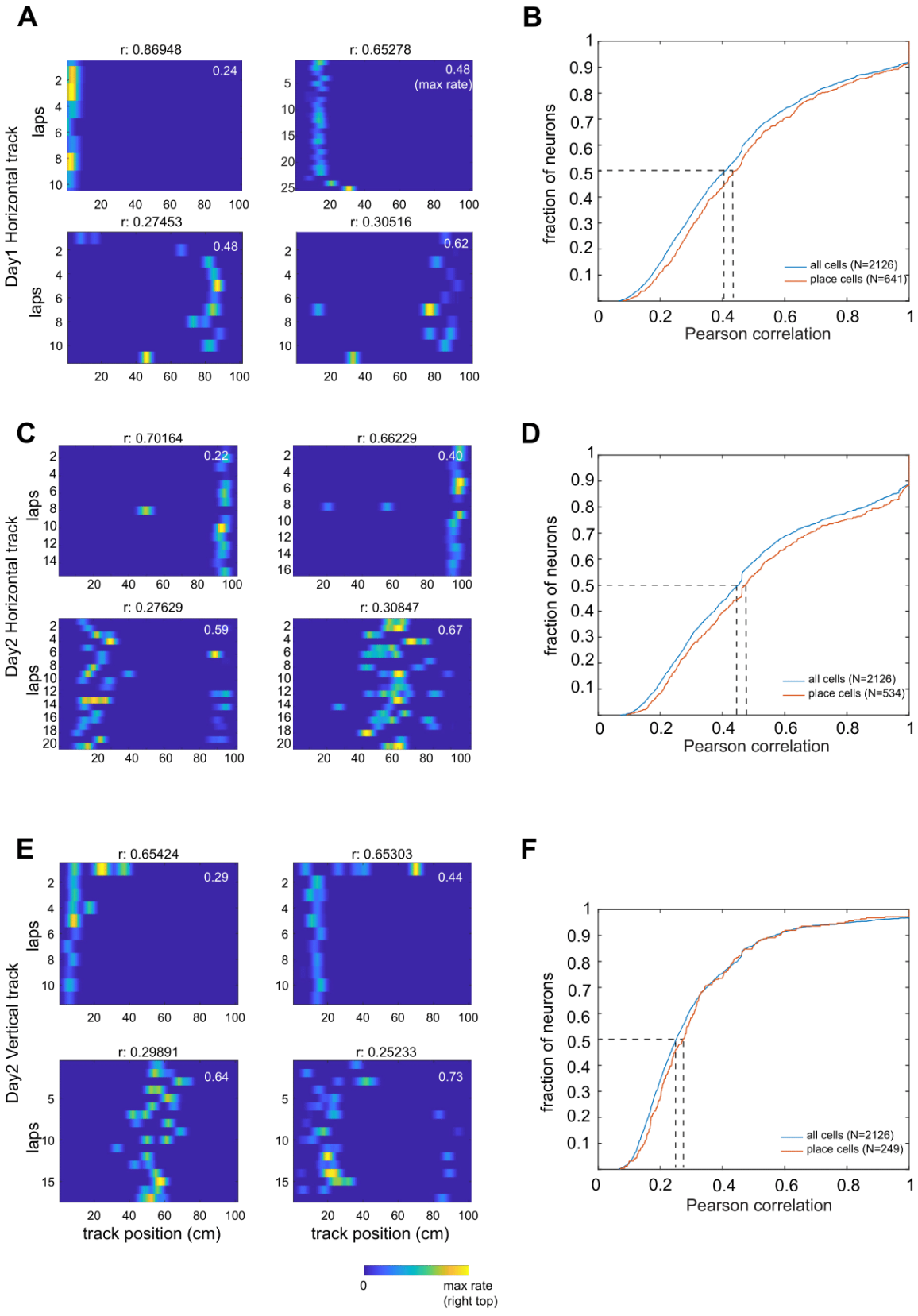
A
r: 0.86948
0.24
r: 0.65278
0.48
(max rate)
r: 0.27453
0.48
r: 0.30516
0.62
Day1 Horizontal track
laps
B
fraction of neurons
Pearson correlation
all cells (N=2126)
place cells (N=641)
C
r: 0.70164
0.22
r: 0.66229
0.40
r: 0.27629
0.59
r: 0.30847
0.67
Day2 Horizontal track
D
all cells (N=2126)
place cells (N=534)
E
r: 0.65424
0.29
r: 0.65303
0.44
r: 0.29891
0.64
r: 0.25233
0.73
Day2 Vertical track
track position (cm)
0
max rate
(right top)
F
all cells (N=2126)
place cells (N=249)

Figure 1.19. Lap-by-lap stability of detected CA1 neurons in linear track experiments (A, C, E). Lap-by-lap activity map plots of four example neurons in three different trials (Day1 Horizontal track, Day2 Horizontal track, Day2 Vertical track). The lap activity map is calculated by using the firing rate in each 10-mm spatial bin. Maximum firing rate is labeled at right top corner of activity maps (B, D, F). Cumulative distributions of lap-by-lap correlations of all cells and place cells for all 3 trials (Day1 Horizontal track, 2126 cells and 641 place cells from 6 mice; Day2 Horizontal track, 2126 cells and 534 place cells from 6 mice; Day2 vertical track, 2126 cells and 249 place cells from 6 mice). Place cell populations exhibit slightly higher, but not significant, between-lap correlation distributions compared with all neurons (Day1 Horizontal track, all cells median correlation: 0.4078, place cell median correlation: 0.4383, p=0.6225; Day2 Horizontal track, all cells: 0.4500, place cell: 0.4731, p=0.8456; Day2 Vertical track, all cells: 0.2523, place cell: 0.2724, p=0.8656. two sample Kolmogorov–Smirnov test). Asterisks are defined as $p \leq 0.05$ *, p< 0.01,**, p< 0.001,***.

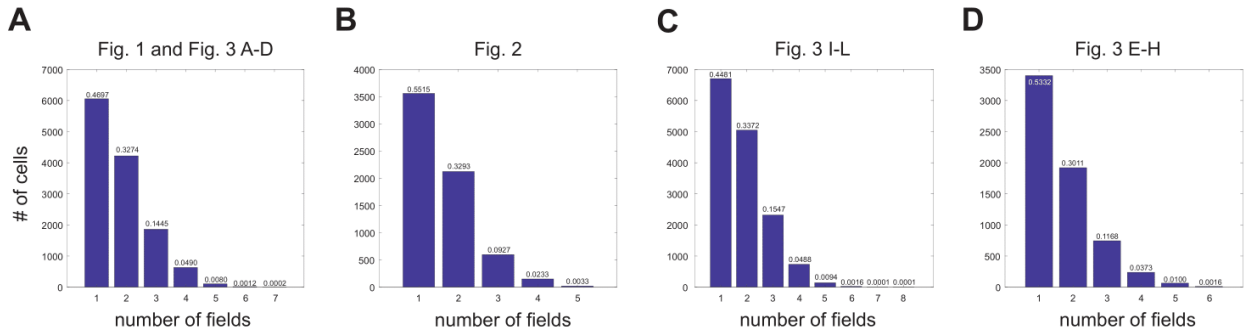

Figure 1.20. Numbers of firing fields of CA1 neurons across mice in different experiments (A-D) Distribution of firing field numbers of individual neurons in the 4 experiments (shown in the corresponding figure panels). The fractions of neurons with specific numbers of fields are labeled on the top of each bar. Overall, a large number of neurons exhibit only one firing field during the experiments (46.97% for 2149 cells from 6 mice across 6 trials, the Figure 1 and Figure 3 A-D related data; 55.15% for 4314 cells from 12 mice across 2 trials, the Figure 1.4 related data; 44.81% for 2504 cells from 6 mice across 6 trials, Figure 3 I-L related data; 53.32% for 2126 cells from 6 mice across 3 trials, Figure 3 E-H related data).

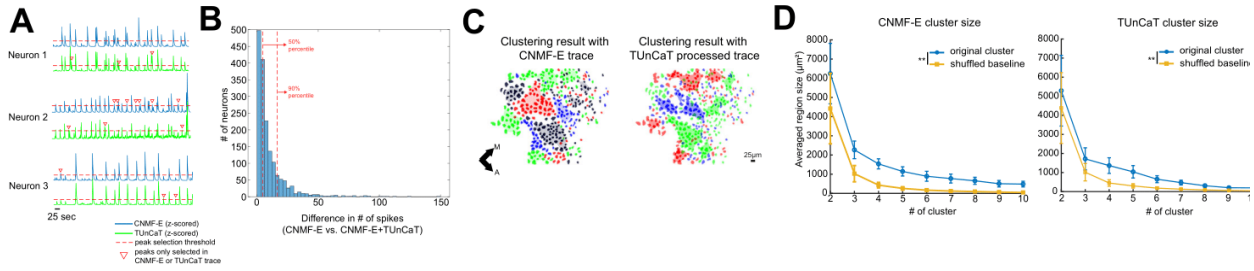

Figure 1.21. The application of Temporal Unmixing of Calcium Traces (TUnCaT) algorithm confirms anatomical clusters (A) CNMF-E extracted calcium traces (blue) and TUnCaT processed calcium traces (green) of the three example neurons. Activity peaks that only appear in CNMF-E or TUnCaT traces are labeled with red triangle. (B) The distribution of differences in the total number of above-threshold peaks between original CNMF-E trace and TUnCaT processed trace, for all individual neurons across the 6 mice. (C) Left: Cluster detection result of an example mice using original CNMF-E calcium trace Right: Cluster detection result of the same mice using TUnCaT processed calcium trace. (D) The plots of average sizes of anatomical clusters across different cluster numbers, for original CNMF-E's clustering result (left) and clusters generated with TUnCaT processed calcium traces (right). Blue circle: averaged size of the original clusters. Yellow square: average size of the corresponding shuffled clusters, which serves as a control. Both CNMF-E generated clusters and TUnCaT generated clusters significantly exceeds the randomized controls. (Averaged original cluster size vs. averaged shuffled controls, across all cluster numbers: CNMF-E: p=0.0039, TUnCaT: p=0.0039, Wilcoxon matched-pairs signed rank tests, N=9 cluster numbers). Asterisks are defined as $p \leq 0.05$ *, $p < 0.01$,**, $p < 0.001$,***.

References

Alexander, A. S., & Nitz, D. A. (2015). Retrosplenial cortex maps the conjunction of internal and external spaces. *Nature Neuroscience*, *18*(8), 1143-1151. https://doi.org/10.1038/nn.4058

Bao, Y., Redington, E., Agarwal, A., & Gong, Y. (2022). Decontaminate Traces From Fluorescence Calcium Imaging Videos Using Targeted Non-negative Matrix Factorization [Methods]. *Frontiers in Neuroscience*, *15*. https://www.frontiersin.org/articles/10.3389/fnins.2021.797421

Bittner, K. C., Milstein, A. D., Grienberger, C., Romani, S., & Magee, J. C. (2017). Behavioral time scale synaptic plasticity underlies CA1 place fields. *Science*, *357*(6355), 1033-1036. https://doi.org/10.1126/science.aan3846

Brown, E. N., Frank, L. M., Tang, D., Quirk, M. C., & Wilson, M. A. (1998). A Statistical Paradigm for Neural Spike Train Decoding Applied to Position Prediction from Ensemble Firing Patterns of Rat Hippocampal Place Cells. *The Journal of Neuroscience*, *18*(18), 7411. https://doi.org/10.1523/JNEUROSCI.18-18-07411.1998

Brunet, J.-P., Tamayo, P., Golub, T. R., & Mesirov, J. P. (2004). Metagenes and molecular pattern discovery using matrix factorization. *Proceedings of the National Academy of Sciences*, *101*(12), 4164. https://doi.org/10.1073/pnas.0308531101

Daigle, T. L., Madisen, L., Hage, T. A., Valley, M. T., Knoblich, U., Larsen, R. S., Takeno, M. M., Huang, L., Gu, H., Larsen, R., Mills, M., Bosma-Moody, A., Siverts, L. A., Walker, M., Graybuck, L. T., Yao, Z., Fong, O., Nguyen, T. N., Garren, E., . . . Zeng, H. (2018). A Suite of Transgenic Driver and Reporter Mouse Lines with Enhanced Brain-Cell-Type Targeting and Functionality. *Cell*, *174*(2), 465-480.e422. https://doi.org/https://doi.org/10.1016/j.cell.2018.06.035

Dolleman-van der Weel, M. J., Griffin, A. L., Ito, H. T., Shapiro, M. L., Witter, M. P., Vertes, R. P., & Allen, T. A. (2019). The nucleus reuniens of the thalamus sits at the nexus of a hippocampus and medial prefrontal cortex circuit enabling memory and behavior. *Learning & Memory*, *26*, 191-205. https://doi.org/10.1101/lm.048389.118

Dombeck, D. A., Harvey, C. D., Tian, L., Looger, L. L., & Tank, D. W. (2010). Functional imaging of hippocampal place cells at cellular resolution during virtual navigation. *Nature Neuroscience*, *13*(11), 1433-1440. https://doi.org/10.1038/nn.2648

Eichenbaum, H., Wiener, S. I., Shapiro, M. L., & Cohen, N. J. (1989). The organization of spatial coding in the hippocampus: a study of neural ensemble activity. *The Journal of Neuroscience*, *9*(8), 2764. https://doi.org/10.1523/JNEUROSCI.09-08-02764.1989

English, D. F., McKenzie, S., Evans, T., Kim, K., Yoon, E., & Buzsáki, G. (2017). Pyramidal Cell-Interneuron Circuit Architecture and Dynamics in Hippocampal Networks. *Neuron*, *96*(2), 505-520.e507. https://doi.org/https://doi.org/10.1016/j.neuron.2017.09.033

Ester, M., Kriegel, H.-P., Sander, J., & Xu, X. (1996). *A density-based algorithm for discovering clusters in large spatial databases with noise* Proceedings of the Second International Conference on Knowledge Discovery and Data Mining, Portland, Oregon.

Fenton, A. A., Lytton, W. W., Barry, J. M., Lenck-Santini, P.-P., Zinyuk, L. E., Kubík, Š., Bureš, J., Poucet, B., Muller, R. U., & Olypher, A. V. (2010). Attention-Like Modulation of Hippocampus Place Cell Discharge. *The Journal of Neuroscience*, *30*(13), 4613. https://doi.org/10.1523/JNEUROSCI.5576-09.2010

Friedrich, J., Zhou, P., & Paninski, L. (2017). Fast online deconvolution of calcium imaging data. *PLOS Computational Biology*, *13*(3), e1005423. https://doi.org/10.1371/journal.pcbi.1005423

Geiller, T., Sadeh, S., Rolotti, S. V., Blockus, H., Vancura, B., Negrean, A., Murray, A. J., Rózsa, B., Polleux, F., Clopath, C., & Losonczy, A. (2022). Local circuit amplification of spatial selectivity in the hippocampus. *Nature*, *601*(7891), 105-109. https://doi.org/10.1038/s41586-021-04169-9

Giocomo, L. M. (2016). Environmental boundaries as a mechanism for correcting and anchoring spatial maps [https://doi.org/10.1113/JP270624]. *The Journal of Physiology*, *594*(22), 6501-6511. https://doi.org/https://doi.org/10.1113/JP270624

Grieves, R. M., Wood, E. R., & Dudchenko, P. A. (2016). Place cells on a maze encode routes rather than destinations. *eLife*, *5*, e15986. https://doi.org/10.7554/eLife.15986

Guzman, S. J., Schlögl, A., Frotscher, M., & Jonas, P. (2016). Synaptic mechanisms of pattern completion in the hippocampal CA3 network. *Science*, *353*(6304), 1117-1123. https://doi.org/10.1126/science.aaf1836

Hampson, R. E., Simeral, J. D., & Deadwyler, S. A. (1999). Distribution of spatial and nonspatial information in dorsal hippocampus. *Nature*, *402*(6762), 610-614. https://doi.org/10.1038/45154

Hubel, D. H., & Wiesel, T. N. (1962). Receptive fields, binocular interaction and functional architecture in the cat's visual cortex [https://doi.org/10.1113/jphysiol.1962.sp006837]. *The Journal of Physiology*, *160*(1), 106-154. https://doi.org/https://doi.org/10.1113/jphysiol.1962.sp006837

Ito, H. T., Moser, E. I., & Moser, M.-B. (2018). Supramammillary Nucleus Modulates Spike-Time Coordination in the Prefrontal-Thalamo-Hippocampal Circuit during Navigation. *Neuron*, *99*(3), 576-587.e575. https://doi.org/https://doi.org/10.1016/j.neuron.2018.07.021

Krupic, J., Bauza, M., Burton, S., & O'Keefe, J. (2018). Local transformations of the hippocampal cognitive map. *Science*, *359*(6380), 1143-1146. https://doi.org/10.1126/science.aao4960

Lopes-dos-Santos, V., Ribeiro, S., & Tort, A. B. L. (2013). Detecting cell assemblies in large neuronal populations. *Journal of Neuroscience Methods*, *220*(2), 149-166. https://doi.org/https://doi.org/10.1016/j.jneumeth.2013.04.010

Markus, E. J., Barnes, C. A., McNaughton, B. L., Gladden, V. L., & Skaggs, W. E. (1994). Spatial information content and reliability of hippocampal CA1 neurons: Effects of visual input [https://doi.org/10.1002/hipo.450040404]. *Hippocampus*, *4*(4), 410-421. https://doi.org/https://doi.org/10.1002/hipo.450040404

Markus, E. J., Qin, Y. L., Leonard, B., Skaggs, W. E., McNaughton, B. L., & Barnes, C. A. (1995). Interactions between location and task affect the spatial and directional firing of hippocampal neurons. *The Journal of Neuroscience*, *15*(11), 7079. https://doi.org/10.1523/JNEUROSCI.15-11-07079.1995

McNaughton, B., & Morris, R. (1987). Hippocampal synaptic enhancement and information storage within a distributed memory system. *Trends in Neurosciences*, *10*, 408-415.

Modi, M. N., Dhawale, A. K., & Bhalla, U. S. (2014). CA1 cell activity sequences emerge after reorganization of network correlation structure during associative learning. *eLife*, *3*, e01982. https://doi.org/10.7554/eLife.01982

Mountcastle, V. B. (2003). Introduction. *Cerebral Cortex*, *13*(1), 2-4. https://doi.org/10.1093/cercor/13.1.2

Muller, R. U., Kubie, J. L., & Ranck, J. B. (1987). Spatial firing patterns of hippocampal complex-spike cells in a fixed environment. *The Journal of Neuroscience*, *7*(7), 1935. https://doi.org/10.1523/JNEUROSCI.07-07-01935.1987

Nitz, D., & McNaughton, B. (2004). Differential Modulation of CA1 and Dentate Gyrus Interneurons During Exploration of Novel Environments. *Journal of neurophysiology*, *91*(2), 863-872. https://doi.org/10.1152/jn.00614.2003

Nitz, D. A. (2006). Tracking Route Progression in the Posterior Parietal Cortex. *Neuron*, *49*(5), 747-756. https://doi.org/https://doi.org/10.1016/j.neuron.2006.01.037

O'Keefe, J., & Burgess, N. (1996). Geometric determinants of the place fields of hippocampal neurons. *Nature*, *381*(6581), 425-428. https://doi.org/10.1038/381425a0

O'Keefe, J., & Dostrovsky, J. (1971). The hippocampus as a spatial map. Preliminary evidence from unit activity in the freely-moving rat. *Brain Research*, *34*(1), 171-175. https://doi.org/https://doi.org/10.1016/0006-8993(71)90358-1

O'Keefe, J., & Recce, M. L. (1993). Phase relationship between hippocampal place units and the EEG theta rhythm [https://doi.org/10.1002/hipo.450030307]. *Hippocampus*, *3*(3), 317-330. https://doi.org/https://doi.org/10.1002/hipo.450030307

Pfeiffer, B. E., & Foster, D. J. (2013). Hippocampal place-cell sequences depict future paths to remembered goals. *Nature*, *497*(7447), 74-79. https://doi.org/10.1038/nature12112

Pnevmatikakis, E. A., & Giovannucci, A. (2017). NoRMCorre: An online algorithm for piecewise rigid motion correction of calcium imaging data. *Journal of Neuroscience Methods*, *291*, 83-94. https://doi.org/https://doi.org/10.1016/j.jneumeth.2017.07.031

Redish, A. D., Battaglia, F. P., Chawla, M. K., Ekstrom, A. D., Gerrard, J. L., Lipa, P., Rosenzweig, E. S., Worley, P. F., Guzowski, J. F., McNaughton, B. L., & Barnes, C. A. (2001). Independence of Firing Correlates of Anatomically Proximate Hippocampal Pyramidal Cells. *The Journal of Neuroscience*, *21*(5), RC134. https://doi.org/10.1523/JNEUROSCI.21-05-j0004.2001

Skaggs, W. E., & McNaughton, B. L. (1996). Replay of Neuronal Firing Sequences in Rat Hippocampus During Sleep Following Spatial Experience. *Science*, *271*(5257), 1870-1873. https://doi.org/10.1126/science.271.5257.1870

Skaggs, W. E., McNaughton, B. L., Wilson, M. A., & Barnes, C. A. (1996). Theta phase precession in hippocampal neuronal populations and the compression of temporal sequences [https://doi.org/10.1002/(SICI)1098-1063(1996)6:2<149::AID-HIPO6>3.0.CO;2-K]. *Hippocampus*, *6*(2), 149-172. https://doi.org/https://doi.org/10.1002/(SICI)1098-1063(1996)6:2<149::AID-HIPO6>3.0.CO;2-K

Sun, Y., Jin, S., Lin, X., Chen, L., Qiao, X., Jiang, L., Zhou, P., Johnston, K. G., Golshani, P., Nie, Q., Holmes, T. C., Nitz, D. A., & Xu, X. (2019). CA1-projecting subiculum neurons facilitate object–place learning. *Nature Neuroscience*, *22*(11), 1857-1870. https://doi.org/10.1038/s41593-019-0496-y

Treves, A., & Rolls, E. T. (1994). Computational analysis of the role of the hippocampus in memory [https://doi.org/10.1002/hipo.450040319]. *Hippocampus*, *4*(3), 374-391. https://doi.org/https://doi.org/10.1002/hipo.450040319

Villette, V., Malvache, A., Tressard, T., Dupuy, N., & Cossart, R. (2015). Internally Recurring Hippocampal Sequences as a Population Template of Spatiotemporal Information. *Neuron*, *88*(2), 357-366. https://doi.org/https://doi.org/10.1016/j.neuron.2015.09.052

Wilent, W. B., & Nitz, D. A. (2007). Discrete Place Fields of Hippocampal Formation Interneurons. *Journal of neurophysiology*, *97*(6), 4152-4161. https://doi.org/10.1152/jn.01200.2006

Wilson, M. A., & McNaughton, B. L. (1993). Dynamics of the Hippocampal Ensemble Code for Space. *Science*, *261*(5124), 1055-1058. https://doi.org/10.1126/science.8351520

Wilson, M. A., & McNaughton, B. L. (1994). Reactivation of Hippocampal Ensemble Memories During Sleep. *Science*, *265*(5172), 676-679. https://doi.org/10.1126/science.8036517

Witter, M. P., Doan, T. P., Jacobsen, B., Nilssen, E. S., & Ohara, S. (2017). Architecture of the Entorhinal Cortex A Review of Entorhinal Anatomy in Rodents with Some Comparative Notes [Review]. *Frontiers in Systems Neuroscience*, *11*. https://www.frontiersin.org/articles/10.3389/fnsys.2017.00046

Wood, E. R., Dudchenko, P. A., Robitsek, R. J., & Eichenbaum, H. (2000). Hippocampal Neurons Encode Information about Different Types of Memory Episodes Occurring in the Same Location. *Neuron*, *27*(3), 623-633. https://doi.org/https://doi.org/10.1016/S0896-6273(00)00071-4

Wu, J., Liu, H., Xiong, H., Cao, J., & Chen, J. (2015). K-Means-Based Consensus Clustering: A Unified View. *IEEE Transactions on Knowledge and Data Engineering*, *27*(1), 155-169. https://doi.org/10.1109/TKDE.2014.2316512

Zhang, S., Schönfeld, F., Wiskott, L., & Manahan-Vaughan, D. (2014). Spatial representations of place cells in darkness are supported by path integration and border information [Original Research]. *Frontiers in Behavioral Neuroscience*, *8*. https://www.frontiersin.org/article/10.3389/fnbeh.2014.00222

Zhou, P., Resendez, S. L., Rodriguez-Romaguera, J., Jimenez, J. C., Neufeld, S. Q., Giovannucci, A., Friedrich, J., Pnevmatikakis, E. A., Stuber, G. D., Hen, R., Kheirbek, M. A., Sabatini, B. L., Kass, R. E., & Paninski, L. (2018). Efficient and accurate extraction of in vivo calcium signals from microendoscopic video data. *eLife*, *7*, e28728. https://doi.org/10.7554/eLife.28728

Chapter 2: Spatial coding defects of hippocampal neural ensemble activities in the 3xTg-AD mouse model

Abstract

Alzheimer's disease (AD) causes progressive deficits in memory and cognitive function and has emerged as a major health and socio-economic concern in the US and worldwide. Despite intense interest in understanding neural and molecular mechanisms underlying AD, we still lack effective therapeutic treatments for this disorder. Here we examine large scale hippocampal neural ensemble activities imaged at single cell resolution in a triple-transgenic Alzheimer's disease mouse model (3xTg-AD) that presents both amyloid plaque and neurofibrillary pathological features. To measure spatial coding in hippocampal neural ensembles in the AD model mice in vivo, we performed GCaMP6-based calcium imaging using head-mounted, miniature fluorescent microscopes ("miniscopes") on freely moving animals. We compared hippocampal CA1 excitatory neural ensemble activity during open-field exploration, and track-based route-running behaviors in age-matched AD and control mice at young (6-7 months old) and old (18-22 months old) animals. We find locomotion significantly modulates the amplitude of hippocampal neural ensemble activities in 3xTg-AD mice during open field ambulatory movements. In open field exploration, while age decreases overall excitatory neural ensemble activities in mouse CA1, the AD genotype exhibits higher circuit excitability relative to wild type control at either the young or old age, indicating that neuronal hyperexcitability is a disease feature. In both open field and linear track traverse, 3xTg-AD mice display lower information score compared to Non-Tg mice, which indicate an impaired spatial representation among the CA1 pyramidal neuron populations under AD condition. In summary, our data provides strong evidence that defects in the neuronal population activities are associated with the development of AD pathology and AD-related memory behavioral deficits.

Introduction

Alzheimer's disease (AD) is an incurable age-related progressive neurodegenerative disorder. Individuals diagnosed with AD undergo a progressive loss of memory, cognition, language skills and personality traits ("2020 Alzheimer's disease facts and figures," 2020; Weller & Budson, 2018). Recent imaging studies from clinical and animal models imply that neuronal dysfunction and functional disruption of neuronal circuits in the brain strongly contribute to memory deficits in AD cases (Busche & Konnerth, 2016; Frere & Slutsky, 2018). As the number of AD cases steadily increase each year and current treatments are only palliative, further understanding of AD-related neural mechanisms is critically required for the development of meaningful new treatment strategies for improving memory and prolonging healthy cognitive function.

One of the major brain areas affected in AD patients is the hippocampal formation. This brain region and its connections with several cortical areas play essential roles in spatial cognition and episodic memory processes (Allison et al., 2016; Coughlan et al., 2018; Venneri et al., 2019). Studies have found that AD lead to impaired circuit function within the hippocampus and along the Entorhinal – hippocampal pathway (Grieco et al., 2023). For example, the remapping ability of hippocampal CA1 place cells and medial entorhinal cortex (MEC) grid cells are reported to be lost under latest stage AD, together with the loss of fast gamma coupling between MEC and HPC (Heechul Jun et al., 2020). At the same time, researches in humans and animal models show that the CA1 projection to the subiculum (SUB) area, the major output of tri-synaptic circuit, is significantly affected in AD (Busche et al., 2012; Lerdkrai et al., 2018). Inside CA1, alterations in excitatory/inhibitory neuronal activity balance have been found together with the progression of AD, Specifically, regional hyper-activity has been described in the vicinity of amyloid plaque

formation (Busche et al., 2012), followed by hypoactivity at late stage of the disease (Grieco et al., 2023), which could indicate dysfunctional circuit changes observed in AD cases (Busche et al., 2012).

Several AD animal models have been developed to help examine the pathological effects of Alzheimer's disease on neural circuits. The 3xTg-AD mouse model contains three mutations in homologous mouse genes associated with human familial Alzheimer's disease (APP Swedish, MAPT P301L, and PSEN1 M146V), and displays age-dependent plaque and tangle pathology. Extracellular amyloid beta (Aβ) deposits appear by 6 months in the brain and become progressively more extensive by 12 months. Although tau pathology is not observed at six months, aggregates of conformationally-altered and hyperphosphorylated tau are detected in the hippocampus by 12-15 months (Billings et al., 2005; Oddo et al., 2003). The 3xTg-AD line has been a very reliable AD model that reveals hippocampal spatial memory impairments at relatively earlier ages, even preceding plaques, and tangles formation (Baglietto-Vargas et al., 2018; Oddo et al., 2003; Stimmell et al., 2019).

Here, we used *in vivo* GCaMP6-based calcium imaging with head-mounted, miniature fluorescent microscopes ("miniscopes") on freely moving animals (Cai et al., 2016; Chen et al., 2013; Ziv et al., 2013) to study CA1 neural circuit ensemble coding associated with AD-related memory impairments in a triple-transgenic Alzheimer's disease mouse model (3xTg-AD). Head-mounted miniscope imaging enables us to examine hundreds of brain cells in action at single cell resolution, as the animal explores freely in environments. We draw on a strong premise from the literature and our previous studies that memory-based behaviors rely on neural circuitry that are altered in aging and AD (Busche & Konnerth, 2016; Canter et al., 2016; Frere & Slutsky, 2018; Grieco et al., 2023; Heechul Jun et al., 2020). Using large scale miniscope imaging of calcium

level changes at single cell resolution, we studied spatial exploration-related neural activation of hippocampal CA1 neuronal populations in freely behaving 3xTg-AD and wild type controls at young (~7 months old) and old (~22 months old) ages and determined spatial coding defects in hippocampal neural ensembles in the 3xTg-AD mouse model. The results provide strong evidence that defects in hippocampal circuit ensemble activities are associated with AD-related memory behavioral deficits.

This work is co-first authored by Xiaoxiao Lin and Lujia Chen, and both authors have permitted the incorporation of the whole article into this thesis. Dr. David Baglietto-Vargas provided significant contributions to this work in terms of providing the 3xTg AD model mouse, participating in the experiment design, and writing the manuscript.

Materials and Methods

Animals

All experiments were conducted according to the National Institutes of Health guidelines for animal care and use and were approved by the Institutional Animal Care and Use Committee and the Institutional Biosafety Committee of the University of California, Irvine. Female non-transgenic (Non-Tg) and 3xTg-AD mice at 3.6-6.5 and 18.5-21 months of age were used in this study. Our 3xTg-AD mice were provided by the La Ferla's lab and the MODEL-AD UCI center, The generation of the 3xTg-AD mice has been described previously (Belfiore et al., 2019; Oddo et al., 2003). Briefly, the 3xTg-AD model has been generated by co-microinjected two independent transgenes encoding human APPswe and the human TauP301L (both under the control of the mouse Thy1.2 regulatory element) into single-cell embryos harvested from homozygous mutant PS1M146V Knockin (PSI-KI) mice. We used the F1 mice from the cross of 129X1/SvJ (JAX reference 000691) with C57BL6 (JAX reference 000664) as non-transgenic

controls. The mice had access to food and water in their home cages with lights maintained on a 12 h light/dark cycle.

All the experimental protocols were approved by the IACUC of the University of California, Irvine and carried out in accordance with the Guide for the Care and Use of Laboratory Animals of the US National Institutes of Health.

Viral injections

3xTg-AD mice were anaesthetized under 2% isoflurane for 10 minutes with a 0.8 L/min oxygen flow rate using an isoflurane tabletop unit (HME109, Highland Medical Equipment). The mouse was then placed in a rodent stereotaxic (Leica Angle Two™ for mouse) with continuous 1.5% isoflurane anesthesia with the head secured. A small incision was made to expose the skull, and a craniotomy was performed. The coordinates of Bregma and lambda were used as landmarks to determine the target brain region with the coordinates: anteroposterior (AP) −1.94 mm, lateromedial (ML) -1.40 mm; dorsoventral (DV) -1.35 mm (all values given relative to the bregma). The GCaMP-expressing virus (0.4 ul of AAV1-CaMKII-GCaMP6f, 2×10^{11}GC/ml) was delivered into the target region at a rate of 20 - 30 nl/min with 10 ms pulse duration by a Picospritzer (General Valve, Hollis, NH). After injection, the glass needle stayed in the brain for 5 min to prevent backflow of the virus. A tissue adhesive (3M Vetbond, St. Paul, MN) was used to close the incision. Three weeks later, the mouse was implanted with a GRIN lens for miniscope imaging.

Imaging experiment preparations

The related mouse surgery has been described in our published study (Sun et al., 2019). All the animals were implanted with a GRIN lens for *in vivo* calcium imaging once they were recovered from AAV1-CaMKII-GCaMP6f injection. Following the same procedure of viral

injection, animals were anesthetized under 2% isoflurane and placed in a heating pad with a setting temperature at 37C. Once applied 70% ethanol and Betadine on the shaved head, the skin tissue was opened. The connective tissue and tendons on the surface of the skull were removed by a swab and fine forcep. The mussel was dissected from the edge of the skull by a scalpel. To enhance the stability of implantation and *in vivo* imaging quality, used a bur (Meisinger, 1/4 Round Steel) to roughen the surface of the skull and implant a skull screw far away from the implantation area. Saline was used to irrigate the skull, which can reduce the overheating caused by bur and clean up the skull. We mark a center point for craniotomy on the exposed skull (AP: -2.3mm, ML: +1.75mm) and surrounding this point etch a 1-mm radius cranial window, which allows a 1.8mm diameter GRIN lens (Edmund Optics) to stabilize in it. The skull fragment is carefully removed with fine forceps and the exposed tissue was gently aspirated with a 27G flat needle. We then switched to a 29 G flat needle until seeing the white striated tissue (corpus callosum) above CA1. We stop the aspiration when the hippocampus is exposed. We then attach the prepared lens holder to the stereotaxic apparatus and gently lower the GRIN lens to the target depth (DV: -1.55mm). A small amount of crazy glue is quickly applied nearby the GRIN lens to cover the exposed tissue. The adaptive spray is used to dry the crazy glue and stabilize the lens in a short time. A thick layer of dental cement (Lang Dental Manufacturing: 1304CLR) is used to secure the micro-endoscope to the skull. We applied Kwik-Sil on the top of the lens to protect the lens from physical damage until the dental cement is dried. We waited for 2-3 weeks for the hippocampal tissue to recover from the surgery damage. A miniature epifluorescence microscope is used to check neural activity through a GRIN lens and to prepare for the placement of baseplate. The baseplate is stabilized by dental cement. We then attach a cap on the baseplate to prevent the damage of the lens caused by daily activity.

Histology and immunochemical staining

All animals were perfused after behavioral studies. 5 ml of phosphate buffered saline (PBS) was used to push out blood in the brain and followed by 25 ml PBS containing 4% paraformaldehyde. The perfused mice brains were fixed in 4% paraformaldehyde and were switched into 30% sucrose in 1 X PBS 24 hours later. In the next, the brain was frozen using dry ice and coronally sectioned in 30 µm thickness on a microtome (Leica SM2010R, Germany). Half of the hippocampal sections were mounted for the checking of GRIN Lens implantation. The contralateral hippocampal slices without implantation were immunostained with various antibodies to identify the pathology of Alzheimer's Disease. To investigate the intracellular Aβ accumulation and APP related products, we stained hippocampal sections with mouse anti-β-Amyloid primary antibody (6E10, BioLegend, 1:500 dilution, Cat: 803010) and following by an Alexa Fluor 549 conjugated donkey anti-mouse secondary antibody (Jackson Immuno Research, 1:200 dilution). For tau staining, a mouse anti-AT8 tau antibody (Thermo Fisher, 1:500 dilution, Cat: MN1000) was used and followed by an Alexa Fluor 488 conjugated goat anti-mouse IgG (Jackson Immuno Research, 1:600 dilution). Sections were stained with DAPI and cover slipped.

The images of immunostained sections were acquired by a fluorescent BX61 Olympus microscope. In addition, AAV-expressing hippocampal sections were imaged with a confocal microscope (Olympus) under a 20X objective lens. The acquired images were exported and analyzed using the software tools.

Behavioral experiments

All the animals were handled and habituated with head-mounted miniscope 5min per day for at least one week before behavior experiments. Water restriction was conducted to motivate animals to move on the track and the reduction of body weights was controlled within 15%.

Open arenas (circle and square box) After well handled, 3xTg-AD mice were habituated in two open field arenas with a head-mounted miniscope for 4 consecutive days. Circle box (36 cm in diameter) and square box (26 cm in length) were adorned with various visual cues. On the first day, animals explore the circular environment for 10 minutes, then are transferred to the adjacent square box for another 10 minutes. On the second day, animals ran in each arena for 10 minutes as day one except exposing to the square arena first then to the circular box. After habituation in two boxes for four days, the neuronal activities of animals were recorded by miniscope in two different environments for another four days.

Linear track 3xTg-AD mice were trained to run on the linear track for 4 days during the habituation sessions. The one-meter linear track is made of black plastic materials. Two water reward zones are located at the end of the linear track. The walls of reward zones were adorned with various visual cues such as spatial information. 10% ethanol was used to get rid of the odor cues left from other mice in the previous behavioral session. In the beginning of each session, the mouse was released in the middle of the track and ran to the end of track to get 10ul of water reward. Once animals reach the minimal 50 laps within 10 minutes in a training session, we will start experimental recording the next day. On the first day of the miniscope recording, animals were required to complete two sessions in the same track with a horizontal direction. The animal had a 2-minute break time in the home cage during each session. At least 40 laps per session was acquired for the data processing. On day 2, animals ran on the same linear track with a horizontal direction as day 1 in session 1. Then, the linear track was rotated in a 90-degree direction, named as “vertical” relative to the recording environment. After 2 minutes of rest in the home case, the animal went through another 40 laps in the vertical track. On the third day, the animal ran on the vertical track first then back to the horizontal track.

Data preprocessing

The raw calcium recordings down-sampled to 15 frames/sec. Motion correction is applied to the neuron recordings with the well-established motion correction streamline NormCorre (Pnevmatikakis & Giovannucci, 2017), to fix the rigid movements caused by potential scope movement across time.

Extract neural calcium signal using CNMF-E

The calcium signal of each neuron is gathered from video data using the Extended Constrained Nonnegative Matrix Factorization (CNMF-E) framework proposed by Zhou et al (P. Zhou et al., 2018). This framework using the following model to represent the video data:

$$y(x,t) = \sum_{i=1}^{K} a_i(x) * c_i(t) + b(x,t)$$

Where $y(x,t)$ represents the raw video data, $a_i(x)$ represent the neuron's spatial footprint, $c_i(t)$ represents the calcium activity and $b(x,t)$ represent the background activity. By applying sophisticated background approximation, CNMF-E can efficiently remove baseline noise, and achieve the neuron footprint and calcium response via deconvolution. To remove false positive detections, a 2D gaussian kernel is fit for the spatial footprint of each neuron, and Kullback–Leibler divergence is calculated between the footprint and gaussian kernel. Kullback–Leibler divergence quantifies the similarity between two distributions, and here it represents the closeness between the actual neuron footprint and the theoretically perfect footprint. Neurons with divergence values larger than 0.6 are kept for subsequent analyses.

CNMF-E is applied to different trials independently. To identify common neurons across the trials, for each pair of extracted neurons across two trials, level of footprint overlaps between two neurons in two different trials, and the similarity of distance pattern between the neuron and its neighbors. Both measures will be converted to probability values indicating the chance for the

two neurons to be aligned, and the final alignment probability is the average of the overlap probability and distance pattern probability. The neuron pairs with the highest alignment probability than go beyond 0.25 will be considered as the same neuron across two trials.

Mouse movement behavior extraction

The behavior trajectory is extracted from the behavior videos recorded together with neuron responses, with a sample rate of 30 Hz. The bottom of the box is selected as the region of interest (ROI), to restrict the area for behavior detection. The behavior trajectory is defined as the positions of red LED centroid across all frames and is smoothed using moving average method.

Spatial rate map calculation

The calcium spike trains are calculated by applying the CNMF-E embedded deconvolution algorithm, OASIS (Friedrich et al., 2017), to the extracted temporal calcium dynamics. A threshold of 10% of maximum amplitude of the neurons' spike train is set for each neuron, and potential events with an amplitude lower than the threshold are excluded.

The behavior trajectory is aligned with the calcium response according to the timestamp that records the correspondence between behavior recordings and calcium recordings. The ROI is divided into 10mm*10 mm bins. The total time mouse spent inside a bin is counted as bin time (sec). The total number of calcium peaks above threshold is added up and normalized by bin time to achieve event rate. When presenting, smoothing is applied to the event rate map with a 100mm*100mm 2D gaussian kernel (delta = 20mm)

dF/F calculation

When comparing amplitude values, each neuron will have its response normalized to dF/F, which is calculated as $\frac{\mathrm{dF}}{\mathrm{F}} = \frac{dF - mean(dF)}{mean(dF)}$

Information score and place cell

The information score of recorded neurons is calculated as information per second and information per spike introduced by Skaggs et al. in 1993. Only the running session with speed larger than 0.5cm/s are included in calculation, and the spatial bins with bin time smaller than 0.1 sec are excluded to avoid non-existed trespass caused by trajectory smoothing. For a rate map with n bins, The information per second is defined as:

$$Information\ Score(bits/second) = \sum_{i=1}^{n} P_i \lambda_i log_2 \frac{\lambda_i}{\lambda}$$

$$Information\ Score(bits/spike) = \sum_{i=1}^{n} P_i \frac{\lambda_i}{\lambda} log_2 \frac{\lambda_i}{\lambda}$$

P_i is the probability the mouse stays in the i th bin, which is represented as the ratio between the times in the bin and total times of the trial. λ_i is the firing rate of the i th bin, while λ is the average firing rate across the trial. Place cells are defined by comparing the information per spike of each neuron with its shuffled baseline. The calcium responses will be divided into 100 trunks and randomly shuffled 100 times, to disrupt their correspondence with behavior and generate a distribution of potential score values the neuron may achieve. The neuron will be determined as a place cell if its original score value is higher than the 95th percentile of the shuffled distribution.

Spatial coherence

Spatial coherence measures the level of spatially contiguous activity the neuron exhibits, that is if the spatial bin with high activity is located close to each other, a high Spatial coherence score would be achieved (Zhang et al. 2014). Spatial coherence is calculated as the Pearson correlation between the activity of each spatial bin and the average activity of its 3x3 neighboring bins.

Sparsity

Sparsity is a measure of the fraction of environment in which the cell is active (Skaggs et al., 1996). The definition is $Sparsity = \frac{\Sigma(p_i\lambda_i)^2}{\Sigma p_i{\lambda_i}^2}$, where p_i is the probability the mouse stays in the i th bin, which is represented as the ratio between the times in the bin and total times of the trial, and λ_i is the firing rate of the i th bin.

Statistical analyses

Data are presented as the mean ± s.e.m, as indicated. Mann-Whitney U test is used to test the influence of genotype and age to the neuron number. We use the linear mixed-effect model (LME) to address the repeat measurement issues inside our data. The main idea of LME ("fitlme" in Matlab) is to view the variables to be tested, such as genotypes, as distributions around the potential groupings inside data, such as the neurons from the same mouse, and when conducting statistical modeling and hypothesis testing, the influence of grouping on tested variable will be taken into account (Laird & Ware, 1982; Mclean et al., 1991). Also, compared with a paired t-test or repeated measures ANOVA, LME can handle unbalanced designs and missing values, and has greater statistical power in the presence of missing values. The importance of LME and its more generalized versions has been increasingly recognized in recent studies involving large cell sample data collected from a relatively small number of animals (Indersmitten et al., 2019; Stobart et al., 2018). For cumulative distributions, Kolmogorov-Smirnov (KS) test is applied for testing the difference. The level of statistical significance was defined as $P \leq 0.05$.

Results

Age-dependent amyloid-β and tau pathology in 3xTg-AD mice

We used triple-transgenic Alzheimer's disease (3xTg-AD) model mice that overexpress APP_{Swe}, $PS1M_{146V}$ and tau_{P301L} transgenes that contribute to both amyloid beta (Aβ) plaque and neurofibrillary tangle formation (Belfiore et al., 2019; Oddo et al., 2003). Unlike most other mouse models, 3xTg-AD model mice uniquely develop two AD hallmark pathological features: plaque and tangle formation (Mesulam, 2000; Oddo et al., 2003). To determine age-related and AD progression effects, we compared littermate control and AD-like mice at young and old ages (young age, 3.6 - 6.5 months old versus old age, 18 - 21 months old). The age choices are guided by behavioral and neuropathological findings by our and other groups (Baglietto-Vargas et al., 2018; Belfiore et al., 2019; Mesulam, 2000; Oddo et al., 2003; Stimmell et al., 2019).

To measure age-dependent plaque and tau aggregate formation in the AD mouse hippocampus, we immunostained 3xTg-AD and controlled genetic background non-transgenic (Non-Tg) sections with Aβ and Tau antibodies. All hippocampal sample sections were from mice that had undergone imaging and behavioral experiments; thus, these results can be correlated with AD neuropathology. Across at least 3 different sets of immunostaining experiments, we confirm that 6.5-month-old 3xTg-AD mice exhibit intracellular Aβ accumulation in hippocampal pyramidal neurons visualized by immunostaining with the 6E10 antibody shown in red, counterstained with DAPI in blue showing cell nuclei (Figure 2.1A, bottom left). Extracellular Aβ deposits are distributed throughout the CA1 pyramidal layers and extend to all layers of the hippocampus in 3xTg-AD mice by 18 months (Figure 2.1A, bottom right). In contrast, no Aβ deposits are detected in the control Non-Tg mice at either young (Figure 2.1A, top left, 6.5 months) or old ages (18 months) (Figure 1A, top right). The phospho-tau (Ser202, Thr205) monoclonal

antibody (AT8) staining, shown in red and counterstained with DAPI shown in blue, was used to identify the presence of human tau pathology in 3 different sets of immunostaining experiments. Anti-AT8 staining shows that tau aggregates in several CA1 pyramidal neurons in aged 3xTg-AD mice (18-month-old, white arrow, Figure 2.1B, bottom right). In comparison, only sparse AT8+ cells are found in hippocampal CA1 in younger 3xTg-AD mice aged 6.5-months (Figure 2.1B, bottom left). Tau pathology is not detected in the young and old control Non-Tg mice (Figure 2.1B, top left and right). Consistent with previous work, Aβ accumulation is detectable at an earlier age than tau pathological accumulation in 3xTg-AD mice, and both neuropathological features are absent in age matched control Non-Tg mice (Belfiore et al., 2019; Oddo et al., 2003). While age-dependent pathological changes correlate with AD-related memory behavioral deficits (Belfiore et al., 2019; Stimmell et al., 2019), spatial coding of *in vivo* neural circuit activities in the AD mouse model has not been studied during spatial exploration of environments.

Miniscope imaging of neural population activities in 3xTg-AD hippocampal CA1

To determine whether hippocampal CA1 ensemble activities during spatial exploration are altered in an age-dependent fashion in 3xTg-AD mice, we used head-mounted miniscopes to image *in vivo* calcium transient ensemble activities in the 3xTg-AD mouse hippocampal CA1 and compared ensemble activities with age-matched control Non-Tg animals sharing the same genetic background (Figure 2.2). To visualize neural calcium activity in the dorsal hippocampal CA1 region, mice were injected with the AAV1-CamKII(0.4)-GCaMP6f virus to restrict expression to CA1 excitatory neurons (Figure 2.2A). This 0.4 Kb promoter is derived from murine α-Calcium/calmodulin-dependent kinase II (CaMKII) and is reported to show up to 95% specificity to excitatory neurons in the cerebral cortex (Scheyltjens et al., 2015).

The cortex overlying the hippocampus was removed, then a gradient refractive index GRIN lens was implanted above CA1 (Figure 2.2B). The implanted GRIN lens allows repeated and longitudinal imaging of the same group of neurons in single cell resolution across prolonged periods up to weeks and months. A small metal baseplate is glued around the lens, and the head-mounted miniscope is magnetically attached to the baseplate. As established in our published studies (Grieco et al., 2021; Grieco et al., 2020; Sun et al., 2019; Wong et al., 2021), GRIN lens implants and the stability of the miniscope attachment permit longitudinal dynamic imaging results to be aligned across sessions and multiple days due to stable registration. Hundreds of neurons can be captured simultaneously in a 700 μm x 450 μm field of view, with a resolution of ~0.9 μm per pixel (Figure 2.2C).

Spatial footprints of individual neurons and their corresponding calcium transients were detected and extracted from raw video data using the established CNMF-E method (Pengcheng Zhou et al., 2018) (Figure 2.2C-D). Overall, visual inspection that the extracted neuronal numbers in AD mice are less than control mice per the field of view (Figure 2.2C), as would be expected due to neurodegenerative loss. By averaging the numbers of extracted neurons across open field exploration trials, the 3xTg mice shows a significant trend to have less neurons than the Non-tg mice at both ages. Meanwhile, young Non-Tg mice has more cells in comparison with aged Non-Tg mice, and a similar significant trend is seen between the two age groups of 3xTg AD mice (number of neurons: young Non-Tg 653.7 ± 83.7 cells, N = 6 mice; aged Non-Tg, 337.7 ± 44.3 cells, N = 10 mice; young 3xTg-AD, 450.9 ± 66.4 cells, N = 8 mice; aged 3xTg-AD, 211.0 ± 25.8 cells, N = 8 mice; Mann-Whitney U test, young Non-tg vs aged Non-tg: p = 0.0110, young 3xTg-AD vs. aged 3xTg-AD: p=0.0207, young Non-tg vs. young 3xTg-AD: p=0.0426, young Non-tg vs. young 3xTg-AD: p=0.0434). (Fig. 2.3 A). When pooled 3xTg-AD and Non-Tg mice together,

the aged group overall has a lower number of extracted neurons than the young group (young group, 520.1 ± 57.3 cells, N = 15 mice; aged group, 312.2 ± 11.2 cells, N = 18 mice, Mann-Whitney U test, p = 0.0006) (Fig. 2.3 B). This suggests that there are fewer active cells per unit of space in hippocampal CA1 in aging and AD conditions.

To quantitatively characterize hippocampal neuronal ensemble activities during free exploration, we constructed spatial firing rate maps for the extracted CA1 neurons during animal exploration in open circle (diameter, 36 cm) and square (26 cm x 26 cm) arenas. Arenas were divided into 1 cm x 1 cm spatial bins. The binned calcium transient rate is defined by dividing the total number of calcium activity peaks by the total exploration times within each bin. Transients as defined by sharp peaks in activity exceeding 10% of the maximum peak amplitude. The spatial firing rate maps of example neurons of both ages and genotypes are shown in Figure 2.2 E-H. For Non-tg mice at both ages, individual excitatory CA1 neurons can display calcium firing activities restricted to specific locations, which is consistent with the well-described 'place-specific' action potential firing of CA1 excitatory neurons (Figure 2.2E, G). For 3xTg-AD mice at both ages, individual excitatory CA1 neurons show less place-specific activities as characterized by more diffused firing and less in-field event rates (Figure 2.2F, H), which suggests decreased signal-to-noise and potential impairment of spatial representations in CA1.

Age- and AD- dependent neural activity differences in mouse hippocampal CA1 during open field exploration

To investigate the AD and age-related differences in hippocampal excitatory CA1 neuron activities, we compared the calcium transient rates and calcium event amplitudes of hippocampal CA1 neurons from 3xTg-AD and Non-Tg genotypes at different ages (Figure 2.2D, Figure 2.4A and B). For the young age group, overall, the 3xTg-AD genotype displays a significantly higher

calcium event rate compared with the Non-Tg control (Figure 2.2E-F, Figure 2.4A. Non-Tg young: 0.0752 ± 0.0010 Hz (1180 cells from 5 mice); AD young: 0.0965 ± 0.0013 Hz (1076 cells from 8 mice); linear mixed-effects (LME) model analysis: p = 0.0091). Similarly, for the old age group, on average the old AD mice exhibit a higher firing rate than old Non-Tg mice (Figure 2.2G-H, Figure 2.4A. Non-Tg old: 0.0497 ± 0.0012 Hz (716 cells from 9 mice); AD old: 0.0612 ± 0.0018 Hz (430 cells from 8 mice); LME: p = 0.0094). We also note that for both control and 3xTg-AD mice, age decreases the overall rate of excitatory neural calcium activities in mouse CA1 (Non-Tg young vs Non-Tg old, LME: $p = 3.8744 \times 10^{-5}$; AD young vs AD old, LME: $p=1.5095 \times 10^{-5}$).

In terms of the overall calcium event amplitudes (ΔF/F), we find that 3xTg-AD genotype exhibits lower amplitudes than Non-Tg mice at the young age (Figure 2.2E-F, Figure 2.4B. Non-Tg young: 7.386 ± 0.100 in the unit of dF/F (1180 cells from 5 mice); AD young: 5.725 ± 0.064 dF/F, (1076 cells from 8 mice), LME: p = 0.0066). The calcium amplitudes are generally higher for the old age group, compared with the young age group (Figure 2.2G-H, Figure 2.4B. Non-Tg old: 11.680 ± 0.322 dF/F (716 cells from 9 mice); AD old: 11.700 ± 0.619 dF/F (430 cells from 8 mice). Non-Tg young vs Non-Tg old: LME: p=0.0055, AD young vs AD old: LME: p=0.0287). The 3xTg-AD and Non-Tg genotypes did not differ significant at the old age (LME: p=0.6388).

These data suggest that 3xTg-AD mouse hippocampal circuits are associated with higher neural ensemble activities relative to Non-Tg controls at either age, which is supported by neural circuit hyper-activity with the accumulation of Aβ as observed in anaesthetized AD mouse preparations (Busche et al., 2012; De Strooper & Karran, 2016; Harris et al., 2020).

Spatial coding impairments of 3xTg-AD CA1 neurons during open field exploration

Given that 3xTg-AD mice show hippocampal spatial memory impairments (Baglietto-Vargas et al., 2018; Oddo et al., 2003; Stimmell et al., 2019), we next investigated the differences

of CA1 neuron spatial coding abilities between 3xTg-AD and Non-Tg genotypes at different ages. Using tetrode electrical recordings, a previous study using a different AD mouse model (single APP knock-in, APP-KI) shows that the APP-KI mice exhibit deteriorated spatial tuning represented by lower information score values (H. Jun et al., 2020). We used a similar approach by calculating the information scores in bits/event (bits/event) from pooled CA1 place cells of each genotype and age group and comparing their cumulative distributions. The metrics of bits/event and bits/second measure different aspects of activity across sub-regions (bins) of an environment. Both the bits/second and bits/event metrics utilize the distributions of firing rate across binned locations in an environment (Skaggs et al., 1999). The bits/event metric is increased when a subset of positional firing rates are high against a low mean positional firing rate. Because of this, neurons with place specific activity tend to have high bits/event values.

We find spatial coding impairments of 3xTg-AD hippocampal CA1 neurons in freely moving animals during open field exploration. The bits/event metric shows that neural calcium events of the 3xTg-AD mice encode less information than Non-Tg mice, at both the young and old age (Figure 2.4C; the respective 50%-cumulative values for Non-Tg young (233 place cells from 5 mice), AD young (214 place cells from 8 mice), Non-Tg old (104 place cells from 9 mice) and AD old (131 place cells from 8 mice) are 2.2410, 1.9409, 1.9136 and 1.6586. Non-Tg young vs AD young: $p = 4.1683 \times 10^{-12}$. Non-Tg old vs AD old: $p = 0.0008$, Non-Tg young vs Non-Tg old: $p = 1.1583 \times 10^{-8}$, AD young vs AD old: $p = 1.1370 \times 10^{-6}$, two-sample Kolmogorov-Smirnov test).

To further compare the spatial coding abilities of hippocampal CA1 excitatory neurons across the genotype and age groups, we measured the sparsity and spatial coherence (Jung et al., 1994; Zhang et al., 2014) of calcium event rate maps for all CA1 neurons pooled from each mouse group. The sparsity index measures the fraction of the exploration area where a neuron fires spikes,

and lower sparsity indicates more constrained firing activities at specific locations (Jung et al., 1994). Coherence measures the extent to which adjacent positional firing rate bins share similar firing rates. For truly place-specific activity, coherence is high because spatial bins with high rates are concentrated in one location. We find that at either age, 3xTg-AD CA1 cells exhibit higher sparsity values than Non-Tg, which complements the bits/event measures and indicate the lower spatial selectivity of place cell firing in 3xTg-AD mice (Figure 2.4 E; the respective 50%-cumulative values for Non-Tg young (1180 cells from 5 mice), AD young (1076 cells from 8 mice), Non-Tg old (716 cells from 9 mice) and AD old (430 cells from 8 mice) are 0.0746, 0.0957, 0.0492 and 0.0657. Non-Tg young vs AD young: $p = 1.2703 \times 10^{-31}$, Non-Tg old vs AD old: $p = 2.0458 \times 10^{-7}$, two-sample Kolmogorov-Smirnov test). Further, for both 3xTg-AD and Non-Tg, mice in the young age group have a higher sparsity than the old age group (Figure 2.3 E; Non-Tg young vs Non-Tg old: $p = 9.0277 \times 10^{-42}$; AD young vs AD old: $p = 1.0343 \times 10^{-25}$, two-sample Kolmogorov-Smirnov test). In addition, the 3xTg-AD mice show overall higher coherence values of activity rate maps than Non-Tg mice at the old age (Figure 2.4 F; the respective 50%-cumulative- values for Non-Tg young (1180 cells from 5 mice), AD young (1076 cells from 8 mice), Non-Tg old (716 cells from 9 mice), and AD old (430 cells from 8 mice): 0.4369, 0.4437, 0.4053 and 0.4286. Non-Tg young vs AD young: $p = 0.0728$, Non-Tg old vs AD old: $p = 5.4990 \times 10^{-4}$, two-sample Kolmogorov-Smirnov test). Younger mice show higher coherence than older mice for both genotypes (Figure 2.3 F; Non-Tg young vs Non-Tg old: $p = 2.3031 \times 10^{-6}$, AD young vs AD old: p=0.0177, two-sample Kolmogorov-Smirnov test). As spatial coherence measures the correlation between the activity of each bin and the averaged activities of its neighborhood bins in a rate map (Jung et al., 1994), we reason that the more diffuse firing fields of old 3xTg-AD mice may result in higher spatial coherence.

Spatial coding deficits of 3xTg-AD CA1 neurons in linear track trials

We extended our investigation to a linear track environment. Population calcium transient activities in hippocampal CA1 were imaged with head-mounted miniscopes while mice ran along a 1-meter linear track (width, 3 cm) for a water reward at each end. CA1 excitatory neurons that exhibit place selective activities can be identified from the populations across the genotypes and ages (Figure 2.5 A-D). We quantitatively analyzed the place-specific activities in linear track trials, as we did for open field exploration. We find that the calcium event rates across mouse groups do not exhibit significant differences (Figure 2.5 E), but AD mice show a significant difference from Non-Tg mice in terms of calcium event amplitudes (Figure 2.5 F; Non-Tg young (1742 cells from 6 mice): 5.745 ± 0.112 dF/F; AD young (1988 cells from 8 mice): 4.534 ± 0.076 dF/F; Non-Tg old (1136 cells from 5 mice): 4.573 ± 0.107 dF/F; AD old (1560 cells from 5 mice): 5.064 ± 0.079 dF/F. Non-Tg young vs AD young, LME: $p = 0.0167$; Non-Tg old vs AD old, LME: $p=0.0495$; Non-Tg young vs Non-Tg old, LME: $p = 0.0132$; AD young vs AD old, LME: $p = 0.0354$).

Consistent with our finding in mouse exploration of open fields, we find that for both ages, 3xTg-AD mice exhibit lower spatial information score in bits/event than Non-Tg mice (Figure 2.5G; the respective 50%-cumulative values for Non-Tg young (238 place cells in direction 1 + 246 place cells in direction 2, from 6 mice), AD young (213 place cells in direction 1 + 237 place cells in direction 2, from 8 mice), Non-Tg old (163 place cells in direction 1 + 159 place cells in direction 2, from 5 mice) and AD old are (259 place cells in direction 1 + 272 place cells in direction 2, from 5 mice) are 2.0727, 1.9371, 1.8581 and 1.4978. Non-Tg young vs AD young: $p=0.0432$, Non-Tg old vs AD old: $p= 0.0010$, Non-Tg young vs Non-Tg old: $p= 8.7241*10^{-7}$, AD young vs AD old: $p=3.4423*10^{-5}$, two-sample Kolmogorov-Smirnov test).

During linear track trails, hippocampal CA1 excitatory neurons in old 3xTg-AD mice have higher sparsity values than young 3xTg-AD mice, while for control mice, there are no significant differences between ages (Figure 2.5H; the respective 50%-cumulative values for Non-Tg young (1742 cells (each direction) from 6 mice), AD young (1988 cells (each direction) from 8 mice), Non-Tg old (1136 cells (each direction) from 5 mice) and AD old (1560 cells (each direction) from 6 mice) are 0.0490, 0.0429, 0.0499, and 0.0559. Non-Tg young vs AD young: $p= 1.2231 \times 10^{-9}$, Non-Tg old vs AD old: $p= 1.7939 \times 10^{-5}$, Non-Tg young vs Non-Tg old: $p = 0.0818$; AD young vs AD old: $p = 3.4707 \times 10^{-31}$, two-sample Kolmogorov-Smirnov test). 3xTg-AD mouse cells exhibit higher spatial coherence values than Non-Tg mice (Figure 2.5 I; the respective 50%-cumulative values for Non-Tg young (1742 cells (each direction) from 6 mice), AD young (1988 cells (each direction) from 8 mice), Non-Tg old (1136 cells (each direction) from 5 mice) and , AD old (1560 cells (each direction) from 6 mice) are 0.3573, 0.3658, 0.3632 and 0.3778. Non-Tg young vs AD young: $p = 8.8051 \times 10^{-10}$, Non-Tg old vs AD old: $p= 2.7640 \times 10^{-11}$, Non-Tg young vs Non-Tg old: $p=7.9276 \times 10^{-12}$, AD young vs AD old: $p=2.7437*10^{-17}$, two-sample Kolmogorov-Smirnov test).

Locomotion modulation of 3xTg-AD mouse CA1 neural population activities

It is known that locomotion states have significant effects across rodent sensory systems including visual and auditory circuits (M. Arriaga & E. B. Han, 2017). While both the calcium activities of CA1 excitatory neurons and inhibitory neurons can be modulated by locomotion (Fuhrmann et al., 2015; Góis & Tort, 2018), locomotion effects on hippocampal neural calcium population activities have not yet been studied in freely moving animals. Miniscope imaging has an advantage of monitoring neural ensemble activities in hippocampal CA1 of animals during free

moving conditions, thus providing the opportunity to examine the modulatory effects of free locomotion on CA1 neural calcium activity ensembles across different groups.

As shown in Figure 2.6A, the calcium activities of hundreds of excitatory neurons recorded during one session from each example mouse are displayed in raster plots over the exploration time. We delineate the high-velocity epochs (black vertical bars) below the raster plots to enable visual comparisons between the neural activity level and locomotion velocity. The high-velocity epoch is defined as the duration when the velocity goes above the averaged trial velocity of each group (Figure 2.6B). To further illustrate the relationship between population calcium responses and velocity overtime, we align the z-scored ensemble calcium response trace with the z-scored velocity trace. Interestingly, compared with control mice at the young or old age, overall neural population calcium activities in hippocampal CA1 of AD mice appear to be more closely modulated by locomotion velocities and CA1 ensemble amplitudes are positively correlated with locomotion velocity changes (Figure 2.6A).

We quantitatively examined the relationship between calcium activity amplitude and velocity by calculating the correlation between individual neurons' calcium responses and velocities. We apply a 15 sec Gaussian window (2.5 sec standard deviation) to smooth both calcium response and movement velocity traces in the time-series, then compare the cumulative distributions of correlations across different genotypes and ages. Our quantification confirms our qualitative observations in Figure 2.6A. Compared with age-matched controls, young and old 3xTg-AD CA1 neurons show stronger correlations between calcium response amplitudes and locomotion velocities (Figure 2.6C; the respective 50%-cumulative values for Non-Tg young (1180 cells from 5 mice), AD young (1076 cells from 8 mice), Non-Tg old (716 cells from 9 mice) and AD old (430 cells from 8 mice) are 0.0435, 0.0561, 0.0341 and 0.0930. Non-Tg young vs AD

young: $p = 9.2871 \times 10^{-6}$, Non-Tg old vs AD old: $p = 1.6663 \times 10^{-10}$, two-sample Kolmogorov-Smirnov test). This holds true when we only include place cells for analysis. Place cells were defined as cells with spatial information score above the chance level (see details in the Method). The locomotion effects appear to be more robust for the place cells (Figure 2.6D; the respective 50%-cumulative values for Non-Tg young (233 place cells from 5 mice), AD young (214 place cells from 5 mice), Non-Tg old (104 place cells from 9 mice) and AD old (131 place cells from 5 mice) are 0.1228, 0.1560, 0.0901 and 0.1556. Non-Tg young vs AD young: p=0.0093, Non-Tg old vs AD old: p=0.0016, two-sample Kolmogorov-Smirnov test).

Discussion

Previous work on AD has focused on molecular and neuropathological features as they correlate to cognitive defects. AD research is now increasingly focused on mechanistic changes at the level of neuronal circuits (Harris et al., 2020). In the present study, we have examined neural calcium activities of hippocampal CA1 neuronal populations in freely behaving 3xTg-AD mice and controls at young (3 - 6.5 months on average) and old (18 - 21 months old) ages. We leveraged the advantages of miniscope-based GCaMP calcium imaging to examine the impairments of spatial representation and spatial coding across large neuronal ensembles by comparing hippocampal CA1 excitatory neural ensemble activities during open-field exploration, and track-based route-running behaviors in age-matched AD and control mice. We have identified AD- and age-related differences in neural calcium activities and have determined deficits in spatial information coding and place remapping associated neural activities in hippocampal neural ensembles in the 3xTg-AD mouse model. We also find locomotion significantly modulates the amplitude of hippocampal neural ensemble activities in 3xTg-AD mice, but not in non-transgenic controls during open field exploration.

Many transgenic AD models have been used in research studies to date, but most models only contain mutation genes for the progression of Aβ plaques, such as APP Tg2576, APP/PS1 and 5xFAD. These models are convenient for the detection of Aβ accumulation at early age but do not take into account the tau pathology in the late AD stage. In our study, we used the 3xTg-AD mouse model that contains the genetic mutations contributing to both pathological markers (Mesulam, 2000; Oddo et al., 2003). AD related neurodegeneration may affect hippocampal CA1 neural activation as 3xTg-AD hippocampal CA1 imaging fields have a smaller number of extracted neurons compared to control mouse hippocampal CA1 fields. Aging might also have effects, as the aged group also has a lower number of extracted neurons relative to the young group. The age-dependent plaque and tau aggregate formation in the 3xTg-AD mouse hippocampus is correlated well with CA1 neural activity alterations identified in our imaging experiments across the ages and genotypes. Our imaging results are also supported by the deficiency in spatial memory behaviors observed in 3xTg-AD mice (Baglietto-Vargas et al., 2018; Oddo et al., 2003; Stimmell et al., 2019).

We identify AD- and age- dependent neural activity differences in mouse hippocampal CA1 during open field exploration. We find that 3xTg-AD CA1 excitatory cells have significantly higher calcium firing rates compared with controls either at young or old age, indicating that *in vivo* enhanced neuronal ensemble activity is a disease feature. Increased ages are correlated with decreased neural calcium firing rates across genotypes. We also have examined calcium event amplitudes. We find that 3xTg-AD CA1 cells have lower amplitudes than control mice at the young age, and that neural calcium amplitudes are generally higher for AD and control CA1 cells, compared with the cells of young age groups. These data suggest AD and aging share related alterations in neural activities and calcium homeostasis. The higher neural ensemble calcium

activities found in 3xtg AD mouse hippocampal CA1 may be a critical AD disease feature. which is supported by neural circuit hyper-activity observed in anaesthetized AD mouse preparations (Busche et al., 2012; De Strooper and Karran, 2016; Harris et al., 2020).

Our data demonstrate spatial coding defects of hippocampal CA1 ensemble activities in 3xTg-AD mice, as our overall imaging results in both open field and linear track environments indicate that neuronal populations of 3xTg-AD mice show lower spatial information scores compared with control mice. In open field, spatial firing of CA1 neurons of old 3xTg-AD mice also displays higher sparsity and spatial coherence compared with those from control mice. This supports the notion that place-specific firing fields of CA1 neurons in the AD condition tend to be larger in size, which indicates less place specificity for spatial representation. In linear track, while 3xTg-AD mice always display higher coherence than Non-tg mice across ages, at young age 3xTg-AD display lower sparsity compared to Non-tg mice. However, considering the lower information score of the 3xTg-AD animal, the young 3xTg-AD could have small but scattered firing activities across multiple positions.

Our finding that locomotion significantly modulates the amplitude of hippocampal neural ensemble activities in 3xTg-AD mice, but not in non-transgenic controls is another important new finding. During movement, hippocampal local field potential (LFP) activity is characterized by θ-frequency oscillations; in contrast, during awake immobility, LFP activity is punctuated by large, irregular activity containing periods of sharp-wave/ripple (SWR) events. Much current research related to this is focused on hippocampal interneurons as their activity is highly modulated with locomotion speed (Moises Arriaga & Edward B. Han, 2017; Góis & Tort, 2018), while locomotion modulates excitatory neurons to a lesser degree (Góis & Tort, 2018). Given that AD neurodegeneration can alter circuit excitation/inhibition balance, it can be inferred that the speed-

correlated inhibition of pyramidal neurons will be weakened in the AD condition. Indeed, our results indicate that CA1 place cells from 3xTg-AD mice exhibit obviously stronger speed modulation on their neural calcium activity amplitudes. Whether decrease in inhibition will lead to higher activity modulation of excitatory neurons in AD related neural circuits requires further investigation.

In conclusion, we applied miniscope calcium imaging in 3xTg-AD model and Non-Tg mice to determine the AD- and aging- related impacts on hippocampal neural population activities. Our data show neural activity alterations and spatial coding defects in CA1 neuronal ensembles that correlate with the development of AD pathology and AD-related spatial memory behavioral deficits.

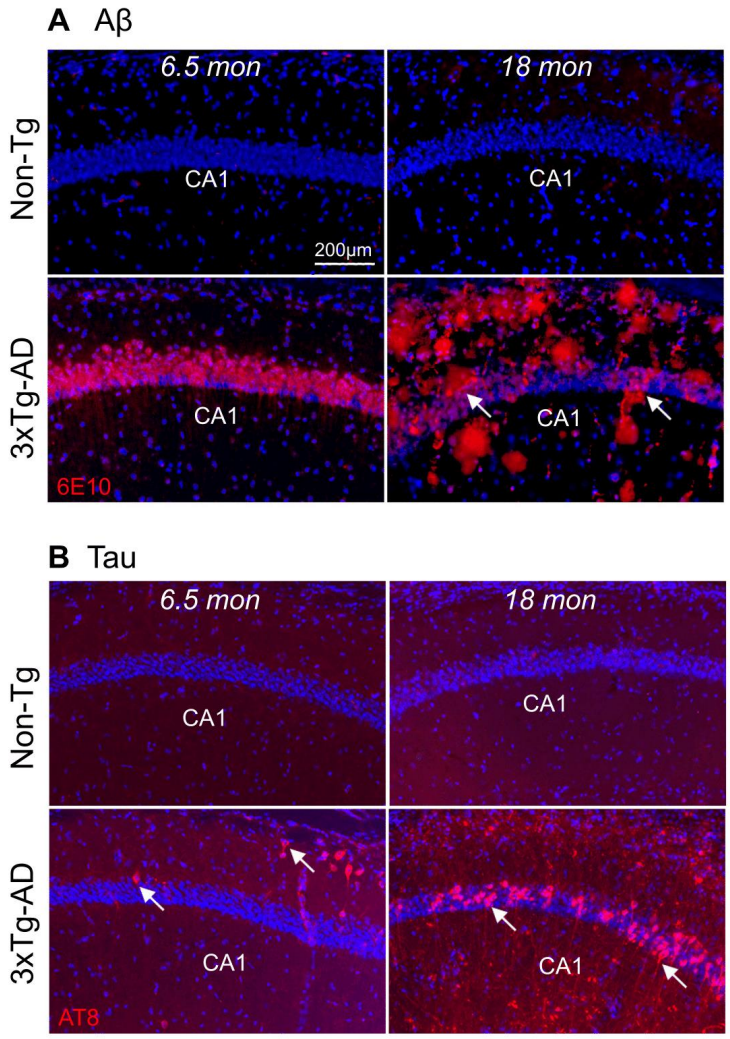

Figure 2.1. Age-dependent change in amyloid beta (Aβ) and phospho-tau accumulation in 3xTg-AD mouse hippocampus A. Comparison of Aβ pathology in the 6.5-month-old and 18-month-old 3xTg-AD and control, Non-Tg mice. 6.5-month-old 3xTg-AD mice show intraneuronal Aβ staining in the pyramidal layer of hippocampal CA1 (left bottom panels). Aβ staining is red and DAPI staining is blue. The accumulation of Aβ (plaques, arrows) is distributed across all the layers of hippocampal CA1 in an 18-month-old 3xAD-Tg mouse (bottom right panel) as compared to a non-transgenic control mouse (Non-Tg) (top right panel). **B.** Phospho-tau builds up in the 3xTg-AD mouse hippocampus. Tau staining is red. 6.5 months old 3x-Tg-AD (bottom left) mice shows sparse tau labeling in distal CA1. The 18-month-old group exhibits elevated tau pathology in hippocampal CA1 pyramidal cells (arrows) (bottom right). The Non-Tg (top two panels) mouse hippocampus does not develop tau pathology. Scale bar = 200 μm. Image usage is approved by the first author, Xiaoxiao Lin.

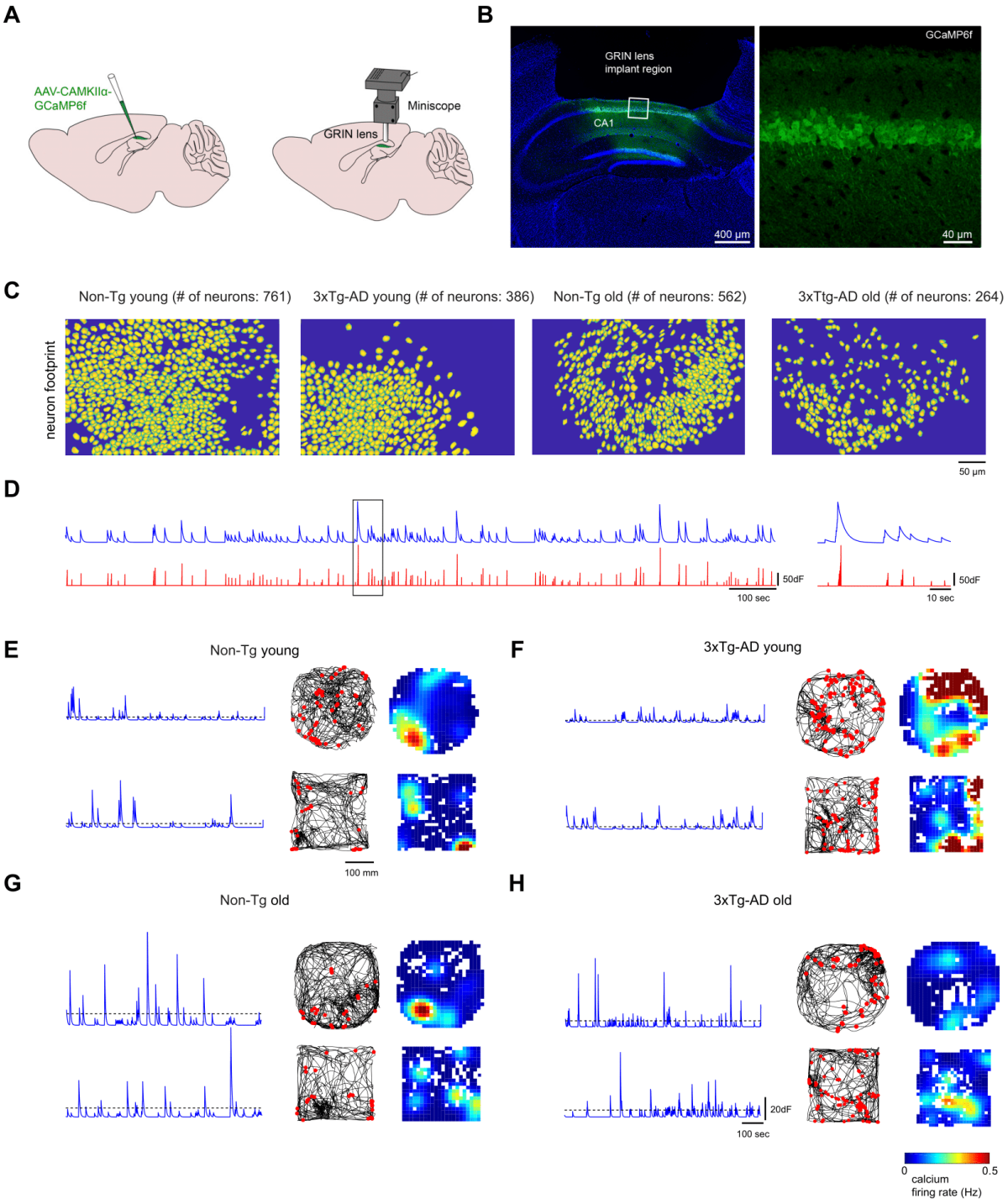
A
AAV-CAMKIIα-
GCaMP6f
Miniscope
GRIN lens
B
GRIN lens
implant region
CA1
400 μm
GCaMP6f
40 μm
C
Non-Tg young (# of neurons: 761)
3xTg-AD young (# of neurons: 386)
Non-Tg old (# of neurons: 562)
3xTtg-AD old (# of neurons: 264)
neuron footprint
50 μm
D
50dF
100 sec
50dF
10 sec
E
Non-Tg young
100 mm
F
3xTg-AD young
G
Non-Tg old
H
3xTg-AD old
20dF
100 sec
0
0.5
calcium
firing rate (Hz)

Figure 2.2. Miniscope imaging of in vivo neural calcium activities of hippocampal CA1 exciatory neurons in 3xTg-AD and Non-Tg mice A. The scheme for viral injection and miniaturized fluorescent microscope (miniscope) recording in hippocampal CA1 region. AAV1 was injected to express GCaMP6f in CA1 excitatory neurons. A 2.8-mm diameter GRIN lens (shown in grey) was implanted at the same location as AAV1 injection site for *in vivo* calcium signal recording in the behavioral animals. **B**. A coronal section image shows the location for GRIN lens implantation in hippocampal CA1. DAPI staining is blue. GCaMP6f signal is green. Scale bar = 400 μm. Right panel: the higher magnificent image of the left panel. The GCaMP6f infected cells are restricted to the pyramidal layers of the hippocampal CA1 region. Scale bar = 40 μm. **C.** Examples of neuron footprints from CNMF-E extraction for data processing. Left to right, the example mice are from young age Non-Tg, young age 3xAD-Tg, old-age Non-Tg and old-age 3xAD-Tg, respectively. **D.** Extracted calcium traces. Top: Blue line represents calcium signal and the corresponding deconvoluted spiking activity is plotted by the red line. Bottom: the magnified calcium signals in the black box. **E-H**. 3xTg-AD CA1 cells exhibit less place-specific firing properties compared to Non-Tg CA1 cells during open field exploration. E. Calcium response and combined spatial rate map from a young age Non-Tg mouse. Left: Denoised calcium signal of one neuron. Middle: travel trajectory in the circular arena is plotted by black line. Red dots represent the locations in which the spike events are higher than threshold. Right: Rate maps of fluorescence firing rate. The arena is divided into 10 X 10mm bins and each bin's firing rate is calculated as the total number of spikes divided by the total time mice spend inside the bin. The rate map is smoothed with 100 X 100mm gaussian kernel (standard deviation = 20mm). F, G, H are arranged in the same format for old-age Non-Tg, young-age 3xAD-Tg and old-age 3xAD-Tg mice.

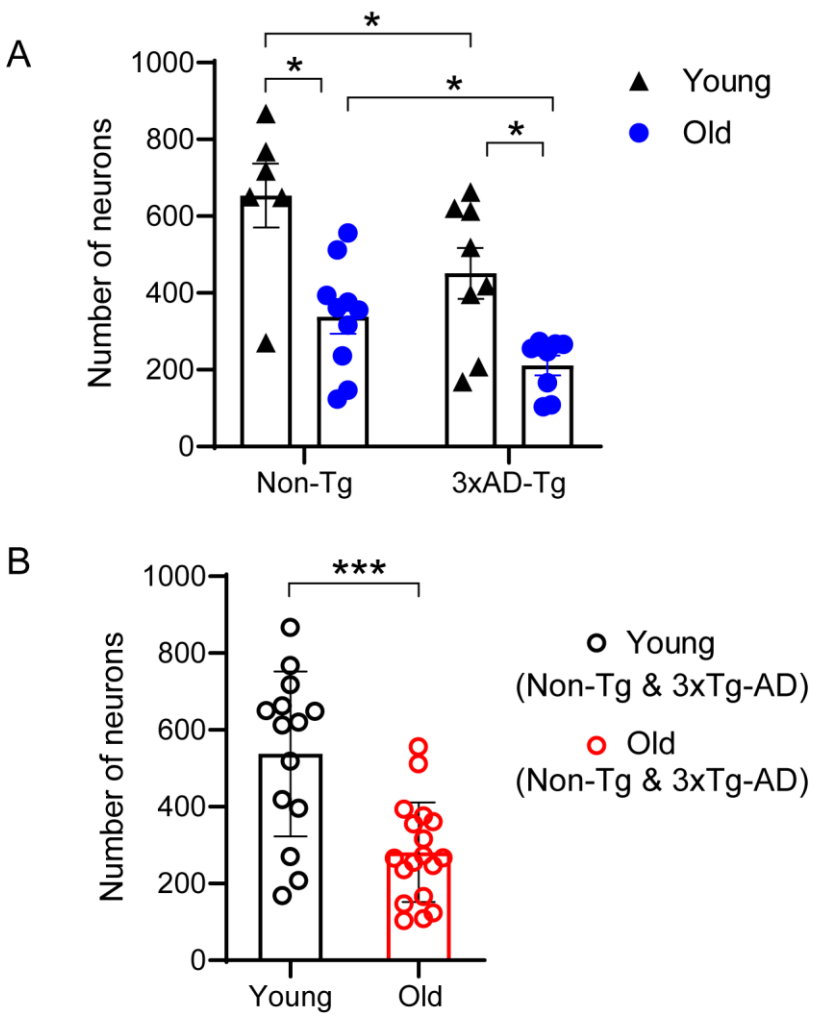

Figure 2.3 Comparative analyses of the numbers of active hippocampal CA1 neurons across age and AD groups using imaging trials during open field exploration A. Comparative quantification of Extended Constrained Nonnegative Matrix Factorization (CNMF-E) extracted neurons for the young and old 3xTg-AD and control Non-Tg mice. The average total numbers of neurons are 653.7 ± 83.7 cells for young Non-Tg mice (N = 6), 337.7 ± 44.3 cells for old Non-Tg mice (N = 10), 450.9 ± 66.4 cells for young 3xTg-AD mice (N = 8), and 211 ± 25.8 cells for old 3xTg-AD mice (N = 8). Each triangle or circle represent a data point from one mouse. All data are presented as mean ± s.e.m.; * indicates the statistical significance level of $p \leq 0.05$ (Mann-Whitney U test). A significant difference was found between the Non-Tg young and old groups ($p = 0.0207$), between young and old 3xTg mice ($p = 0.0110$), between young Non-Tg and 3xTg-AD ($p=0.0426$), and between old Non-Tg and 3xTg-AD ($p=0.0434$) **B.** Comparative quantification of CNMF-E extracted neurons for combined young and old groups (pooling Non-Tg and 3xTg-AD mice) to test age effects. The total number of neurons is on average 520.1 ± 57.3 cells for young Non-Tg and 3xTg-AD mice (N = 15), 312.2 ± 11.2 cells for old Non-Tg and 3xTg-AD mice (N = 18). A significant difference was found between age groups ($p = 0.0006$, Mann-Whitney U test). *** indicates the statistical significance level of $p \leq 0.001$.

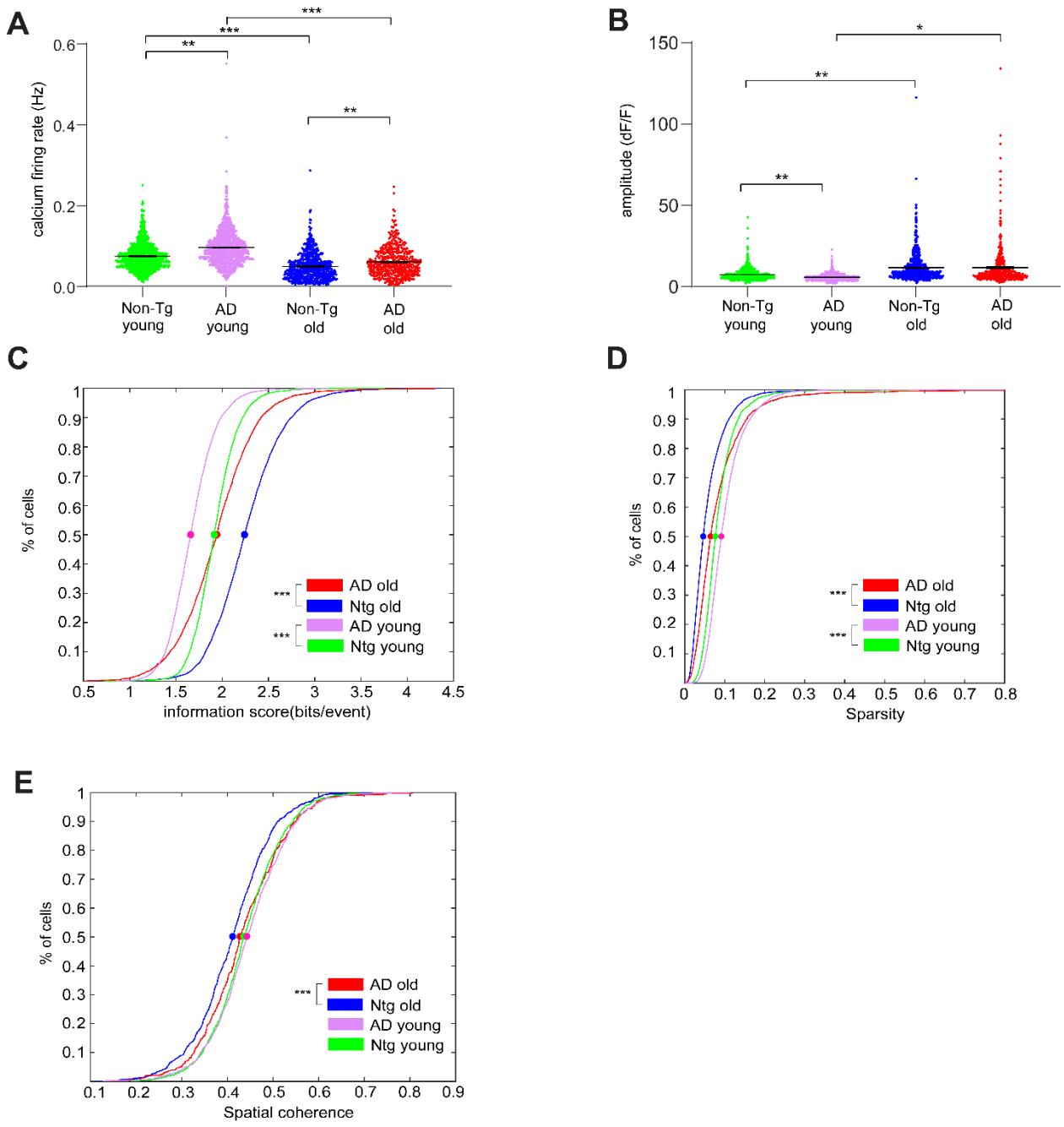

Figure 2.4. Hippocampal CA1 cells in 3xTg-AD mice exhibit altered calcium activities and impaired spatial coding during open field exploration A. Temporal firing rate of all neurons from the 4 types of mice. Only the periods with traversal speed higher than 5mm/sec are used for firing rate calculation, and firing rates from trials with the same geometry are averaged. Overall, neurons from 3xTg-AD mice have higher firing rate than those from Non-Tg mice, and young mice have higher firing rate than old mice (Non-Tg young: 0.0752 ± 0.0010 Hz (1180 cells from 5 mice), AD young: 0.0965 ± 0.0013 Hz (1076 cells from 8 mice), Non-Tg old: 0.0497 ± 0.0012 Hz (716 cells from 9 mice), AD old: 0.0612 ± 0.0018 Hz (430 cells from 8 mice). Ntg young vs AD young, LME: p = 0.0091; Ntg old vs AD old, LME: p = 0.0094; Non-Tg young vs Non-Tg

old, LME: $p = 3.8744 \times 10^{-5}$; AD young vs AD old, LME: $p=1.5095 \times 10^{-5}$). **B**. Averaged calcium spike amplitude of all neurons from the 4 types of mice. Only the periods with traversal speed higher than 5mm/sec are used for amplitude calculation, and amplitude values from trials with the same geometry are averaged. Overall, the amplitude values of young AD mice are significantly higher than those of young Non-Tg mice, while between old AD and Non-Tg mice there's no significant difference. The amplitude of young mice is significantly lower than old mice for both genotypes (Non-Tg young: 7.386 ± 0.100 in the unit of dF/F (1180 cells from 5 mice); AD young: 5.725 ± 0.064 dF/F (1076 cells from 8 mice), Non-Tg old: 11.680 ± 0.322 dF/F (716 cells from 9 mice), AD old: 11.700 ± 0.619 dF/F (430 cells from 8 mice). Non-Tg young vs AD young, LME: p=0.0066, Non-Tg old vs AD old, LME: p=0.6388, Non-Tg young vs Non-Tg old: LME, p=0.0055, AD young vs AD old, LME: p=0.0287). **C**. Cumulative distribution of spatial information scores (in bits/event) for all place cells from Non-Tg old, AD old, Non-Tg young and AD young mice exploring in both square and circle arenas. Only the periods with traversal speed higher than 5mm/sec are used for calculation. Overall Non-Tg mice have a higher information score than AD mice for both ages. Old AD mice display higher score values than younger AD ones (the respective 50%-cumulative values for Non-Tg young (233 place cells from 5 mice), AD young (214 place cells from 8 mice), Non-Tg old (104 place cells from 9 mice) and AD old (131 place cells from 8 mice) are 1.9136 1.6586, 2.2410, and 1.9409. Non-Tg young vs AD young: $p = 4.1683 \times 10^{-12}$. Non-Tg old vs AD old: p = 0.0008, Non-Tg young vs Non-Tg old: $p = 1.1583 \times 10^{-8}$, AD young vs AD old: $p = 1.1370 \times 10^{-6}$, two-sample Kolmogorov-Smirnov test). **D.** Cumulative distribution plots of sparsity of all neurons for all Non-Tg old, AD old, Non-Tg young and AD young mice, in both square and circle arena. Overall AD mice have higher sparsity than Non-Tg mice. Meanwhile, young mice show higher sparsity than old mice (the respective 50%-cumulative values for Non-Tg young (1180 cells from 5 mice), AD young (1076 cells from 8 mice), Non-Tg old (716 cells from 9 mice) and AD old (430 cells from 8 mice) are 0.0746, 0.0957, 0.0492 and 0.0657. Non-Tg young vs AD young: $p = 1.2703 \times 10^{-31}$, Non-Tg old vs AD old: $p= 2.0458 \times 10^{-7}$, Non-Tg young vs Non-Tg old: $p = 9.0277 \times 10^{-42}$, AD young vs AD old: $p = 1.0343 \times 10^{-25}$, two-sample Kolmogorov-Smirnov test) **E.** Cumulative distribution plots of spatial coherence of all neurons for all Non-Tg old, AD old, Non-Tg young and AD young mice, in both square and circle arena. Old AD mice have higher spatial coherence than old Non-Tg mice, while no significant difference is noted between genotypes of young mice. Meanwhile, young mice show higher coherence values than old mice (the respective 50%-cumulative- values for Non-Tg young (1180 cells from 5 mice), AD young (1076 cells from 8 mice), Non-Tg old (716 cells from 9 mice), and AD old (430 cells from 8 mice): 0.4369, 0.4437, 0.4053 and 0.4286. Non-Tg young vs AD young: p = 0.0728, Non-Tg old vs AD old: $p= 5.4990 \times 10^{-4}$, Non-Tg young vs Non-Tg old: $p = 2.3031 \times 10^{-6}$, AD young vs AD old: p=0.0177, two-sample Kolmogorov-Smirnov test)

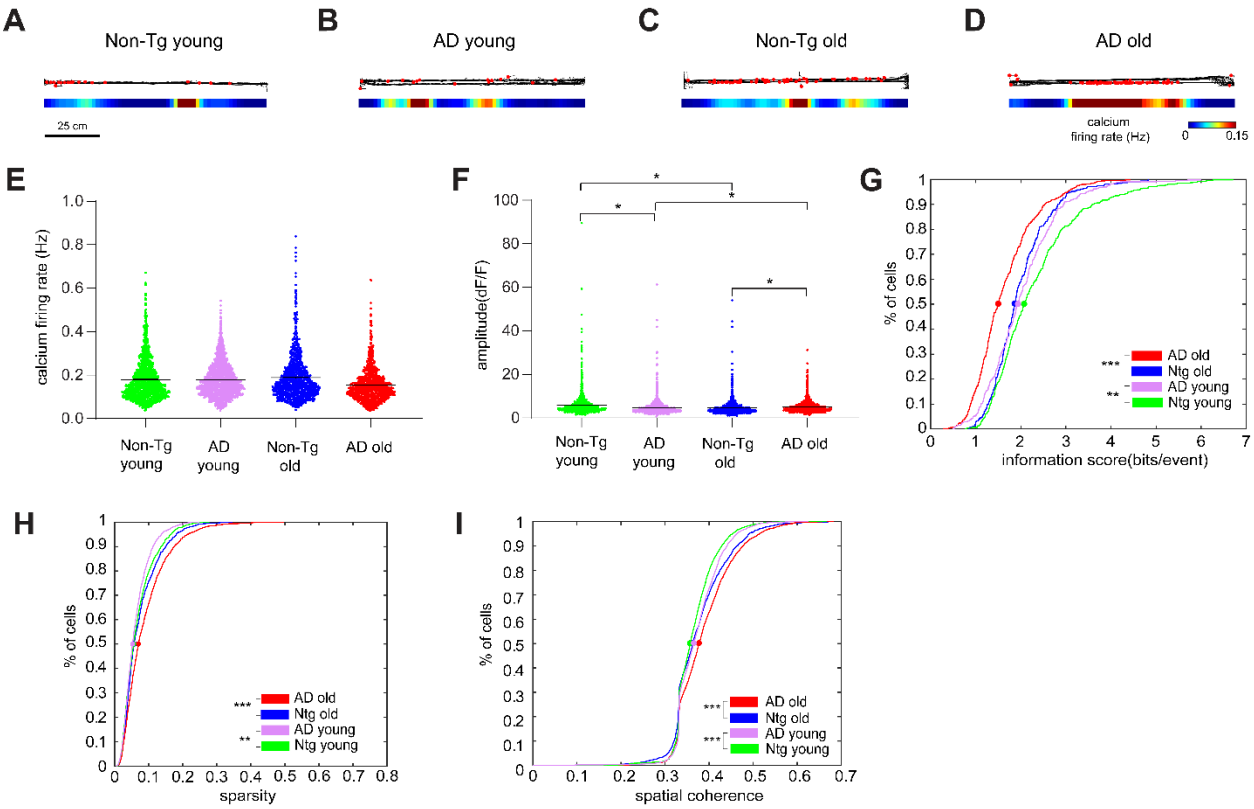

Figure 2.5. Linear track experiment data also supports impaired spatial coding in 3xTg AD hippocampal CA1 A-D. Response of typical neurons in horizontal linear track of mice with different genotypes and ages. Top: black line represents the trajectory of mice. Red dots on top represent sites where beyond threshold calcium events occur. Bottom: smoothed spatial ratemaps. **E**. Temporal firing rate of all neurons from the 4 types of mice. Only the periods with traversal speed higher than 5mm/sec are used for firing rate calculation, and firing rates from trials with the same track direction are averaged. Overall, no significance is noted between ages and genotypes (Non-Tg young (1742 cells from 6 mice): 0.1795 ± 0.0023 Hz; AD young (1988 cells from 8 mice): 0.1762 ± 0.0018 Hz; Non-Tg old (1136 cells from 5 mice): 0.1880 ± 0.0031 Hz; AD old (1560 cells from 5 mice): 0.1603 ± 0.0022 Hz. Non-Tg young vs AD young: LME: p=0.8752, Non-Tg old vs AD old: LME: p=0.1875, Non-Tg young vs Non-Tg old: LME: p=0.8974, AD young vs AD old: LME: p=0.2324). **F.** Averaged calcium spike amplitude of all neurons from the 4 types of mice. Only the periods with traversal speed higher than 5mm/sec are used for amplitude calculation, and amplitude values from trials with the same geometry are averaged. Overall, the amplitude values of AD mice are significantly higher than those of Non-Tg mice, and the amplitude of young mice is significantly lower than old mice for both genotypes (Non-Tg young (1742 cells from 6 mice): 5.745 ± 0.112 dF/F; AD young (1988 cells from 8 mice): 4.534 ± 0.076 dF/F; Non-Tg old (1136 cells from 5 mice): 4.573 ± 0.107 dF/F; AD old (1560 cells from 5 mice): 5.064 ± 0.079 dF/F. Non-Tg young vs AD young, LME: p = 0.0167; Non-Tg old vs AD old, LME: p=0.0495; Non-Tg young vs Non-Tg old, LME: p = 0.0132; AD young vs AD old, LME: p = 0.0354). **G**. Cumulative distribution plots of spatial information score (in bits/event) for all place cells from Non-Tg old, AD old, Non-Tg young and AD young mice, for both horizontal and

vertical tracks and two directions. Overall Non-Tg mice have higher score values than AD mice for both ages, and young mice have higher score values than old mice (the respective 50%-cumulative values for Non-Tg young (238 place cells in direction 1 + 246 place cells in direction 2, from 6 mice), AD young (213 place cells in direction 1 + 237 place cells in direction 2, from 8 mice), Non-Tg old (163 place cells in direction 1 + 159 place cells in direction 2, from 5 mice) and AD old are (259 place cells in direction 1 + 272 place cells in direction 2, from 5 mice) are 2.0727, 1.9371, 1.8581 and 1.4978. Non-Tg young vs AD young: p=0.0432, Non-Tg old vs AD old: p= 0.0010, Non-Tg young vs Non-Tg old: p= $8.7241*10^{-7}$, AD young vs AD old: p=$3.4423*10^{-5}$, two-sample Kolmogorov-Smirnov test). **H.** sparsity of all neurons for all Non-Tg old, AD old, Non-Tg young and AD young mice, in both square and circle arena. Old AD mice have higher sparsity than Non-Tg mice, while young 3xTg-AD mice show lower sparsity than Non-Tg mice. Meanwhile, 3xTg-AD old mice show higher sparsity than young mice (the respective 50%-cumulative values for Non-Tg young (1742 cells (each direction) from 6 mice), AD young (1988 cells (each direction) from 8 mice), Non-Tg old (1136 cells (each direction) from 5 mice) and AD old (1560 cells (each direction) from 6 mice) are 0.0490, 0.0429, 0.0499, and 0.0559. Non-Tg young vs AD young: p= 1.2231×10^{-9}, Non-Tg old vs AD old: p= 1.7939×10^{-5}, Non-Tg young vs Non-Tg old: p = 0.0818; AD young vs AD old: p = 3.4707×10^{-31}, two-sample Kolmogorov-Smirnov test). **I.** Cumulative distribution plots of spatial coherence of all neurons for all Non-Tg old, AD old, Non-Tg young and AD young mice, in both square and circle arena. AD mice have higher spatial coherence than Non-Tg mice at both ages, meanwhile, young mice shows higher coherence values than old mice (the respective 50%-cumulative values for Non-Tg young (1742 cells (each direction) from 6 mice), AD young (1988 cells (each direction) from 8 mice), Non-Tg old (1136 cells (each direction) from 5 mice) and , AD old (1560 cells (each direction) from 6 mice) are 0.3573, 0.3658, 0.3632 and 0.3778. Non-Tg young vs AD young: p = 8.8051×10^{-10}, Non-Tg old vs AD old: p= 2.7640×10^{-11}, Non-Tg young vs Non-Tg old: p=7.9276×10^{-12}, AD young vs AD old: p=$2.7437*10^{-17}$, two-sample Kolmogorov-Smirnov test)

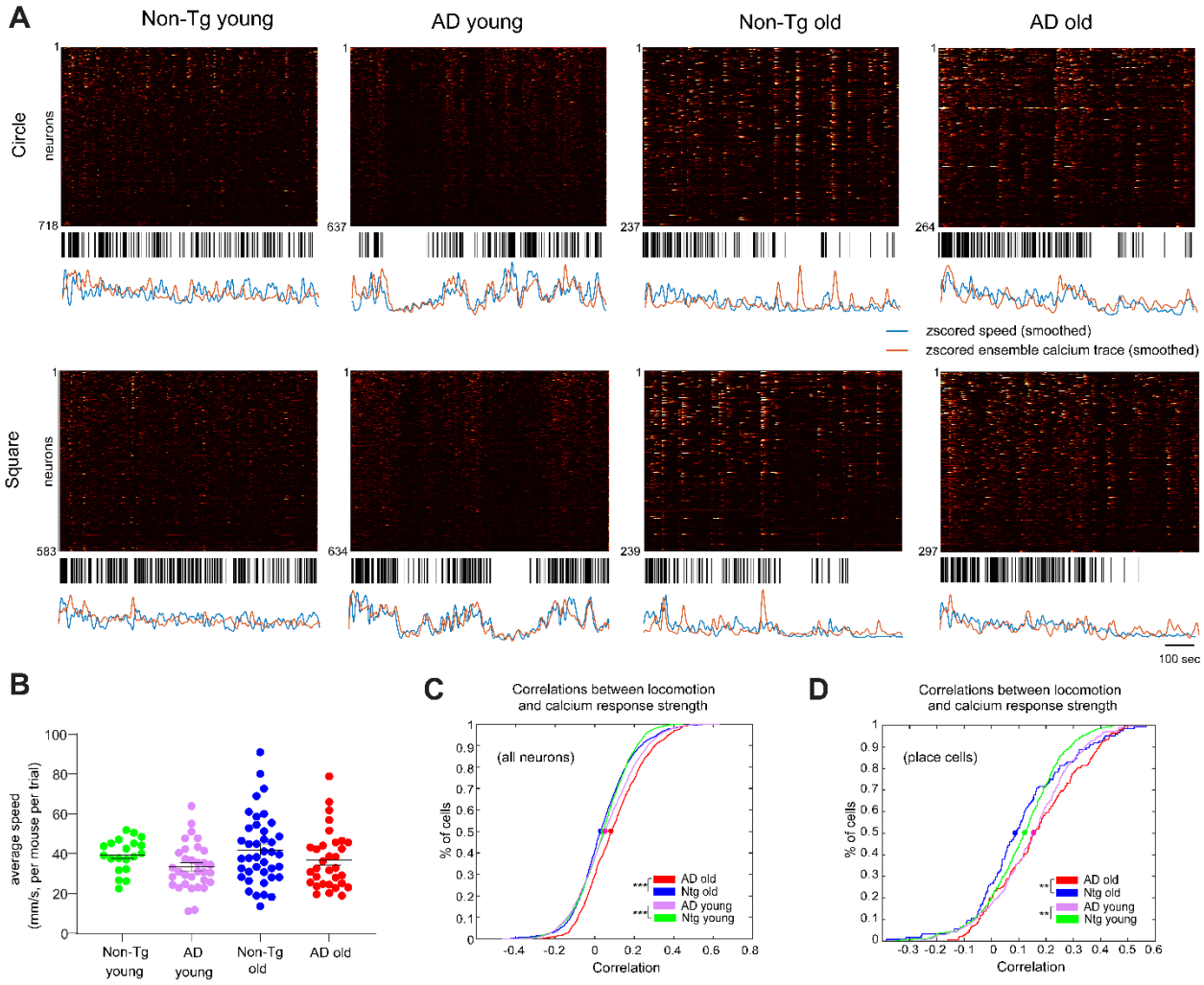

Figure 2.6. Neural calcium activities of 3xAD-Tg mice exhibit stronger locomotion modulation than Non-Tg mice A. Raster plots of calcium activities of hundreds of CA1 cells along with the time (top), movement epochs (middle) and comparison between the z-scored ensemble calcium signal trace and movement speed (bottom, ensemble calcium trace: orange; velocity trace: blue). The high-speed epoch is shown as the black bar at the time points where the movement speed is higher than the speed threshold, which is defined as the averaged median movement speed of the group. Four example sessions of Non-Tg young, 3xTg-AD young, Non-Tg old, and 3xTg-AD old mice, respectively, are shown. **B.** Distribution of mean movement speeds of different groups of mice. Each dot represents the mean speed of one mouse in one trial (circle or square). **C.** Cumulative distribution plots of correlation values between moving speed and all individual neuron's calcium response. Correlation values from trials with the same geometry are averaged. **D.** Cumulative distribution plots of correlation values between moving speed and all place cells' calcium trace. Two-sample Kolmogorov-Smirnov tests were used for C-D. *, ** and *** indicate the significance levels with the respective p values of <0.05, <0.001, and < 0.0001. (For interpretation of the references to colour in this figure legend, the reader is referred to the web version of this article.)

References

2020 Alzheimer's disease facts and figures. (2020). *Alzheimers Dement*. https://doi.org/10.1002/alz.12068

Allison, S. L., Fagan, A. M., Morris, J. C., & Head, D. (2016). Spatial Navigation in Preclinical Alzheimer's Disease. *J Alzheimers Dis*, *52*(1), 77-90. https://doi.org/10.3233/JAD-150855

Arriaga, M., & Han, E. B. (2017). Dedicated Hippocampal Inhibitory Networks for Locomotion and Immobility. *J Neurosci*, *37*(38), 9222-9238. https://doi.org/10.1523/JNEUROSCI.1076-17.2017

Arriaga, M., & Han, E. B. (2017). Dedicated Hippocampal Inhibitory Networks for Locomotion and Immobility. *The Journal of Neuroscience*, *37*(38), 9222. https://doi.org/10.1523/JNEUROSCI.1076-17.2017

Baglietto-Vargas, D., Prieto, G. A., Limon, A., Forner, S., Rodriguez-Ortiz, C. J., Ikemura, K., Ager, R. R., Medeiros, R., Trujillo-Estrada, L., Martini, A. C., Kitazawa, M., Davila, J. C., Cotman, C. W., Gutierrez, A., & LaFerla, F. M. (2018). Impaired AMPA signaling and cytoskeletal alterations induce early synaptic dysfunction in a mouse model of Alzheimer's disease. *Aging Cell*, *17*(4), e12791. https://doi.org/10.1111/acel.12791

Belfiore, R., Rodin, A., Ferreira, E., Velazquez, R., Branca, C., Caccamo, A., & Oddo, S. (2019). Temporal and regional progression of Alzheimer's disease-like pathology in 3xTg-AD mice. *Aging Cell*, *18*(1), e12873. https://doi.org/10.1111/acel.12873

Billings, L. M., Oddo, S., Green, K. N., McGaugh, J. L., & LaFerla, F. M. (2005). Intraneuronal Abeta causes the onset of early Alzheimer's disease-related cognitive deficits in transgenic mice. *Neuron*, *45*(5), 675-688. https://doi.org/10.1016/j.neuron.2005.01.040

Busche, M. A., Chen, X., Henning, H. A., Reichwald, J., Staufenbiel, M., Sakmann, B., & Konnerth, A. (2012). Critical role of soluble amyloid-beta for early hippocampal hyperactivity in a mouse model of Alzheimer's disease. *Proc Natl Acad Sci U S A*, *109*(22), 8740-8745. https://doi.org/10.1073/pnas.1206171109

Busche, M. A., & Konnerth, A. (2016). Impairments of neural circuit function in Alzheimer's disease. *Philos Trans R Soc Lond B Biol Sci*, *371*(1700). https://doi.org/10.1098/rstb.2015.0429

Cai, D. J., Aharoni, D., Shuman, T., Shobe, J., Biane, J., Song, W., Wei, B., Veshkini, M., La-Vu, M., Lou, J., Flores, S. E., Kim, I., Sano, Y., Zhou, M., Baumgaertel, K., Lavi, A., Kamata, M., Tuszynski, M., Mayford, M., . . . Silva, A. J. (2016). A shared neural ensemble links distinct contextual memories encoded close in time. *Nature*, *534*(7605), 115-118. https://doi.org/10.1038/nature17955

Canter, R. G., Penney, J., & Tsai, L.-H. (2016). The road to restoring neural circuits for the treatment of Alzheimer's disease. *Nature*, *539*(7628), 187-196. https://doi.org/10.1038/nature20412

Chen, T. W., Wardill, T. J., Sun, Y., Pulver, S. R., Renninger, S. L., Baohan, A., Schreiter, E. R., Kerr, R. A., Orger, M. B., Jayaraman, V., Looger, L. L., Svoboda, K., & Kim, D. S. (2013). Ultrasensitive fluorescent proteins for imaging neuronal activity. *Nature*, *499*(7458), 295-300. https://doi.org/10.1038/nature12354

Coughlan, G., Laczo, J., Hort, J., Minihane, A. M., & Hornberger, M. (2018). Spatial navigation deficits - overlooked cognitive marker for preclinical Alzheimer disease? *Nat Rev Neurol*, *14*(8), 496-506. https://doi.org/10.1038/s41582-018-0031-x

De Strooper, B., & Karran, E. (2016). The Cellular Phase of Alzheimer's Disease. *Cell*, *164*(4), 603-615. https://doi.org/10.1016/j.cell.2015.12.056

Frere, S., & Slutsky, I. (2018). Alzheimer's Disease: From Firing Instability to Homeostasis Network Collapse. *Neuron*, *97*(1), 32-58. https://doi.org/10.1016/j.neuron.2017.11.028

Friedrich, J., Zhou, P., & Paninski, L. (2017). Fast online deconvolution of calcium imaging data. *PLoS Comput Biol*, *13*(3), e1005423. https://doi.org/10.1371/journal.pcbi.1005423

Fuhrmann, F., Justus, D., Sosulina, L., Kaneko, H., Beutel, T., Friedrichs, D., Schoch, S., Schwarz, M. K., Fuhrmann, M., & Remy, S. (2015). Locomotion, Theta Oscillations, and the Speed-Correlated Firing of Hippocampal Neurons Are Controlled by a Medial Septal Glutamatergic Circuit. *Neuron*, *86*(5), 1253-1264. https://doi.org/10.1016/j.neuron.2015.05.001

Góis, Z. H. T. D., & Tort, A. B. L. (2018). Characterizing Speed Cells in the Rat Hippocampus. *Cell Reports*, *25*(7), 1872-1884.e1874. https://doi.org/https://doi.org/10.1016/j.celrep.2018.10.054

Grieco, S. F., Holmes, T. C., & Xu, X. (2023). Probing neural circuit mechanisms in Alzheimer's disease using novel technologies. *Molecular Psychiatry*. https://doi.org/10.1038/s41380-023-02018-x

Grieco, S. F., Qiao, X., Johnston, K. G., Chen, L., Nelson, R. R., Lai, C., Holmes, T. C., & Xu, X. (2021). Neuregulin signaling mediates the acute and sustained antidepressant effects of subanesthetic ketamine. *Transl Psychiatry*, *11*(1), 144. https://doi.org/10.1038/s41398-021-01255-4

Grieco, S. F., Qiao, X., Zheng, X., Liu, Y., Chen, L., Zhang, H., Yu, Z., Gavornik, J. P., Lai, C., Gandhi, S. P., Holmes, T. C., & Xu, X. (2020). Subanesthetic Ketamine Reactivates Adult Cortical Plasticity to Restore Vision from Amblyopia. *Curr Biol*, *30*(18), 3591-3603 e3598. https://doi.org/10.1016/j.cub.2020.07.008

Harris, S. S., Wolf, F., De Strooper, B., & Busche, M. A. (2020). Tipping the Scales: Peptide-Dependent Dysregulation of Neural Circuit Dynamics in Alzheimer's Disease. *Neuron*, *107*(3), 417-435. https://doi.org/10.1016/j.neuron.2020.06.005

Indersmitten, T., Schachter, M. J., Young, S., Welty, N., Otte, S., Nassi, J. J., Lovenberg, T., Bonaventure, P., & Wyatt, R. M. (2019). In vivo Calcium Imaging Reveals That Cortisol Treatment Reduces the Number of Place Cells in Thy1-GCaMP6f Transgenic Mice. *Frontiers in Neuroscience*, *13*. https://doi.org/Artn 176

10.3389/Fnins.2019.00176

Jun, H., Bramian, A., Soma, S., Saito, T., Saido, T. C., & Igarashi, K. M. (2020). Disrupted Place Cell Remapping and Impaired Grid Cells in a Knockin Model of Alzheimer's Disease. *Neuron*, *107*(6), 1095-1112 e1096. https://doi.org/10.1016/j.neuron.2020.06.023

Jun, H., Bramian, A., Soma, S., Saito, T., Saido, T. C., & Igarashi, K. M. (2020). Disrupted Place Cell Remapping and Impaired Grid Cells in a Knockin Model of Alzheimer's Disease. *Neuron*, *107*(6), 1095-1112.e1096. https://doi.org/https://doi.org/10.1016/j.neuron.2020.06.023

Jung, M. W., Wiener, S. I., & McNaughton, B. L. (1994). Comparison of spatial firing characteristics of units in dorsal and ventral hippocampus of the rat. *J Neurosci*, *14*(12), 7347-7356. https://www.ncbi.nlm.nih.gov/pubmed/7996180

Laird, N. M., & Ware, J. H. (1982). Random-effects models for longitudinal data. *Biometrics*, *38*(4), 963-974. http://www.ncbi.nlm.nih.gov/pubmed/7168798

Lerdkrai, C., Asavapanumas, N., Brawek, B., Kovalchuk, Y., Mojtahedi, N., Olmedillas Del Moral, M., & Garaschuk, O. (2018). Intracellular Ca(2+) stores control in vivo neuronal

hyperactivity in a mouse model of Alzheimer's disease. *Proc Natl Acad Sci U S A*, *115*(6), E1279-E1288. https://doi.org/10.1073/pnas.1714409115

Mclean, R. A., Sanders, W. L., & Stroup, W. W. (1991). A Unified Approach to Mixed Linear-Models. *American Statistician*, *45*(1), 54-64. https://doi.org/Doi 10.2307/2685241

Mesulam, M. M. (2000). A plasticity-based theory of the pathogenesis of Alzheimer's disease. *Ann N Y Acad Sci*, *924*, 42-52. https://doi.org/10.1111/j.1749-6632.2000.tb05559.x

Oddo, S., Caccamo, A., Shepherd, J. D., Murphy, M. P., Golde, T. E., Kayed, R., Metherate, R., Mattson, M. P., Akbari, Y., & LaFerla, F. M. (2003). Triple-transgenic model of Alzheimer's disease with plaques and tangles: intracellular Abeta and synaptic dysfunction. *Neuron*, *39*(3), 409-421. https://doi.org/10.1016/s0896-6273(03)00434-3

Pnevmatikakis, E. A., & Giovannucci, A. (2017). NoRMCorre: An online algorithm for piecewise rigid motion correction of calcium imaging data. *J Neurosci Methods*, *291*, 83-94. https://doi.org/10.1016/j.jneumeth.2017.07.031

Scheyltjens, I., Laramee, M. E., Van den Haute, C., Gijsbers, R., Debyser, Z., Baekelandt, V., Vreysen, S., & Arckens, L. (2015). Evaluation of the expression pattern of rAAV2/1, 2/5, 2/7, 2/8, and 2/9 serotypes with different promoters in the mouse visual cortex. *J Comp Neurol*, *523*(14), 2019-2042. https://doi.org/10.1002/cne.23819

Skaggs, W. E., McNaughton, B. L., Wilson, M. A., & Barnes, C. A. (1996). Theta phase precession in hippocampal neuronal populations and the compression of temporal sequences. *Hippocampus*, *6*(2), 149-172. https://doi.org/10.1002/(SICI)1098-1063(1996)6:2<149::AID-HIPO6>3.0.CO;2-K

Stimmell, A. C., Baglietto-Vargas, D., Moseley, S. C., Lapointe, V., Thompson, L. M., LaFerla, F. M., McNaughton, B. L., & Wilber, A. A. (2019). Impaired Spatial Reorientation in the 3xTg-AD Mouse Model of Alzheimer's Disease. *Sci Rep*, *9*(1), 1311. https://doi.org/10.1038/s41598-018-37151-z

Stobart, J. L., Ferrari, K. D., Barrett, M. J. P., Stobart, M. J., Looser, Z. J., Saab, A. S., & Weber, B. (2018). Long-term In Vivo Calcium Imaging of Astrocytes Reveals Distinct Cellular Compartment Responses to Sensory Stimulation. *Cerebral Cortex*, *28*(1), 184-198. https://doi.org/10.1093/cercor/bhw366

Sun, Y., Jin, S., Lin, X., Chen, L., Qiao, X., Jiang, L., Zhou, P., Johnston, K. G., Golshani, P., Nie, Q., Holmes, T. C., Nitz, D. A., & Xu, X. (2019). CA1-projecting subiculum neurons facilitate object-place learning. *Nat Neurosci*, *22*(11), 1857-1870. https://doi.org/10.1038/s41593-019-0496-y

Venneri, A., Mitolo, M., Beltrachini, L., Varma, S., Della Pieta, C., Jahn-Carta, C., Frangi, A. F., & De Marco, M. (2019). Beyond episodic memory: Semantic processing as independent predictor of hippocampal/perirhinal volume in aging and mild cognitive impairment due to Alzheimer's disease. *Neuropsychology*, *33*(4), 523-533. https://doi.org/10.1037/neu0000534

Weller, J., & Budson, A. (2018). Current understanding of Alzheimer's disease diagnosis and treatment. *F1000Res*, *7*. https://doi.org/10.12688/f1000research.14506.1

Wong, J. C., Grieco, S. F., Dutt, K., Chen, L., Thelin, J. T., Inglis, G. A. S., Parvin, S., Garraway, S. M., Xu, X., Goldin, A. L., & Escayg, A. (2021). Autistic-like behavior, spontaneous seizures, and increased neuronal excitability in a Scn8a mouse model. *Neuropsychopharmacology*. https://doi.org/10.1038/s41386-021-00985-9

Zhang, S., Schonfeld, F., Wiskott, L., & Manahan-Vaughan, D. (2014). Spatial representations of place cells in darkness are supported by path integration and border information. *Front Behav Neurosci*, *8*, 222. https://doi.org/10.3389/fnbeh.2014.00222

Zhou, P., Resendez, S. L., Rodriguez-Romaguera, J., Jimenez, J. C., Neufeld, S. Q., Giovannucci, A., Friedrich, J., Pnevmatikakis, E. A., Stuber, G. D., Hen, R., Kheirbek, M. A., Sabatini, B. L., Kass, R. E., & Paninski, L. (2018). Efficient and accurate extraction of in vivo calcium signals from microendoscopic video data. *Elife*, *7*. https://doi.org/10.7554/eLife.28728

Zhou, P., Resendez, S. L., Rodriguez-Romaguera, J., Jimenez, J. C., Neufeld, S. Q., Giovannucci, A., Friedrich, J., Pnevmatikakis, E. A., Stuber, G. D., Hen, R., Kheirbek, M. A., Sabatini, B. L., Kass, R. E., & Paninski, L. (2018). Efficient and accurate extraction of in vivo calcium signals from microendoscopic video data. *eLife*, *7*, e28728. https://doi.org/10.7554/eLife.28728

Ziv, Y., Burns, L. D., Cocker, E. D., Hamel, E. O., Ghosh, K. K., Kitch, L. J., El Gamal, A., & Schnitzer, M. J. (2013). Long-term dynamics of CA1 hippocampal place codes. *Nat Neurosci*, *16*(3), 264-266. https://doi.org/10.1038/nn.3329

Chapter 3: Impact of Alzheimer's disease and aging on the anatomical organization of temporally correlated CA1 pyramidal neurons

Abstract

Alzheimer's disease is known for damaging the circuit connectivity and neuron function along the entorhinal-hippocampal circuit. Recently we discovered temporally correlated CA1 pyramidal neurons could formulate anatomically compact clusters that occupy segregated regions under the imaging field of view, but how Alzheimer's disease at different stages could impact this kind of organization is still not known. Here we re-analyzed a dataset of a published work in 2023 containing in vivo miniscope calcium imaging on the CA1 pyramidal cell populations in 5xFAD mice and wildtype controls performing linear track running task, at three different ages (4-5 month, 8-10 month, and 14 month). We identified subpopulations of temporally correlated CA1 pyramidal cell in both wild type and 5xFAD mice that lie in segregated anatomical clusters as reported in our previous research, while the intra-cluster pairwise correlation, as well as the size of anatomical clusters, did not show significant difference across ages and genotypes. Ensemble activities between different clusters of young AD mice have higher level of overlap compared to corresponding wild type, but the effect is not shown in other ages. When rotate track by 90 degrees in the same environment, anatomical cluster similarity between the different direction tracks was significantly lower than that between two tracks in the same direction, however this phenomenon only appears at the 8-10 month age, and no significant difference noted between wild type and 5xFAD mice. Lastly, we defined the mosaic index, which represent the segregation level of the anatomical clusters, and find that the index is negatively correlated with overall pairwise correlation strength of the whole CA1 pyramidal cell population, except old AD mice. Overall, this preliminary study examines key features of the temporal-anatomical CA1 pyramidal neurons clusters discovered in Chapter 1 under AD condition across different age groups, and find these features are largely similar between wildtype and AD condition

Introduction

Individual hippocampal CA1 pyramidal neurons can represent variables related to the environment and experience of the animals (Eichenbaum, 2014; Gauthier & Tank, 2018; O'Keefe & Dostrovsky, 1971). At the same time, ensembles of pyramidal neurons can display collective, synchronized activation within a short time window (Buzsáki, 2010; Harris et al., 2003). The synchronized activation increases the temporal correlations between neurons inside the co-active subgroup, while between two neurons not exhibiting co-activation, their correlation will be low, which created a patterned pairwise correlation structure within the whole pyramidal neuron population. In recent years, this temporal-based structure has been proposed to represent an internal cognitive map that contains animal's innate understanding of the environment (Buzsáki, 2019; Kubie et al., 2020). In the meantime, recent studies have proposed that temporally correlated CA1 pyramidal neurons may display patterned distribution in anatomical space (Dombeck et al., 2010; Geiller et al., 2022; Modi et al., 2014). Our results in Chapter 1 have supported the hypothesis by illustrating the CA1 pyramidal neurons subgroups with relatively high pairwise correlation can organize into segregated anatomical spaces. These neural clusters may represent hippocampal micro-circuits that support and guide the pyramidal cells ensemble activity patterns.

Alzheimer's Disease (AD) has a profound impact on the CA1 pyramidal neurons. The accumulation of Aβ plaque has been found to have toxicity toward pyramidal neurons, lead to hyperactivity in the early stage of the disease, and hypoactivity in the later stage (Busche et al., 2012; Grieco et al., 2023), which may add randomness to the neurons' activation pattern and impact the correlation structure. Meanwhile, loss of synaptic connectivity and interneurons may lead to less coordinated firing patterns among the pyramidal cell subgroups (Kuchibhotla et al., 2008; Kurudenkandy et al., 2014; Neuman et al., 2015; Palop & Mucke, 2016). However, the

actual impact of AD on the CA1 pyramidal neurons ensemble activation pattern also depends on the age and disease stages (Grienberger et al., 2012; Jun et al., 2020). For example, in APP-KI mice it has been found that at around 3 month age, although Aβ plaque already appears in CA1, the global remapping ability of pyramidal neuron populations is not affected between different environments, and the remapping impairment only appears at ~13 month age (Jun et al., 2020). The temporal-anatomical CA1 neuron clusters described in Chapter 1 could also be subjected to the age and disease stage specific dysregulation of AD. But till now, few studies have been performed to address this hypothesis.

In the present work, we investigated the questions above by examining the temporal dynamics of CA1 pyramidal neuron populations using in vivo calcium imaging with miniature head-mounted microscopes ("miniscopes") for both wild type and 5xFAD mice across different ages (4-5 month, 8-10 month, and 14 month), during a linear track traverse experiment. Specially, we examined how the organizations we described in Chapter 1 will be different across genotypes and ages. Interestingly, we didn't find significant difference for both intra-temporal cluster correlation, and anatomical size, between wild type and 5xFAD mice and across ages. Between two trials with same or different direction tracks, the pairwise correlation pattern, as well as anatomical cluster similarity, only showing significant reduction of similarity at middle age (8-10 month). Lastly, the segregation level of anatomical clusters, measured by the mosaic level metric, exhibit significant negative correlation toward the intra-cluster temporal correlation level for young WT, middle-aged WT and young AD, but no significant correlation with rate map correlation, which reflect that the anatomical organizations' relationship with functional connectivity rather than spatial coding.

Methods

Animals

This study re-analyzed data from a previous published study (Zhang et al., 2023). In the study, 5xFAD mice and wild type (WT) mice were obtained from the Model Organism Development and Evaluation for Late-onset Alzheimer's Disease (MODEL-AD) center at the University of California, Irvine. Mice were housed in a controlled environment with temperature maintained at 21–23 °C and humidity at 40% - 70%. Mice had free access to diet but had water restrictions during linear track test. Young age means 4-5 months old mice, middle-age means 8-10 months old mice, and old age means 14 months old mice. Both male and female mice were included and were pooled together for analysis. All the experimental protocols were approved by the IACUC of the University of California, Irvine and carried out in accordance with the Guide for the Care and Use of Laboratory Animals of the US National Institutes of Health.

Virus injection

Surgery was performed as described previously (Lin et al., 2022; Sun et al., 2019). AAV1-CaMKIIa-GCaMP6f-WPRE-SV40 was purchased from Addgene. Mice were anesthetized with 1.5% - 2% isoflurane and placed on a stereotaxic instrument (Stoelting). Stereotactic injection was performed with a micromanipulator guided by a digital atlas. The virus was injected into dorsal CA1 (AP -1.94, L 1.4, DV -1.38 mm, relative to the bregma) of the right hemisphere using a glass micropipette. We recorded from the right hippocampus as the right side of the brain tends to be more related to processing spatial information (Shinohara et al., 2012; Lin et al., 2022). A 0.5-mm-diameter hole was drilled in the skull above the injection site. The diameter of the pipette tip was 20–30 μm. The virus titer was 1 × 1013 GC/ml and injection volume was 0.3 μl. The virus was infused at speed of 0.1 μl /min by short pulses of air pressure (PICOSPRITZER III). The glass

pipette remained in place for 5 min before being withdrawn. Mice were treated with carprofen (3 mg/kg) as analgesia for 3 days after surgery.

GRIN lens implantation and miniscope installation

a GRIN lens was implanted into the brain tissue of the mice two weeks after virus injection (Sun et al., 2019). Mice were anesthetized with isoflurane, and carprofen as well as dexamethasone (2 mg/kg) were administered. A craniotomy of 2-mm-diameter was performed over CA1, centered at AP -2.3, L 1.75 mm. Dura was removed with ultrafine forceps, and the cortical tissue above the target CA1 area was aspirated using a 29-G blunt needle connected to vacuum, until the vertical striations of corpus callosum appeared. Sterile saline was continuously applied during aspiration. After bleeding stopped, a GRIN lens (1.8 mm diameter, 4.3 mm length, 0.25 PITCH, Edmund Optics) was lowered to contact the corpus callosum (depth − 1.55 mm) for CA1 imaging, which was secured with superglue and dental cement. The skull and lens were covered with Kwik-Sil silicone elastomer (WPI) and mice were allowed to recover for 2–3 weeks. After recovery, mice were anesthetized again, Kwik-Sil was removed and a miniscope (UCLA) mounted onto a baseplate was placed on the GRIN lens to search the imaging area. After cells being in focus, the baseplate was attached to the skull with dental cement, the miniscope was removed and a plastic cap was placed on the baseplate to prevent dust.

Linear track experiment

Mice were handled and habituated with miniscope tethering before tests. Before the experiment, mice were water restricted until their bodyweight reached 85% - 90% of the initial weight (3–5 days). They were then trained to run back and forth on a 1-m-long linear track to obtain 10–20 μl of water reward on either end of the track. After 5 days of training, miniscope was tethered and mice were trained for another 5 days. The testing consisted of two sessions at 30 min apart each

day and was repeated for two days. On the first day, the linear track was placed in the initial orientation of training. On the second day, the track remained the initial orientation in the first session and rotated 90 degrees in the second session. Mice were recorded for 30 trials (laps) in each session, usually finishing in 10–15 min. Linear track was cleaned with 70% ethanol before each recording.

Calcium imaging data preprocessing

Calcium imaging data was down-sampled to 15 frames/sec. To adjust for rigid, between-frame movements of the brain relative to the camera, motion correction was applied to the images with an established calcium imaging motion correction pipeline, NormCorre (Pnevmatikakis & Giovannucci, 2017) (https://github.com/flatironinstitute/NoRMCorre). The corrected recordings under different conditions were aligned with each other by aligning the neurons that appeared across conditions and were combined prior to neuron extraction.

Extraction of calcium transients in individual neurons using the CNMF-E method

The calcium signals of neurons were extracted from the combined recording using the Extended Constrained Nonnegative Matrix Factorization (CNMF-E) method proposed by Zhou et al (Zhou et al., 2018) (https://github.com/zhoupc/CNMF_E). This method models the recording as follows:

$$y(\mathrm{x}, t) = \sum_{i=1}^{\mathrm{K}} a_i(\mathrm{x}) * c_i(t) + b(\mathrm{x}, t)$$

Where $y(x, t)$ represents the raw video data, $a_i(x)$ represent the neuron's spatial footprint, $c_i(t)$ represents the temporal calcium activity and $b(x, t)$ represents the background activity. The software applies sophisticated background approximation to remove the background component,

and by iteratively applying constrained nonnegative matrix factorization to the remaining data, extracts the temporal varying calcium dynamic and the spatial footprint of neurons in the recordings. After extraction, we applied manual intervention to further remove false detections with aberrant shapes and temporal responses.

Mouse movement tracking

The movement trajectory of the mouse was extracted from overhead videos using a Logitech web camera which has a sample rate of 30 Hz. The floor of any given arena is selected as the region of interest (ROI) to restrict the area for detection of movement. A red LED built into the miniscope is detected inside the ROI of each frame, and its centroid position is captured using customized MATLAB software. The locomotor trajectory is constructed from the positions of red LED across all frames and smoothed with a moving average.

Spike train and spatial rate map calculation

The calcium spike trains are estimated by applying the CNMF-E embedded deconvolution algorithm, OASIS (Friedrich et al., 2017). A threshold of 3 times of the standard deviation of the spike train is applied for each neuron and spikes lower than the threshold was discarded.

Spatial rate maps were calculated as follows: the locomotor trajectory was downsampled to 15 Hz to be aligned with the calcium responses. The linear track space was divided into 2.5 cm X 2.5 cm bins. For each bin, the total time the mouse occupied that location was determined as the total number of events occurring while occupying that bin (C). The spatial event rate for each bin (bin rate) thus was defined as the ratio of C and bin time. After construction, the rate map is smoothed with a 10 cm x 10 cm 2D Gaussian kernel (delta = 2cm). Because linear track is a 1-D environment, the rate maps thus were averaged across the shorter dimension with to obtain 1-D rate maps which then represent the overall activation along the longer 1-meter dimension. The

trajectory and calcium data within 10% of both ends were excluded as they are inside the water reward area.

Generalized Louvain Clustering

We utilized a community clustering method called Generalized Louvain Clustering (De Meo et al., 2011; Lucas G. S. Jeub, 2019). This algorithm is a modified version of the original Louvain clustering algorithm, which detects subgroups of highly interconnected elements within a large element set. The basic idea of Generalized Louvain Clustering is the same to the original Louvain Clustering (Blondel et al., 2008), which is described as follows:

given a set of neurons N,

- Step1: Randomly choose one neuron ***n*** from ***N***, assign it into community ***a***.
- Step2: For other neurons that are neighbors to ***n***, assign a neuron to community ***a*** if the assignment induces the highest modularity change to ***N*** compared to other neighboring neurons.
- Step3: loop through all the neighbors for neurons in community ***a*** until no neuron assignments will induce modularity change to ***N***, then finish ***a***'s construction.
- Step4: Repeat step 1-3 for all remaining neurons and finish construction for all communities.
- Step5: Regard each community as an "aggregated neuron", which forms a set ***M.*** Calculate the correlation between the aggregated neurons in ***M*** (i.e. averaged correlation between all neurons formulating two "aggregated neurons").
- Step6: repeat step 1-4 for ***M*** until the modularity of ***M*** stabilized. A new set of communities by the aggregated neurons are formed.

- Step7: repeat step 5-6 until each aggregated unit represents its own community. Then for each neuron, their community (cluster) identity is determined by the aggregated unit they participated in.

Compared to the original Louvain clustering algorithm, the Generalized Louvain algorithm introduced improvements to make sure the algorithm is not affected by the connectivity structures within ***N*** (De Meo et al., 2011). As randomization are introduced during the step1, to achieve a replicable clustering result, 1000 pass of the Generalized Louvain Clustering will be performed and formulate a consensus matrix representing the frequencies each pair of neurons will be assigned to the same cluster. The candidate cluster numbers will be all potential cluster numbers appeared during the 1000 cluster pass. Hierarchical clustering will be performed using each cluster number and the consensus matrix, and the cluster number that results a hierarchical clustering partition that are most similar to all the 1000 cluster partitions (quantified by Adjusted Rand Index, see the "Cluster similarity" section below) will be selected as the optimal cluster number. Thus, the final clustering result is the hierarchical clustering partition corresponding to the optimal cluster number.

Intra- and inter- cluster pairwise correlation and spatial distance

Pearson correlation of calcium signals was calculated for all neuron pairs of each mouse according to their cluster memberships. Baseline correlations are created by performing 1000 randomized shuffles of cluster identity and taking the average correlation levels across 1000 shuffle pass.

Anatomically contiguous patches of CA1 anatomical space

Same as Chapter 1, we used Density-Based Spatial Clustering of Applications with Noise (DBSCAN)(Ester et al., 1996) to isolate the anatomically compact neuron clusters. We define the

95^{th} percentile of the minimum anatomical distance across all neurons as the maximal distance between intra-cluster neuron pairs and use 3 as the minimal number of intra-cluster neurons.

Ensemble rate map and major ensemble firing field overlap

Ensemble rate map of each cluster was calculated by averaging the rate maps of all individual intra-cluster neurons. The major firing firing field of ensemble rate maps were calculated as the continuous areas with bin rate higher than 45% of the maximum bin rate in the map. The overlap between multiple major ensemble firing fields was calculated as the ratio between overlapping area of the two major fields, and the total area of the two major fields. For each mouse the overlap level is calculated for each pair of the ensemble rate maps, and the final overlap level per mouse is the averaged overlap level across all pairs of ensemble rate maps.

Cluster similarity

Different from Chapter 1, in this study we tried to quantify the cluster partitions without limiting the number of clusters, as the different cluster numbers themselves could represent a meaningful representation of the physiological difference of micro-circuits. However, comparing cluster partitions with different numbers requires correction for the chance-level similarity. Hence, we utilized the established metric adjusted rand index (ARI) to quantify the cluster similarity in this study (Hubert & Arabie, 1985; Steinley, 2004). ARI is calculated as follows:

Suppose we have two cluster partitions P1 and P2 on the same set of elements,

a= number of element pairs always stay in the same cluster in P1 and P2;

b= number of element pairs stay in the same cluster in P1 but not P2;

c= number of element pairs stay in the same cluster in P2 but not P1;

d= number of element pairs stay in different clusters in both P1 and P2;

The original Rand Index (RI), which is a simple matching for two cluster partitions, is calculated as

$$RI = \frac{a + d}{a + b + c + d}$$

While the ARI is a corrected-for-chance-level version of RI, which is calculated as

$$ARI = \frac{RI - E(RI)}{1 - E(RI)} = \frac{(a + b + c + d)(a + d) - [(a + b)(a + c) + (c + d)(b + d)]}{(a + b + c + d)^2 - [(a + b)(a + c) + (c + d)(b + d)]}$$

In which $E(RI) = \frac{(a+b)(a+c)+(c+d)(b+d)}{(a+b+c+d)^2}$ represent the mathematical expectation of similarity between P1 and P2, i.e. the chance level similarity (Steinley, 2004).

Quantification and statistical analysis

Data are presented as the mean ± SEM. Two-tailed Wilcoxon rank sum test was used for testing statistical significance between distributions of individual mouse. Linear mixed-effect modeling (LME) is used to address the repeat measurement issues inside our data (Yu et al., 2021). The level of statistical significance was defined as are defined as $p \leq 0.05$ *, $p < 0.01$ **, $p < 0.001$ ***.

Result

Temporally correlated hippocampal CA1 neurons are organized anatomically regardless of ages and genotypes

The first question we asked is how the pairwise correlation pattern between CA1 pyramidal cells differs between WT and AD mice, as well as across ages, as in Chapter 1 we identified temporally correlated CA1 neuron subgroups in ordinary mice. To answer this, we

utilize miniscope imaging to examine the calcium-induced fluorescence during the first linear track traverse trial of the two-days track rotation experiment. Apart from the K-mean based algorithm used in Chapter 1, we use a community detection algorithm called Generalized Louvain Clustering (Lucas G. S. Jeub, 2019) which also defined the temporal clusters based on pairwise temporal correlation between neurons, while do not acquire any cluster number constrain. We find that for both WT and AD mice across different ages, CA1 pyramidal neuron subgroups could display temporally correlated activity that spans across seconds, like the results in Chapter 1 (Figure 3.1 B-C, 7 young WT mice and 8 young AD mice, 6 middle-age WT mice and 6 middle-age AD mice, 4 old WT mice and 3 old AD mice). To determine their statistical significance, we adopted Chapter 1's strategy by comparing the correlation between neuron pairs within each cluster, between clusters, as well as within randomly shuffled clusters which serves as baseline. At young and middle age, intra-cluster neurons of both WT and AD mice show significantly higher pairwise correlation toward inter-cluster neuron pairs and baseline, while for old mice, WT show significantly higher intra-cluster pairwise correlation while AD only show a non-significant trend (Figure 3.1 D-F). Meanwhile, comparing intra-cluster correlations across ages, no significant differences are noted for both WT and AD mice (Figure 3.1 G). This indicates regardless of genotypes and ages, CA1 pyramidal neuron population could contains subgroups of co-firing neurons that defining multiple temporal clusters.

In Chapter 1 we also show that temporally correlated CA1 pyramidal neurons could form anatomical clusters. Hence, we performed the same operation by plotting the memberships of temporal clusters into anatomical space. We see a similar anatomical organization as appeared in Chapter 1, that temporally correlated pyramidal neuron subgroups organized into one or multiple anatomical clusters under the imaging field of view (Figure 1 H-I). We quantify the size of those

anatomical clusters by using the density-based spatial clustering of applications with noise (DBSCAN) algorithm and compared the original anatomical cluster size with their corresponding baseline generated by shuffling the cluster membership. At young and middle age, for both WT and AD mice, the original anatomical cluster sizes significantly surpass the baseline, while for the old age only a same tendency trend appears (not significant). When comparing across ages, no significant differences are noted between the anatomical cluster size at different ages, for both WT and AD mice. This indicates that the appearance of the anatomical organization we defined in Chapter 1 is not affected by AD condition or aging, but whether there are differences in the characteristics of these anatomical clusters remains to be studied.

Higher Overlap between ensemble rate maps among young 5xFAD mice

Although both wildtype and 5xFAD mice display anatomically organized, temporally correlated CA1 neuron subgroups, these clusters may have differentiated functional significance, considering AD's impact on the cognitive performance and memory. In Chapter 1 we investigated the functional meaning of the temporal-anatomical CA1 neuron clusters by examine the environment coverage of the ensemble rate map, calculated by averaging the rate maps of individual intra-cluster neurons, and found that the ensemble activity of different clusters covers different portion of the open field. If the phenomenon also applies for animals in this study, an interesting question would be whether the ensemble firing fields of AD animal are more overlapped with each other, which potentially represent impaired populational representation of locations.

We first visualized the ensemble rate maps of six example mice of different genotypes and ages (Figure 3.2 A, B). Ensemble rate maps of different clusters were showing location-specific activity at specific portions along the linear track, indicate that the detected temporal-anatomical

CA1 neuron clusters exhibit spatial related activities similar the those discovered in Chapter 1. Although due to the constrained environment in linear track, ensemble activities between different clusters are more likely to overlap with each other (Figure 3.2 C). Nevertheless, we quantified the overlap between the major field of the ensemble rate maps (rate map areas with >45% of maximum bin rate) and compared the averaged overlap level between genotypes and ages (Figure 3.2 C, D). For young, aged mice, 5xFAD population shows a significant higher overlap level compared to the corresponding wildtype population, which support our hypothesis that the populational environment representation of CA1 neurons in young 5xFAD mice could be diffused and unspecific. No difference is noted for middle-aged mice and old 5xFAD mice. Apart from the small number of old mice population, the continued experiments of the mouse populations across age may also contribute to better location separation abilities among the AD-mice population, which represented as the drop in overlap level among middle-aged 5xFAD mice (Figure 3.2 D). However, further investigations are still needed to examine the reason for the indifferent cluster-level environment representation in middle-aged and old-aged mice.

Age-specific dissimilarity in pairwise correlation pattern and anatomical clusters between linear tracks with different directions

Next, we asked whether the revealed temporal-anatomical CA1 pyramidal neuron clusters can reflect environment changes, and if the reflection differs between WT and AD animal across ages. To answer this question, we utilized a track rotation experiment like the one used in Chapter 1. On the first day, mice will perform two trials in which the tracks will be placed in the same direction, and on the second day, track in the second trial will be rotated by 90 degrees, effectively alters the global environment mice will perceive during traverse.

We first examined the rate map correlation between the two trials with the track in the first (tracks in same direction) and second day (track in different directions). For young and middle-aged mice, both WT and AD exhibit significant remapping between the two trials with tracks in different directions, as the rate map correlation exhibits a significant drop. For old mice, only WT exhibits a significant rate map correlation difference between the two different direction tracks. Old AD did not display obvious trend of rate map correlation difference (Figure 3.3 C-E). This indicates that the rotation of the track successfully induces notable remapping across the CA1 pyramidal neuron populations of young WT and AD, middle-aged WT and AD, and old WT mice.

We then move on to examine the similarity between the pairwise correlation patterns (defined as the Pearson correlation between the neuron-neuron pairwise temporal correlation matrices of two trials) between tracks with same or different directions. Interestingly, we only find a significant similarity decrease between the different direction tracks at middle-age, and this decrease was applied to both WT and AD mice (Figure 3.2 G-I). We then performed clustering to the neuron populations and compared the anatomical cluster similarities between the same and different direction tracks. Again, only middle-aged mice display a significant drop in cluster similarity between different direction tracks (Figure 3.2 K-M).

In Chapter 1, we have discovered that mice would show significantly decreased anatomical cluster similarity between tracks with 90-degree direction difference, which aligns with the anatomical cluster similarities drop described among the middle-aged mice. However, rate map correlation also illustrated remapping events for young WT, young AD, and old WT, of which both pairwise correlation pattern and anatomical clusters did not exhibit significant change. We hypothesized that this phenomenon may be related to the different types of remapping strategies animals were taken in each experiment, for example, the existence of partial remapping can cause

a difference between rate map correlations, while only causing a partial change to the co-firing relationship between neurons that is not enough for a cognitive map reconstruction (Kubie et al., 2020). The difference in the remapping strategies could be caused by the combined effect of experience and aging. However, whether the results presented here represent an age-specific change in remapping strategy remains to be investigated.

While we noted a difference in rate map correlation change between old WT and AD mice, no difference was noted for young and middle-aged mice, as both WT and AD in these two age groups display higher rate map correlations between same direction tracks than different direction tracks. This may be explained by the reduced populational rate map stability among the old AD mice, and the indifferent rate map correlation level at young and middle age discovered by the linear-mixed effect modeling in the original study (Zhang et al., 2023). The middle-age specific similarity decreases of pairwise correlation pattern and anatomical clusters, however, do not differ between genotypes. Whether this indicates an age-specific influence of AD on the temporal correlation – defined cognitive map, but not individual neurons' spatial coding, remains to be further studied.

Global pairwise correlation level display age and genotype variated relationship with the segregation level of anatomical clusters

Although we were able to note the anatomical clusters by projecting the membership of temporally correlated pyramidal cell subgroups into anatomical space, no quantitative features of the anatomical organization have been defined to be compared with the temporal activity or spatial rate maps, and across genotypes and ages. Hence, here we defined a feature called mosaic level, which measures the diversity of cluster types around any individual neuron under the field of view. Basically, for a specific neuron and its 10 neighbors, mosaic level is calculated as the ratio between

the number of neuron pairs with different cluster types, and the total number of pairs (11 neurons results in 55 pairs). Hence the metric will be higher in the area with more diversified cluster types (Figure 3.4 A). The overall mosaic level of a sample is calculated as the averaged mosaic level across all neurons, which could represent the overall segregation level of anatomical clusters, as scattered anatomical cluster patches will cause more neurons to possess a higher mosaic level (Figure 3.4 A).

With the metric, we first asked if there's any difference between the overall mosaic levels across genotypes and ages, and we noted no differences (Figure 3.4 B). This means both WT and AD mice in different age groups can display various levels of anatomical cluster patch sizes, as we noted in Figure 3.1. We then calculated its relationship with the averaged pairwise correlation level, as pairwise correlation is the most direct variable for calculating the temporal-anatomical cluster organizations. Interestingly, we noted a significant negative relationship between the mosaic level and intra-cluster pairwise correlation level for the young and middle-aged WT mice, as well as young AD mice. Old WT and AD mice, as well as middle-age AD mice show a non-significant negative trend between the two variables. This could be attributed to the fact that higher mosaic level will make it more probable for a neuron's neighbor to be inter-cluster neurons, which share a relatively low pairwise correlation. Lastly, we compared the relationship between mosaic level and spatial rate map correlation and found no significant relationship between the two measures (Figure 3.4 D). These results indicate that there's a relationship between the anatomical organization of the pyramidal neurons and the temporal correlation between neurons, but the anatomical feature may not have strong relationship with the spatial coding similarity of the neurons. Meanwhile, the absence of significance between mosaic level and temporal pairwise correlation in mid AD, old WT, and old AD may indicate an influence of age and disease stage on

the temporal-anatomical pyramidal neuron clusters, but further studies are needed to establish this hypothesis.

Discussion

In this study, we examined our recent findings of anatomically organized, temporally correlated CA1 pyramidal neuron organizations in WT and 5xFAD mice across three different ages. We focus on four major questions: 1. Whether the intra-cluster correlation and anatomical cluster size differ between genotypes and ages; 2. Whether the functional role of the temporal-anatomical clusters display differences between genotypes and ages 3. Whether the temporal-anatomical clusters display reduced similarity between rotated linear track, and how this phenomenon differs across genotypes and ages; 4. Whether there's a quantitative feature displayed by the anatomical clusters that show direct correlation with neural activities. We find that CA1 pyramidal neurons of both WT and AD mice across different ages display the temporal-anatomical cluster organization, and the intra-cluster correlation level, as well as anatomical cluster size, did not show significant difference across genotypes and ages. When examining the cluster-level ensemble representation of the environment, young AD mice show a lower level of specificity between the labelling of different clusters, but no differences were noted between WT and AD for other age groups. At the same time, although rate map correlation showed significant remapping for both WT and AD mice at young and middle age, as well as old WT mice, the pairwise correlation patterns as well as anatomical cluster similarities only showed significant drop at middle age. Lastly, we defined mosaic level, a measure of the anatomical clusters' segregation level, and found this metric is negatively correlated with the averaged intra-cluster pairwise correlation of the whole pyramidal neuron populations, which means anatomical clusters could be

a major factor promoting the pairwise temporal correlation between neurons. Meanwhile, the metric does not have significant relationship with the correlation between spatial rate maps.

Although AD is known to disrupt connectivity of CA1 neural circuits, and the accumulation of AD-related pathology could lead to abnormal firing patterns of individual pyramidal neurons (Busche et al., 2012), the temporal-anatomical cluster organizations we previously discovered still exist under AD condition. In this dataset, Aβ plaques already exists under 4 month age of the 5xFAD animal (Zhang et al., 2023), indicating the CA1 circuits could already been under pathological condition at young age. Indeed, the higher overlap level between the cluster-wide ensemble activities of young AD mice may advocate the presence of pathological conditions, but it did not explain the non-significance of middle-age and old age animals. The mixed results may either indicate that this organization is relative robust to AD's influence, or the organizations are influenced by the disease, but only in specific aspects that we have not discovered yet, for example, the way neuron memberships change between multiple anatomical clusters along time. The unknown effect of AD on the temporal-anatomical CA1 pyramidal cell clusters could also be responsible to the middle-age specific, genotype invariant similarity reduction of cluster similarity between different direction tracks. Overall, although we confirmed the existence of the anatomically organized, temporally correlated CA1 pyramidal neuron subgroups under both WT and AD condition across ages, future research are required to fully uncover the influence of AD and aging on this type of organization.

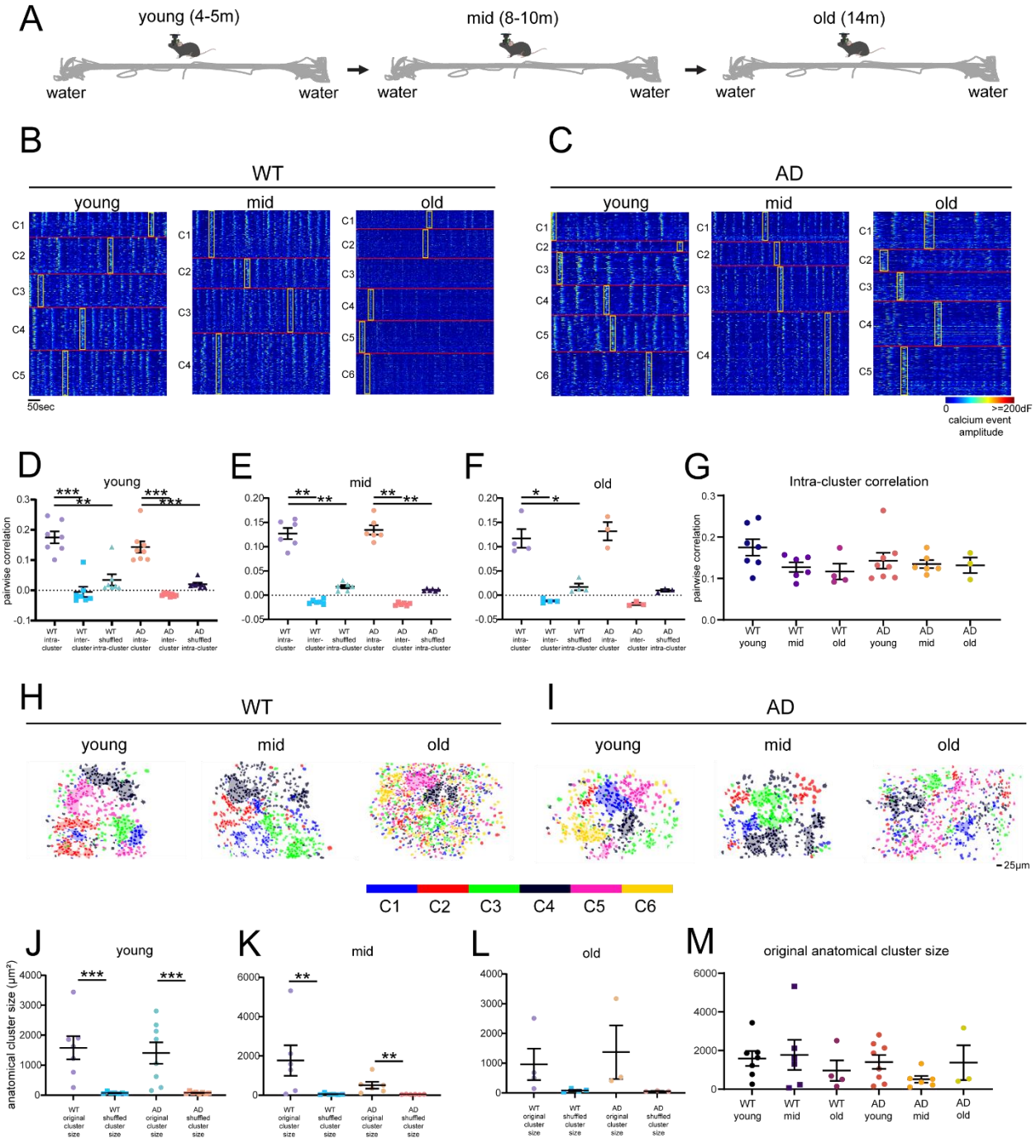
A
young (4-5m)
mid (8-10m)
old (14m)
water
water
water
water
water
water
B
WT
young
mid
old
C1
C2
C3
C4
C5
C6
50sec
C
AD
young
mid
old
0
>=200dF
calcium event amplitude
D
young
E
mid
F
old
pairwise correlation
WT intra-cluster
WT inter-cluster
WT shuffled intra-cluster
AD intra-cluster
AD inter-cluster
AD shuffled intra-cluster
G
Intra-cluster correlation
WT young
WT mid
WT old
AD young
AD mid
AD old
H
WT
young
mid
old
I
AD
young
mid
old
25µm
C1
C2
C3
C4
C5
C6
J
young
K
mid
L
old
anatomical cluster size (µm²)
WT original cluster size
WT shuffled cluster size
AD original cluster size
AD shuffled cluster size
M
original anatomical cluster size
WT young
WT mid
WT old
AD young
AD mid
AD old

Figure 3.1. Temporally correlated hippocampal CA1 neurons are organized into anatomically clustered groups regardless of ages and genotypes A. Illustration of a mouse with a head-mounted miniscope targeting the hippocampal CA1 region, and its trajectories in the linear track environment (track length = 1m). Gray line represents the traverse trajectory the mouse was taken inside the track. All mice will be examined across three age spans (4-5 months, 8-10 months, and 14 months). **B-C.** Heatmap of temporal calcium response of all neurons grouped into clusters recorded from example wild type (WT) mice (B), and 5xFAD mice (C), at different ages. Each row of the heatmap represent a single neuron. Yellow rectangles represent typical correlated firing events in the neuron subgroups **D-F.** Comparisons of intra- and inter- cluster pairwise temporal correlations, as well as shuffled intra-cluster pairwise correlation, of neuron calcium activity of both WT mice and 5xFAD mice across ages. For both WT and AD mice at young and mid age, Intra-cluster correlation is significantly higher than both shuffled and inter-cluster correlation. Old WT mice show significantly higher intra-cluster correlation toward inter-cluster and shuffled intra-cluster correlation, while old AD mice do not show significant difference (D: young mice, WT intra-cluster, 0.1749 ± 0.0198; WT inter-cluster, -0.0051 ± 0.0169; WT shuffled intra-cluster, 0.0341 ± 0.0186; AD intra-cluster, 0.1427 ± 0.0190; AD inter-cluster, -0.0148 ± 0.0018; AD shuffled intra-cluster: 0.0200 ± 0.0047. WT intra-cluster vs. inter-cluster, p= 0.0006; WT intra-cluster vs. shuffled intra-cluster-cluster, p= 0.0023; AD intra-cluster vs. inter-cluster, p=0.0002; AD intra-cluster vs. shuffled intra-cluster, p=0.0002. Mann Whitney test, 7 WT mice and 8 AD mice) (E: middle-aged mice, WT intra-cluster, 0.1273 ± 0.0115; WT inter-cluster, -0.0135 ± 0.0115; WT shuffled intra-cluster, 0.0176 ± 0.0034; AD intra-cluster, 0.1345 ± 0.0096; AD inter-cluster, -0.0183 ± 0.0012; AD shuffled intra-cluster: 0.0110 ± 0.0010. WT intra-cluster vs. inter-cluster, p= 0.0022; WT intra-cluster vs. shuffled intra-cluster-cluster, p= 0.0022; AD intra-cluster vs. inter-cluster, p=0.0022; AD intra-cluster vs. shuffled intra-cluster, p=0.0002. Mann Whitney test, 6 WT mice and 6 AD mice) (F: old mice, WT intra-cluster, 0.1169 ± 0.0192; WT inter-cluster, -0.0117 ± 0.0022; WT shuffled intra-cluster, 0.0170 ± 0.0068; AD intra-cluster, 0.1317 ± 0.0187; AD inter-cluster, -0.0179 ± 0.0025; AD shuffled intra-cluster: 0.0099 ± 0.0024. WT intra-cluster vs. inter-cluster, p= 0.0286; WT intra-cluster vs. shuffled intra-cluster-cluster, p= 0.0286; AD intra-cluster vs. inter-cluster, p=0.1000; AD intra-cluster vs. shuffled intra-cluster, p=0.1000. Mann Whitney test, 4 WT mice and 3 AD mice) **G.** Comparison of intra-cluster pairwise correlations between WT and AD mice at different ages. No significant differences were noted between genotype and ages (p=0.3397; Kruskal-Wallis test. No significant difference noted between any two groups using Dunn's multiple comparison test) **H-I.** Anatomical clusters of neural calcium event footprints of temporally correlated neurons from WT mice (H), and AD mice(I), of three different ages. **J-L.** Average patch size of original anatomical clusters compared to shuffled baseline. Shuffle baseline is created by averaging the patch size of anatomical clusters with shuffled cluster membership. Overall, for both WT and AD mice at young and middle age, their original cluster size is significantly higher than the shuffled baseline. For old mice, original cluster patch sizes only show a non-significant trend of higher than baseline (J: young mice, WT original, 1583 ± 383.80 μm^2; WT baseline, 73.31 ± 12.70 μm^2; AD original, 1406 ± 359.10 μm^2;

AD baseline, 77.34 ± 13.36 μm^2. WT original vs. WT baseline: p=0.0006; AD original vs AD baseline: p=0.0002; Two-tailed Wilcoxon ranksum test, 7 WT mice and 8 AD mice) (K: middle-aged mice, WT original, 1770 ± 779.30 μm^2; WT baseline, 62.08 ± 17.65 μm^2; AD original, 512.90 ± 175.80 μm^2; AD baseline, 48.16 ± 4.16 μm^2. WT original vs. WT baseline: p=0.0043; AD original vs AD baseline: p=0.0022; Two-tailed Wilcoxon ranksum test, 6 WT mice and 6 AD mice) (L: old mice, WT original, 960.90 ± 528.50 μm^2; WT baseline, 82.67 ± 27.87 μm^2; AD original, 1371 ± 901.1 μm^2; AD baseline, 59.02 ± 10.17 μm^2. WT original vs. WT baseline: p=0.0571; AD original vs AD baseline: p=0.1000; Two-tailed Wilcoxon ranksum test, 4 WT mice and 3 AD mice) **M.** Comparison of original anatomical cluster patch size between WT and AD genotypes across three age groups. Overall, no significant difference is noted between WT and AD mice at same ages, or between different age groups of the same genotype (p=0.4493, Kruskal-Wallis test. No significant difference noted between any two groups using Dunn's multiple comparison test)

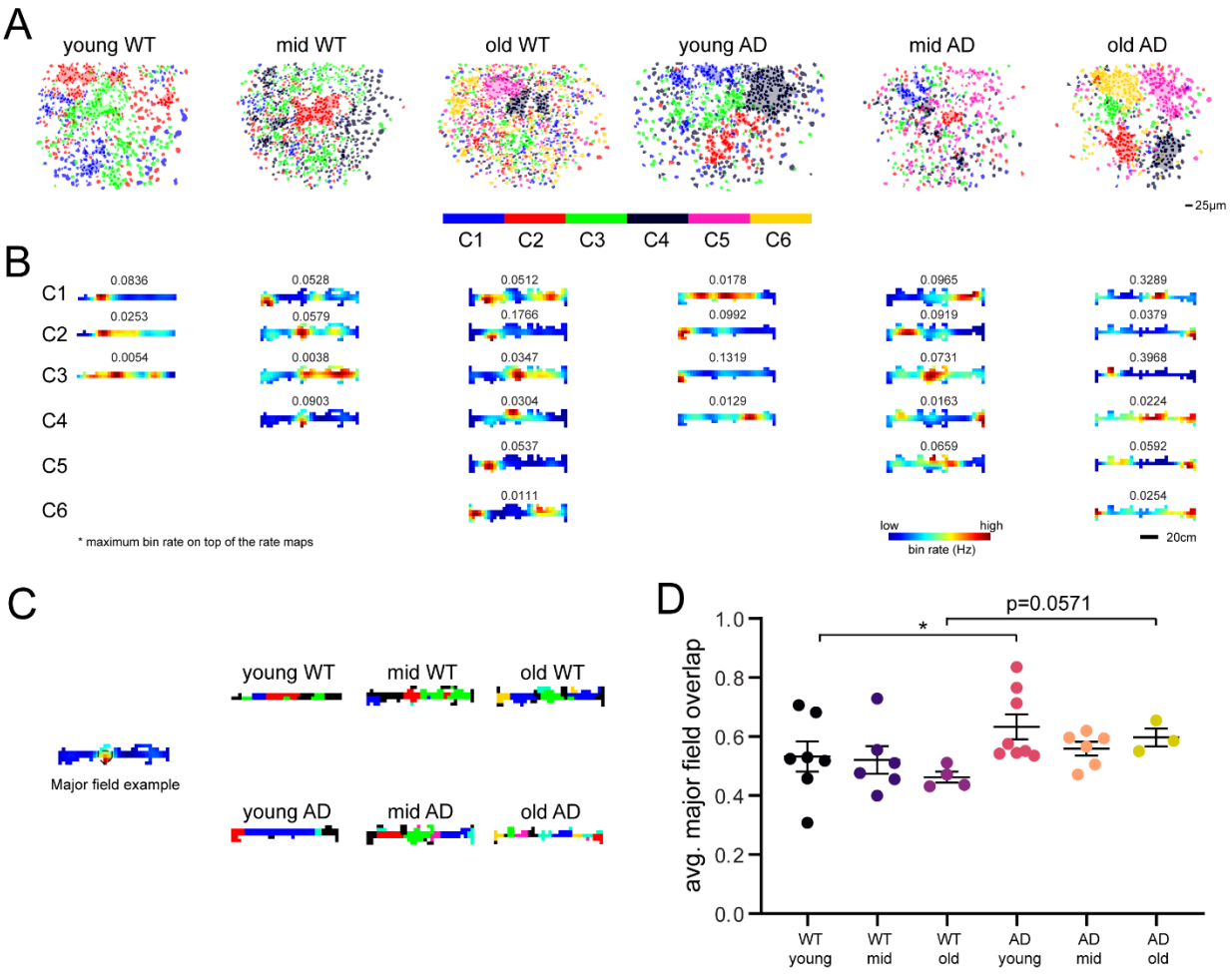

Figure 3.2. Higher Overlap between ensemble rate maps among young 5xFAD mice A. Illustration of the anatomical cluster footprints for 6 examine mice of different genotypes and ages. **B.** Ensemble rate map of each cluster for the corresponding mice in A. The maximum firing rate is labeled on top of each rate map. **C.** illustration of major field of the ensemble rate map (left), and the overlay of all major fields for the ensemble rate maps for each mouse in B. Major fields are calculated as the area inside rate map with bin rate higher than the 45% of the maximum bin rate **D.** Averaged major field overlap level for mice across genotypes and ages. Young AD mice show significantly higher overlap than corresponding WT mice, while old AD mice show a non-significant trend of higher overlap level than corresponding WT (young WT: 0.5325 ± 0.0509, middle-aged WT: 0.5207 ± 0.0467, old WT: 0.4624 ± 0.0185, young AD: 0.6328 ± 0.0424, middle-aged AD: 0.5587 ± 0.0237, old AD: 0.5969 ± 0.0304, mean ± SEM. young WT vs. young AD: p=0.0401; middle-aged WT vs. middle-aged AD: p=0.3095; old WT vs. old AD: p=0.0571, Two-tailed Wilcoxon ranksum test)

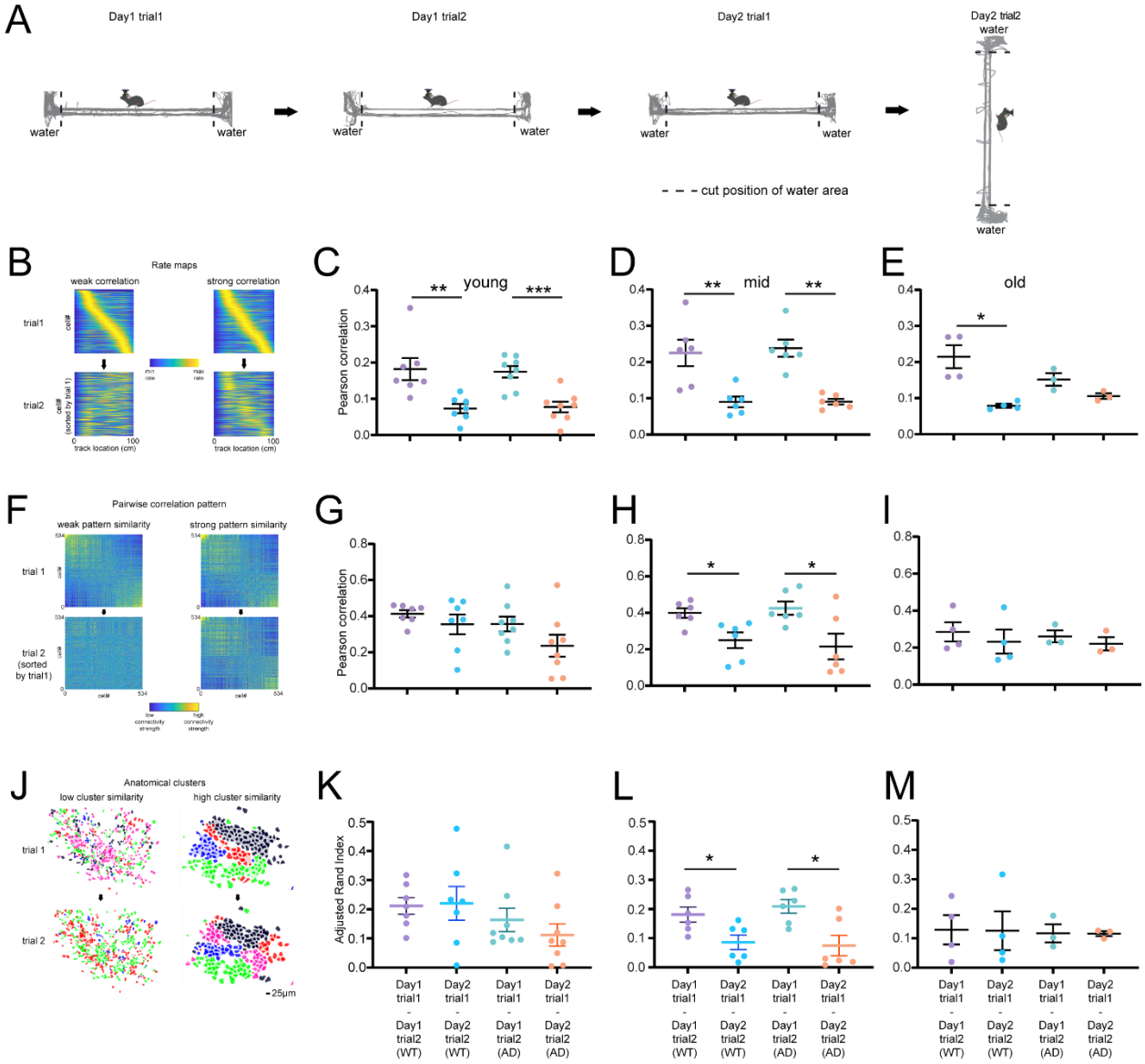

Figure 3.3. Age-specific dissimilarity of CA1 neural clusters between rotated linear tracks A. Illustration of the track rotation experiment. On the first day, two trials with the track placed in the same direction (Horizontal direction) are performed, while on the second day, in the second trial the track will be rotated by 90 degrees. Gray line represents the traverse trajectory the mouse was taken inside the track. All WT and AD mice will be examined across three age spans (4-5 months, 8-10 months, and 14 months). **B.** Example rate map pairs with weak and strong correlation. Collective rate maps of the mice are formulated by stacking the one-dimensional rate maps of individual cells together. In trial 1 the rate maps are sorted based on the peak firing rate location of each cell, while in trial 2 the cell orders are the same as trial 1. Color represents the level of normalized firing rate in each spatial bin (2.5cm) **C-E.** Averaged rate map correlation per mice between the two same direction tracks in the first day, and the two different direction tracks in the second day, for both WT and AD mice across three ages. At young and middle age, both WT and AD mice show significantly higher rate map correlation between the same direction tracks (Day1

trial1 and Day1 trial2) than between tracks with different direction (Day2 trial1 and Day2 trial2). For old mice the difference only appears for WT genotype. No significant difference noted between WT and AD mice across three ages (**C**: young mice. WT Day1: 0.1821±0.0305, WT Day2: 0.0730±0.0126, AD Day1: 0.1744±0.0157, AD Day2: 0.0770±0.0147. WT Day1 vs. WT Day2: p=0.0012, AD Day1 vs. AD Day2: p=0.0006, WT Day1 vs. AD Day1: p=0.6126, WT Day2 vs. AD Day2: p=0.9999. Mann- Whitney test, 7WT and 8AD mice) (**D**: middle-aged mice. WT Day1: 0.2250±0.0366, WT Day2: 0.0898±0.0146, AD Day1: 0.2382±0.0238, AD Day2: 0.0906±0.0076. WT Day1 vs. WT Day2: p=0.0087, AD Day1 vs. AD Day2: p=0.0022, WT Day1 vs. AD Day1: p=0.9372, WT Day2 vs. AD Day2: p=0.8182. Two-tailed Wilcoxon ranksum test, 6WT and 6AD mice) (**E**: old mice. WT Day1: 0.2146±0.0318, WT Day2: 0.0787±0.0053, AD Day1: 0.1518±0.0173, AD Day2: 0.1057±0.0078. WT Day1 vs. WT Day2: p=0.0286, AD Day1 vs. AD Day2: p=0.1000, WT Day1 vs. AD Day1: p=0.2286, WT Day2 vs. AD Day2: p=0.0571. Two-tailed Wilcoxon ranksum test, 4WT and 3AD mice) **F.** Example functional connectivity patterns with weak and strong correlation. Functional connectivity is calculated as the pairwise correlation between each pair of neurons during a track traverse trial. The color in the connectivity pattern represents the connectivity strength (correlation) between each pair of neurons. The similarity between functional connectivity patterns of different trials is represented as the correlation between two connectivity pattern matrices **G-I.** Connectivity pattern similarity per mice between the two same direction tracks in the first day, and the two different direction tracks in the second day, for both WT and AD mice across three ages. Only for middle-aged mice, both WT and AD mice show significantly higher connectivity pattern correlation between the same direction tracks (Day1 trial1 and Day1 trial2) than between tracks with different direction (Day2 trial1 and Day2 trial2). No significant differences noted for young and old mice, as well as between genotypes (**G**: young mice. WT Day1: 0.4131±0.0206, WT Day2: 0.3549±0.0549, AD Day1: 0.3569±0.0404, AD Day2: 0.2364±0.0604. WT Day1 vs. WT Day2: p=0.6200, AD Day1 vs. AD Day2: p=0.0830, WT Day1 vs. AD Day1: p=0.1520, WT Day2 vs. AD Day2: p=0.1520. Mann-Whitney test, 7WT and 8AD mice) (**H**: middle-aged mice. WT Day1: 0.3988±0.0263, WT Day2: 0.2498±0.0431, AD Day1: 0.4251±0.0364, AD Day2: 0.2152±0.0703. WT Day1 vs. WT Day2: p=0.0152, AD Day1 vs. AD Day2: p=0.0411, WT Day1 vs. AD Day1: p=0.6991, WT Day2 vs. AD Day2: p=0.6991. Two-tailed Wilcoxon ranksum test, 6WT and 6AD mice) (**I**: old mice. WT Day1: 0.2851±0.0522, WT Day2: 0.2326±0.0652, AD Day1: 0.2612±0.0326, AD Day2: 0.2208±0.0357. WT Day1 vs. WT Day2: p=0.4857, AD Day1 vs. AD Day2: p=0.4000, WT Day1 vs. AD Day1: p=0.8571, WT Day2 vs. AD Day2: p=0.8571. Two-tailed Wilcoxon ranksum test, 4WT and 3AD mice) J. Example anatomical clusters with weak and strong cluster similarity. The similarity between two cluster partitions is measured by Adjusted Rand Index (ARI) **K-M**. Cluster similarity per mice between the two same direction tracks in the first day, and the two different direction tracks in the second day, for both WT and AD mice across three ages. Only for middle-aged mice, both WT and AD mice show significantly higher cluster similarity between the same direction tracks (Day1 trial1 and Day1 trial2) than between tracks with different direction (Day2 trial1 and Day2 trial2). No significant differences noted for young and old mice, as well as between genotypes (**K**: young mice. WT Day1: 0.2118±0.0286, WT Day2: 0.2201±0.0579, AD Day1: 0.1634±0.0403, AD Day2: 0.1115±0.0382. WT Day1 vs. WT Day2: p=0.9999, AD Day1 vs. AD Day2: p=0.1949, WT Day1 vs. AD Day1: p=0.1520, WT Day2 vs. AD Day2: p=0.1893. Mann-

Whitney test, 7WT and 8AD mice) (**L**: middle-aged mice. WT Day1: 0.1810±0.0258, WT Day2: 0.0861±0.0250, AD Day1: 0.2090±0.0234, AD Day2: 0.0747±0.0350. WT Day1 vs. WT Day2: p=0.0411, AD Day1 vs. D Day2: p=0.0260, WT Day1 vs. AD Day1: p=0.5887, WT Day2 vs. AD Day2: p=0.6991. Two-tailed Wilcoxon ranksum test, 6WT and 6AD mice) (**M**: old mice. WT Day1: 0.1283±0.0498, WT Day2: 0.1255±0.0660, AD Day1: 0.1168±0.0310, AD Day2: 0.1157±0.0083. WT Day1 vs. WT Day2: p=0.9999, AD Day1 vs. D Day2: p=0.9999, WT Day1 vs. AD Day1: p=0.9999, WT Day2 vs. AD Day2: p=0.6286. Two-tailed Wilcoxon ranksum test, 4WT and 3AD mice)

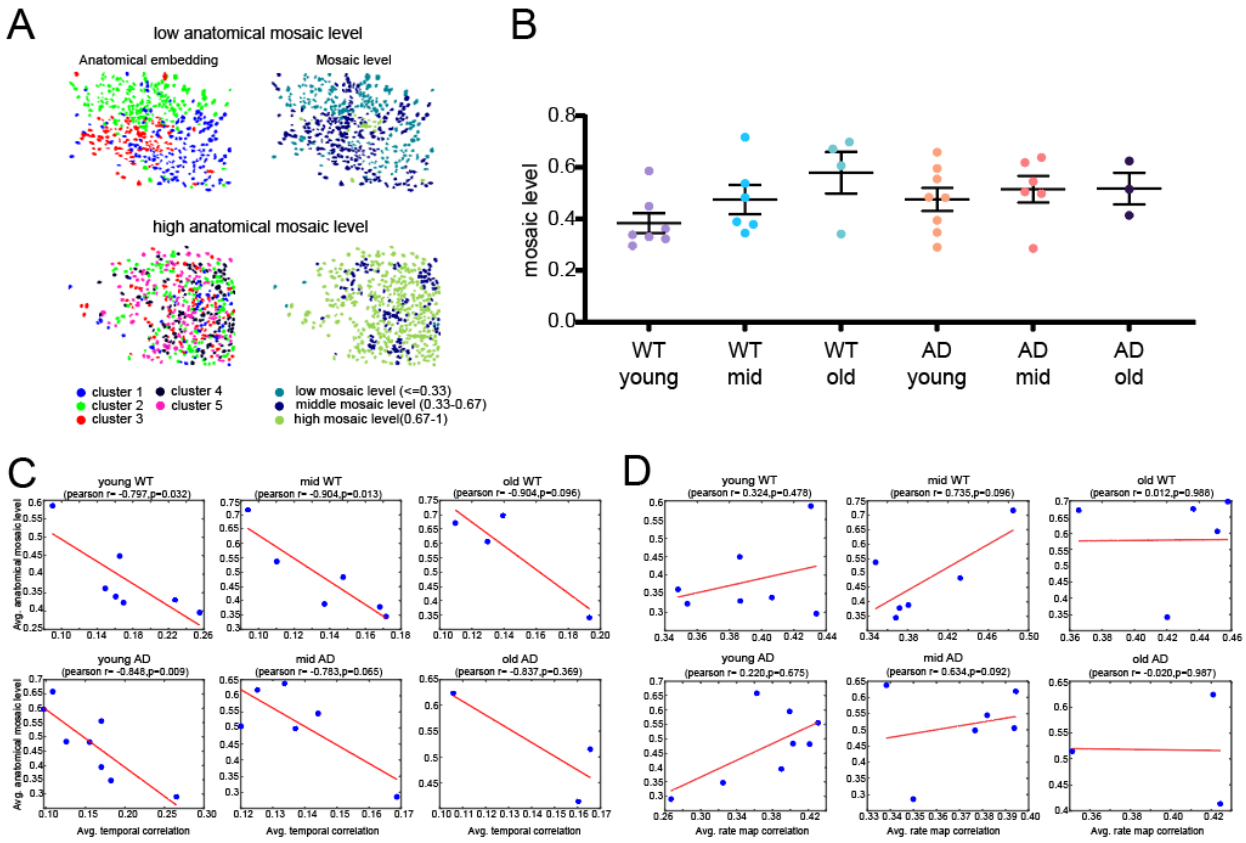

Figure 3.4. Mosaic level of anatomical clusters display significant correlation with temporal correlation but not rate map correlation A. Illustration of the mosaic level of anatomical clusters. Mosaic level is used to quantify the segregation level of anatomical clusters, for each neuron, its local mosaic level is calculated as the fraction of neuron pairs with different cluster assignment of its 11 neighboring neurons include itself. Overall mosaic level is calculated by averaging the local mosaic level of all neurons together. Two example mice with different overall mosaic levels are shown here. **B.** Overall mosaic level across genotypes and ages. No significant differences are noted (young WT: 0.3834±0.0384, middle-aged WT: 0.4749±0.0565, old WT: 0.5792±0.0815, young AD: 0.4758±0.0446, middle-aged AD: 0.5151±0.0515, old AD: 0.5175±0.0608, p=0.2009, Kruskal-Wallis test with Dunn's multiple comparisons test) **C.** Relationship between anatomical mosaic level and intra-cluster pairwise temporal correlation. Overall, young and middle-aged WT mice, as well as young AD mice, show a significant negative trend between the two measures, while old WT, middle-aged AD and old AD only show a non-significant negative trend (young WT: r = -0.797, p=0.032; young AD: r=-0.848, p=0.009; middle-aged WT: r=-0.904, p=0.013; middle-aged AD: r=-0.783, p=0.065; old WT: r=-0.904, p=0.096; old AD: r=-0.837, p=0.369) **D.** Relationship between anatomical mosaic level and intra-cluster pairwise rate map correlation. Overall, young and middle-aged mice, both WT and AD, display a positive but non-significant trend between mosaic level and rate map correlation, while old WT and old AD display non obvious trend (young WT: r = 0.324, p=0.478; young AD: r=0.634, p=0.092; middle-aged WT: r=0.735, p=0.096; middle-aged AD: r=-0.220, p=0.675; old WT: r=-0.904, p=0.096; old AD: r=-0.837, p=0.369)

References

Blondel, V. D., Guillaume, J.-L., Lambiotte, R., & Lefebvre, E. (2008). Fast unfolding of communities in large networks. *Journal of Statistical Mechanics: Theory and Experiment*, *2008*(10), P10008. https://doi.org/10.1088/1742-5468/2008/10/P10008

Busche, M. A., Chen, X., Henning, H. A., Reichwald, J., Staufenbiel, M., Sakmann, B., & Konnerth, A. (2012). Critical role of soluble amyloid-β for early hippocampal hyperactivity in a mouse model of Alzheimer's disease. *Proceedings of the National Academy of Sciences*, *109*(22), 8740. https://doi.org/10.1073/pnas.1206171109

Buzsáki, G. (2010). Neural Syntax: Cell Assemblies, Synapsembles, and Readers. *Neuron*, *68*(3), 362-385. https://doi.org/https://doi.org/10.1016/j.neuron.2010.09.023

Buzsáki, G. (2019). *The Brain from Inside Out*. Oxford University Press. https://doi.org/10.1093/oso/9780190905385.001.0001

De Meo, P., Ferrara, E., Fiumara, G., & Provetti, A. (2011). Generalized Louvain Method for Community Detection in Large Networks. *International Conference on Intelligent Systems Design and Applications, ISDA*. https://doi.org/10.1109/ISDA.2011.6121636

Dombeck, D. A., Harvey, C. D., Tian, L., Looger, L. L., & Tank, D. W. (2010). Functional imaging of hippocampal place cells at cellular resolution during virtual navigation. *Nature Neuroscience*, *13*(11), 1433-1440. https://doi.org/10.1038/nn.2648

Eichenbaum, H. (2014). Time cells in the hippocampus: a new dimension for mapping memories. *Nature Reviews Neuroscience*, *15*(11), 732-744. https://doi.org/10.1038/nrn3827

Ester, M., Kriegel, H.-P., Sander, J., & Xu, X. (1996). *A density-based algorithm for discovering clusters in large spatial databases with noise* Proceedings of the Second International Conference on Knowledge Discovery and Data Mining, Portland, Oregon.

Friedrich, J., Zhou, P., & Paninski, L. (2017). Fast online deconvolution of calcium imaging data. *PLOS Computational Biology*, *13*(3), e1005423. https://doi.org/10.1371/journal.pcbi.1005423

Gauthier, J. L., & Tank, D. W. (2018). A Dedicated Population for Reward Coding in the Hippocampus. *Neuron*, *99*(1), 179-193.e177. https://doi.org/https://doi.org/10.1016/j.neuron.2018.06.008

Geiller, T., Sadeh, S., Rolotti, S. V., Blockus, H., Vancura, B., Negrean, A., Murray, A. J., Rózsa, B., Polleux, F., Clopath, C., & Losonczy, A. (2022). Local circuit amplification of spatial selectivity in the hippocampus. *Nature*, *601*(7891), 105-109. https://doi.org/10.1038/s41586-021-04169-9

Grieco, S. F., Holmes, T. C., & Xu, X. (2023). Probing neural circuit mechanisms in Alzheimer's disease using novel technologies. *Molecular Psychiatry*. https://doi.org/10.1038/s41380-023-02018-x

Grienberger, C., Rochefort, N. L., Adelsberger, H., Henning, H. A., Hill, D. N., Reichwald, J., Staufenbiel, M., & Konnerth, A. (2012). Staged decline of neuronal function in vivo in an animal model of Alzheimer's disease. *Nature Communications*, *3*(1), 774. https://doi.org/10.1038/ncomms1783

Harris, K. D., Csicsvari, J., Hirase, H., Dragoi, G., & Buzsáki, G. (2003). Organization of cell assemblies in the hippocampus. *Nature*, *424*(6948), 552-556. https://doi.org/10.1038/nature01834

Hubert, L., & Arabie, P. (1985). Comparing partitions. *Journal of Classification*, *2*(1), 193-218. https://doi.org/10.1007/BF01908075

Jun, H., Bramian, A., Soma, S., Saito, T., Saido, T. C., & Igarashi, K. M. (2020). Disrupted Place Cell Remapping and Impaired Grid Cells in a Knockin Model of Alzheimer's Disease. *Neuron*, *107*(6), 1095-1112.e1096. https://doi.org/https://doi.org/10.1016/j.neuron.2020.06.023

Kubie, J. L., Levy, E. R. J., & Fenton, A. A. (2020). Is hippocampal remapping the physiological basis for context? [https://doi.org/10.1002/hipo.23160]. *Hippocampus*, *30*(8), 851-864. https://doi.org/https://doi.org/10.1002/hipo.23160

Kuchibhotla, K. V., Goldman, S. T., Lattarulo, C. R., Wu, H.-Y., Hyman, B. T., & Bacskai, B. J. (2008). Aβ Plaques Lead to Aberrant Regulation of Calcium Homeostasis In Vivo Resulting in Structural and Functional Disruption of Neuronal Networks. *Neuron*, *59*(2), 214-225. https://doi.org/https://doi.org/10.1016/j.neuron.2008.06.008

Kurudenkandy, F. R., Zilberter, M., Biverstål, H., Presto, J., Honcharenko, D., Strömberg, R., Johansson, J., Winblad, B., & Fisahn, A. (2014). Amyloid-β-Induced Action Potential Desynchronization and Degradation of Hippocampal Gamma Oscillations Is Prevented by Interference with Peptide Conformation Change and Aggregation. *The Journal of Neuroscience*, *34*(34), 11416. https://doi.org/10.1523/JNEUROSCI.1195-14.2014

Lin, X., Chen, L., Baglietto-Vargas, D., Kamalipour, P., Ye, Q., LaFerla, F. M., Nitz, D. A., Holmes, T. C., & Xu, X. (2022). Spatial coding defects of hippocampal neural ensemble calcium activities in the triple-transgenic Alzheimer's disease mouse model. *Neurobiology of Disease*, *162*, 105562. https://doi.org/https://doi.org/10.1016/j.nbd.2021.105562

Lucas G. S. Jeub, M. B., Inderjit S. Jutla, and Peter J. Mucha. (2019). *A generalized Louvain method for community detection implemented in MATLAB*. In https://github.com/GenLouvain/GenLouvain

Modi, M. N., Dhawale, A. K., & Bhalla, U. S. (2014). CA1 cell activity sequences emerge after reorganization of network correlation structure during associative learning. *eLife*, *3*, e01982. https://doi.org/10.7554/eLife.01982

Neuman, K. M., Molina-Campos, E., Musial, T. F., Price, A. L., Oh, K.-J., Wolke, M. L., Buss, E. W., Scheff, S. W., Mufson, E. J., & Nicholson, D. A. (2015). Evidence for Alzheimer's disease-linked synapse loss and compensation in mouse and human hippocampal CA1 pyramidal neurons. *Brain Structure and Function*, *220*(6), 3143-3165. https://doi.org/10.1007/s00429-014-0848-z

O'Keefe, J., & Dostrovsky, J. (1971). The hippocampus as a spatial map. Preliminary evidence from unit activity in the freely-moving rat. *Brain Research*, *34*(1), 171-175. https://doi.org/https://doi.org/10.1016/0006-8993(71)90358-1

Palop, J. J., & Mucke, L. (2016). Network abnormalities and interneuron dysfunction in Alzheimer disease. *Nature Reviews Neuroscience*, *17*(12), 777-792. https://doi.org/10.1038/nrn.2016.141

Properties of the Hubert-Arable Adjusted Rand Index, 9 American Psychological Association 386-396 (2004).

Sun, Y., Jin, S., Lin, X., Chen, L., Qiao, X., Jiang, L., Zhou, P., Johnston, K. G., Golshani, P., Nie, Q., Holmes, T. C., Nitz, D. A., & Xu, X. (2019). CA1-projecting subiculum neurons facilitate object–place learning. *Nature Neuroscience*, *22*(11), 1857-1870. https://doi.org/10.1038/s41593-019-0496-y

Yu, Z., Guindani, M., Grieco, S. F., Chen, L., Holmes, T. C., & Xu, X. (2021). Beyond t test and ANOVA: applications of mixed-effects models for more rigorous statistical analysis in neuroscience research. *Neuron*. https://doi.org/https://doi.org/10.1016/j.neuron.2021.10.030

Zhang, H., Chen, L., Johnston, K. G., Crapser, J., Green, K. N., Ha, N. M.-L., Tenner, A. J., Holmes, T. C., Nitz, D. A., & Xu, X. (2023). Degenerate mapping of environmental location presages deficits in object-location encoding and memory in the 5xFAD mouse model for Alzheimer's disease. *Neurobiology of Disease*, *176*, 105939. https://doi.org/https://doi.org/10.1016/j.nbd.2022.105939

Zhou, P., Resendez, S. L., Rodriguez-Romaguera, J., Jimenez, J. C., Neufeld, S. Q., Giovannucci, A., Friedrich, J., Pnevmatikakis, E. A., Stuber, G. D., Hen, R., Kheirbek, M. A., Sabatini, B. L., Kass, R. E., & Paninski, L. (2018). Efficient and accurate extraction of in vivo calcium signals from microendoscopic video data. *eLife*, *7*, e28728. https://doi.org/10.7554/eLife.28728

Chapter 4: Conclusions and future directions

In this dissertation, I explored the ensemble dynamic of CA1 pyramidal neurons under both healthy condition and Alzheimer's disease. Especially, I tried to investigate the long-standing question about the anatomical embedding of the temporally correlated CA1 pyramidal neuron subgroups. Utilizing the head mounted miniature microscope, I started with reporting the anatomically clustered, temporally correlated pyramidal neuron subpopulations inside hippocampal CA1 region of healthy mice during open field arena traverse. These temporal-anatomical neuron clusters display ensemble activities that covers different regions in the explored environment, while also exhibiting elevated pattern dissimilarity between altered environments like linear tracks with 90-degree direction difference, and square arenas with or without barrier inside, but not closely placed arenas with different geometries (Chapter 1). With the novel CA1 pyramidal neuron organization established, I propose to examine the difference of this organization between healthy and Alzheimer's disease animals. Before formally exploring the difference, I first utilized the 3xTg AD mouse strain to examine the difference of ensemble CA1 pyramidal neuron response between AD and WT condition. I confirmed the results of previous research that CA1 pyramidal neuron populations of AD mice display hyperexcitability compared to control inside 2D open arena, but not in the linear track. At the same time, when representing the spatial representation ability by information score, in both open field and linear track the control mice display higher score value compared to the AD mice at different ages, while their firing fields display lower spatial coherence and sparsity, indicating higher spatial selectivity compared to their AD counter parts. This illustrates that defects in spatial representation widely exist inside the CA1 pyramidal cells in AD animals, which could be the result of the circuit degradation and cytotoxicity caused by the AD -related symptoms (Chapter 2). Having proved the AD's negative influence on the functionality of CA1 pyramidal neurons, I moved on to examine the impact of AD on the

temporal-anatomical CA1 pyramidal neuron clusters discovered in Chapter 1, using 5xFAD mice and corresponding wild type controls. Interestingly, this type of organization exists in both WT and 5xFAD mice across ages, and the correlation level of intra-cluster cell pairs, as well as the anatomical cluster size, do not differ across genotypes and ages. In the meantime, both WT and AD mice display the cluster organization shift between linear tracks with 90-degree direction difference, but only at the 8-10 month middle age. Lastly, in terms of the relationship between anatomical feature and functional feature, the mosaic level, a metric measuring the segregation level of anatomical clusters, is negatively correlated with the populational pairwise correlation strength of the CA1 pyramidal neurons, but not the spatial rate map correlation, indicating the anatomical organization could be more relevant to the functional connectivity between neurons defined by temporal relationship, rather than spatial coding similarity (Chapter 3). Together, the results in the dissertation have discovered a under studied anatomical organization of the CA1 pyramidal neurons displaying correlated ensemble firing and performed preliminary attempts to examine the organization's properties under Alzheimer's disease condition.

Future research in similar directions could focus on characterizing the temporal-anatomical CA1 pyramidal neuron clusters under different physiological conditions and cognitive tasks. For example, between wild type and Alzheimer's disease animals, the impact on the organization may be more prevalent under more complicated cognitive tasks like object location memory (Zhang et al., 2023). Also, features like anatomical cluster assimilation and split during remapping, and cluster stability between individual laps of the trial, have not been examined by the current study, and worth examination as may reveal the impact of AD condition. Lastly, utilizing optogenetic and chemical methods to manipulate the CA1 circuit could also be an important way to reveal the organizations' underlying circuit-level mechanism.

In the meantime, it would be worthwhile to consider the existing imaging studies that claims CA1 pyramidal neuron assemblies do not exhibit patterned anatomical distributions (Liu et al., 2022; Villette et al., 2015). In these studies, the "temporal clusters" of the CA1 pyramidal cells are defined only using highly correlated neurons. For example, Villette et al. using Otsu thresholding to only keep the neurons with relatively high correlations (Villette et al., 2015), and Liu et al. tried to defined temporal clusters based on deconvoluted spikes rather than the original calcium signal, which requires strict temporal activity alignment for intra-cluster neurons (Liu et al., 2022). Although it is admitted that highly correlated neurons could be more rigid in terms of defining functional assemblies, it should be considered that the less correlated neurons, if their correlation is higher than a defined baseline, could still represent their meaningful contributions to a correlated subpopulation. Our method, similar to the one used in Modi et al. 2014 research and previous study in dorsal striatum (Barbera et al., 2016; Modi et al., 2014), utilize k-mean and community clustering and find that the correlation level of intra-cluster neuron pairs is overall higher than neuron pairs in different clusters, although the correlation level values themselves may be close to 0. Hence future studies should compare different ways of defining the temporally correlated neuron populations and distinguish the meanings of the neuron clusters returned by different clustering strategies.

Future research could also focus on the molecular level mechanism that helps guide the temporally correlated neuron subgroups, as well as their anatomical patterns. For example, whether the correlated neuron subgroups are the engram cells that display high immediate early gene expression (Miyashita et al., 2018), and whether the level of gene markers defining the temporally correlated neuron subgroups also show patterned anatomical distributions. In recent years, the advance of spatial transcriptomic technology has enabled genotyping neurons with their

anatomical profile maintained, which provide the opportunity of analyzing the molecular-defined cell type of specific functional organizations, as well as combining the anatomical distribution of specific genes' expression level with neuron footprints from functional imaging. Recent research has already tried to align the transcriptomic profile of hippocampal interneurons and aligned their gene expression pattern with temporal activation pattern based on the footprint matching between spatial transcriptomic and 2-photon imaging (Bugeon et al., 2022). The search of molecular mechanisms that could be related to this organization could be beneficial to pharmaceutical and medical research on memory and neurodegeneration diseases that involves the neural organization described here.

References

Barbera, G., Liang, B., Zhang, L., Gerfen, Charles R., Culurciello, E., Chen, R., Li, Y., & Lin, D.-T. (2016). Spatially Compact Neural Clusters in the Dorsal Striatum Encode Locomotion Relevant Information. *Neuron*, *92*(1), 202-213. https://doi.org/https://doi.org/10.1016/j.neuron.2016.08.037

Bugeon, S., Duffield, J., Dipoppa, M., Ritoux, A., Prankerd, I., Nicoloutsopoulos, D., Orme, D., Shinn, M., Peng, H., Forrest, H., Viduolyte, A., Reddy, C. B., Isogai, Y., Carandini, M., & Harris, K. D. (2022). A transcriptomic axis predicts state modulation of cortical interneurons. *Nature*, *607*(7918), 330-338. https://doi.org/10.1038/s41586-022-04915-7

Liu, X., Terada, S., Ramezani, M., Kim, J.-H., Lu, Y., Grosmark, A., Losonczy, A., & Kuzum, D. (2022). E-Cannula reveals anatomical diversity in sharp-wave ripples as a driver for the recruitment of distinct hippocampal assemblies. *Cell Reports*, *41*(1), 111453. https://doi.org/https://doi.org/10.1016/j.celrep.2022.111453

Miyashita, T., Kikuchi, E., Horiuchi, J., & Saitoe, M. (2018). Long-Term Memory Engram Cells Are Established by c-Fos/CREB Transcriptional Cycling. *Cell Reports*, *25*(10), 2716-2728.e2713. https://doi.org/https://doi.org/10.1016/j.celrep.2018.11.022

Modi, M. N., Dhawale, A. K., & Bhalla, U. S. (2014). CA1 cell activity sequences emerge after reorganization of network correlation structure during associative learning. *eLife*, *3*, e01982. https://doi.org/10.7554/eLife.01982

Villette, V., Malvache, A., Tressard, T., Dupuy, N., & Cossart, R. (2015). Internally Recurring Hippocampal Sequences as a Population Template of Spatiotemporal Information. *Neuron*, *88*(2), 357-366. https://doi.org/https://doi.org/10.1016/j.neuron.2015.09.052

Zhang, H., Chen, L., Johnston, K. G., Crapser, J., Green, K. N., Ha, N. M.-L., Tenner, A. J., Holmes, T. C., Nitz, D. A., & Xu, X. (2023). Degenerate mapping of environmental location presages deficits in object-location encoding and memory in the 5xFAD mouse model for Alzheimer's disease. *Neurobiology of Disease*, *176*, 105939. https://doi.org/https://doi.org/10.1016/j.nbd.2022.105939